POLITECNICO DI TORINO

Corso di Laurea Magistrale in Ingegneria Elettrica

Tesi di Laurea Magistrale

GRID-CONNECTED OPERATION OF A HYBRID MICROGRID

Design, operation and control of a Wind-Solar-Hydrogen Energy System

Relatori:
Prof. Ettore Bompard
Prof. Enrico Pons
Dr. Abouzar Estebsari
Dr. Andrea Mazza

Candidato:
Jonny Esteban Villa Londoño

Anno Accademico: 2018/2019

Dedicated

To

My Parents, my brother Edisson, my aunt Nubia and My Nita...

Without who my dream would have never come true.

Acknowledgements

First of all I would like to thank **Dr. Andrea Mazza** and **Professor Enrico Pons** for giving me the opportunity to do this master thesis.

I would like to express my gratitude to **Sabrina Fiorot** to have put at my disposal, the material necessary to do this thesis.

I thank the **Universidad de Antioquia - Department of Electrical Engineering** and **Politecnico di Torino - Department of Energy** for the opportunity to be part of this bilateral agreement, especially, to thank **Professor Jesus Lopez Lezama**, **Dra. Maritza Areiza**, **Dra. Sara Tobon**.

I also grateful to **Alessandro Benefazio**, **Edoardo Banchio**, **Laura Trombetta** and **Components Team** for their appearance in the most difficult moment of my life with a great opportunity and motivation.

I want to thank **Dr. Michel Montoya**, **Dra. Paula Trujillo**, and **Celsa's Commercial-Energy Team** for their willingness with this project in Italy.

It is a pleasure to thank all the people who made this thesis possible, to thank **Alejandro Munera**, **Natasha**, **Antonella Farì**. For their availability and support during this years.

I want to thank all my friends and family for their support, kindness and useful advice, thank to **Camilo Londoño**, **Sebastian Puerta**, **Andrés Lopez**.

Finally, I would like to thank my girlfriend **Nita** for her support, her "patience", her affections, and her motivation. Thank to my beloved **Ketmany** for her encouragement in the last part of this thesis.

I would like to thank my beloved **Parents** without who my dream would have never come true.

I also want to thank my aunt **Nubia** and my brother **Edisson** for their support, and for never leave me alone from the beginning until the end of this thesis.

Abstract

During the last years, the number of research and development ($R\&D$) projects regarding renewable energy sources (RES) increased. This caused an increase of the penetration of power generated from RES into the grid. In electrical systems, a microgrid (μG) coupled with RES can lead to significant economic and environmental benefits. However, it is necessary the compensation of all the problems due to the intermittent nature of RES. The major problems of these microgrids are caused mainly by an unpredictable generation from RES as a consequence of weather conditions. Furthermore, additional variability is due to the consumption load.

This thesis proposes a hybrid microgrid ($H\mu G$) model with distributed generators and an energy storage system. A control strategy is proposed as well. The $H\mu G$ presented is constituted by three distributed generator units (DGU), these are: *(i)* a photovoltaic system, *(ii)* a wind turbine and *(iii)* a PEM fuel cell system. Furthermore, an alkaline electrolyzer is proposed to produce hydrogen and a hydrogen tank is presented as an energy storage system. The main objectives of this work are: *(i)* proposing a dynamic model for each component of the $H\mu G$ and *(ii)* providing a strategy to reduce the power absorption from the grid under weather conditions good enough.

The photovoltaic system presented may operate tracking its maximum power point (MPP), while the wind turbine operates between its cut-on and cut-off speed. Both systems follow environmental conditions in order to be disconnected from the grid in periods with low wind and solar irradiation. When the power supplied from DGU is larger than the sum of the loads, demand and electrolyzer, it could be possible to charge the energy storage system (hydrogen tank) or to exchange power to the grid. In the same way, in poor environmental conditions, the power demand could be met by the power of the fuel cell, reducing the grid absorption.

The effectiveness of the alkaline electrolyzer and PEM fuel cell models is demonstrated. Measured data of a hydrogen system obtained from a precedent work in a laboratory are used to validate the models. In the hydrogen storage system, the state of charge is adjusted with an adaptive scheme. Furthermore, supervisory power control is designed to reduce

power exchange and to improve the system stability.

Finally, three cases were studied considering different summer load profiles measured in two days in an electrical substation of *Politecnico di Torino*. They present static and variable loads with the purpose to demand the highest performance of the system. Results demonstrated the advantages of a system with hydrogen as a medium to green energy produced by photovoltaic and wind systems, in order to reduce the power absorbed from the grid.

Keywords
Hybrid microgrid, Simulink model, Renewable energy sources, Alkaline electrolyzer, *PEM* fuel cell, Hydrogen storage tank, Control strategy.

Attached files
Matlab - Simulink model and user guide.

Contents

List of Figures

List of Tables

Chapter 1

Introduction

During the last years, the number of research and development ($R\&D$) projects regarding renewable energy sources (RES) increased. These projects are largely driven by government regulations. Thus, the increase of RES has attracted special attention over the world about new strategies to improve the operation and stability of energy systems, reducing the dependency of fossil fuels, or in a different point of view, reducing the emission of greenhouse gases [1]. However, the intermittent RES presents a risk to satisfy successfully the power demand. Therefore, the integration of energy storage systems (ESS) to the RES is a challenge in order to ensure the normal operation of the systems [2].

One way to overcome this challenge is the introduction of powerful new technologies as mediums to storage energy, i.e, hydrogen tanks. Hydrogen can deliver about three times more specific energy than its same weight of oil. Thus, it is often called the energy carrier of the future and it is a promising way to store energy from RES, whether solar or wind energy. [3]. Nevertheless, this requires developing high performing and robust models considering the possibility to be integrated with hydrogen. These models are called hybrid microgrids ($H\mu G$) [1].

The structure to consider could be composed by a whole H_2 energy system, which employs mainly fuel cells, electrolyzers and hydrogen tanks. Therefore, to present these new hybrid systems as a potential solution, two improvements have to be considering: *(i)* improvements in storage strategies to manage the surplus of energy associated with RES, whether with PV or wind turbine generators. *(ii)* strategies of energy management, in order to drive the power flow calculation of hydrogen systems integrated to μGs [1].

Although the power generation of energy has been historically based on a wide range

[1] Hybrid microgrids incorporate renewable energy sources, often as an add-on to diesel generator-based system [4]

of technologies, being the most commons fossil fuels, nuclear fuels, and hydropower systems. The constant searching for economic and industrial developments and, at the same time, the need to preserve the environment lead the current effort to replace the power produced from conventional sources to another one with a low environmental impact, meeting in this way the world agreements and treaties of climate and environmental change. [5].

Nowadays, several hydrogen energy projects around the world demonstrate the advantages of this technology as a storage medium. The performed studies suggest that wind energy and photovoltaic systems can be successfully stored into hydrogen tanks in applications like grid-connected or stand-alone. Where there is an excess of green power, it is converted into H_2 through an electrolyzer and stored into a hydrogen vessel to be used later. Moreover, a *PEM* fuel cell produces clean energy when there are poor weather conditions.

To emulate the behavior of the system, it is implemented a control strategy to manage the energy flow. The goal is to satisfy the grid requirements maximizing its benefit, optimizing the operation of each component of the system. Then, this thesis proposes (*i*) a control strategy for the $H\mu G$ and (*ii*) integration of a hydrogen tank as storage medium. This work is based on the following systematic approach:

1. Modeling the dynamic of each component of the $H\mu G$.
2. Validating the *PEM* fuel cell model and alkaline electrolyzer model using experimental data.
3. Proposing a $H\mu G$ model.
4. Implementing a control strategy for the power flow in order to operate correctly the hydrogen system.

Finally, the chapters are organized as follows: Chapter (*1*) introduces the $H\mu G$. Chapter (*2*) presents a dynamic model for each component of the system: PV system, wind turbine generator, alkaline eltrolyzer, *PEM* fuel cell and hydrogen tank. Chapter (3) shows a detailed description of the whole system and, it presents the validation for alkaline electrolyzer and *PEM* fuel cell models using experimental data. Chapter (*4*) proposes a control strategy to the system and, it shows the Matlab-Simulink (*R2016a*) models implemented. And Chapter (*5*) presents the simulation results under different cases of study.

Chapter 2

Modeling a Hybrid Microgrid

2.1 Introduction

Microgrids are now emerging from laboratory benches and pilot demonstration sites into commercial markets [6]. A microgrid is a group of interconnected loads and distributed energy resources within clearly defined electrical boundaries that acts as a single controllable entity with respect to the grid. It is comprising of distributed power generators and loads (DPG). In the last few years, the introduction of new technologies as renewable energies or unconventional ways to store energy suggests the term of $H\mu G$. A $H\mu G$ is a μG that combine RES with gas generator sets and energy storage capability can deliver clean, cost-effective electricity to remote locations with limited or no access to reliable utility power [7]. The $H\mu G$ can connect and disconnect from the grid to enable it to operate in both grid-connected or island mode [8].

The $H\mu G$ presented in this thesis is formed by a collection of different distributed generation units (DGU) and a ESS. The power from distributed generation is composed by; (i) a photovoltaic system (PV), (ii) wind turbine generators (WT), and a (iii) (PEM) fuel cell (FC). The ESS consists basically in a hydrogen storage tank (HST) coupled with an alkaline electroyzer (ELY). The ESS subsystem is connected to the load side and it is assumed to have enough capacity respect to the load, to store the surplus of power produced by PV and WT [9].

A general model of hydrogen storage system is integrated to manage the production and consumption of energy from the electrolyzer and the PEM fuel cell respectively. The electrolyzer is used to absorb rapidly the output power from RES, i.e. WT and PV systems and generates hydrogen as fuels for fuel cells. [9], [10].

The schematic diagram of the $H\mu G$ is presented in Figure 2.1 [11]. The sum of the

power demand P_{Demand} and electrolyzer power P_{ELY} is equal to the sum of the output power generated by turbine generators P_{WT}, photovoltaic generators P_{PV} and, *PEM* fuel cells P_{FC}. Equation (2.1) represents the power supplied to the load. [10].

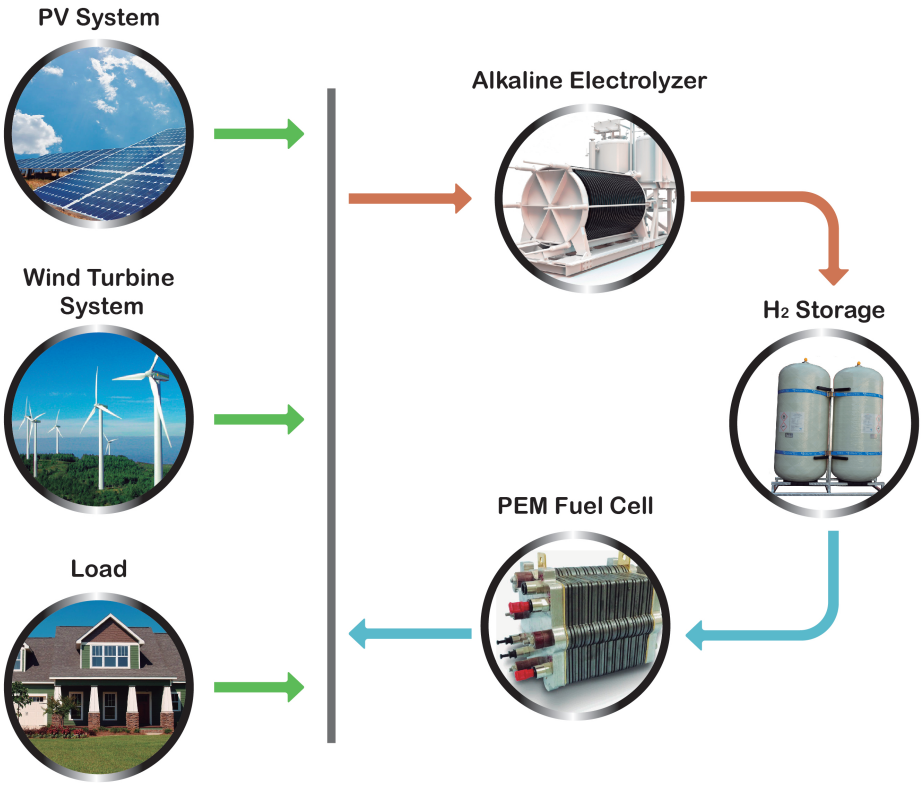

Figure 2.1: Schematic diagram of $H\mu G$.

$$P_{Load} = P_{WT} + P_{PV} + P_{FC} - P_{ELY} \tag{2.1}$$

In the follow sections is presented a general description of the technical specifications for each component of the $H\mu G$. Furthermore, the sections describe the models used to simulate the components of the $H\mu G$. Each physical component is modeled as a part of a modular system of *Simulink*. The models are presented in following order:

1. *PV* system model.
2. *WT* system model.
3. Alkaline electrolyzer.
4. *PEM* fuel cell.
5. Hydrogen storage tank.

2.2 Photovoltaic system

The *PV* system is composed by: (*i*) *PV* array, (*ii*) *DC-DC* boost converter with maximum power point tracker (using incremental conductance technique), (*iii*) three phases *VSC*, and (*iv*) a capacitor bank, as shown in Figure 2.2.

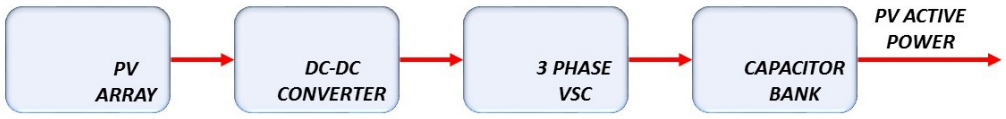

Figure 2.2: *PV* system.

The *PV* array delivers a maximum of 23 kW at 1000 W/m^2 sun irradiance. The boost converter increases the voltage from *PV* natural voltage 116 V DC at maximum power) to 625 V DC and, with the *MPPT* controller, the system detects automatically the correct duty cycle in order to extract the maximum power from the panel [12].

The *VSC* converts the 625 V DC link voltage to 380 V AC and keeps unity power factor. The *VSC* control system uses two control loops: (*i*) an external control loop which regulates *DC* link voltage to +/- 116 V DC and (*ii*) an internal control loop which regulates I_d and I_q grid currents (active and reactive current components). I_d current reference is the output of the *DC* voltage external controller. I_q current reference is set to zero in order to maintain unity power factor. V_d and V_q voltage outputs of the current controller are converted to three modulating signals $U_{abc-ref}$ used by the *PWM* generator. Finally, the capacitor bank filters the harmonics produced by *VSC*.

The parameters of the *PV* array are summarized in Table 2.1.

Table 2.1: Parameters of PV

***PV* array**	**Value**	**Unit**
Array power	23	kW
Cells per module	60	-
Open circuit voltage per module	36.3	V
Short circuit current per module	7.8	A
Series strings	4	-
Parallel strings	27	-
Voltage at *MPP*	29	V
Current at *MPP*	7.35	A
Maximun power per module at *MPP*	213.15	W
Maximun power per array at *MPP*	23.02	kW

2.3 Modeling PV System

PV generators are renewable source-based generators which provide as output a DC current and voltage [13]. In a photovoltaic system, the most visible part of the system are the PV panels. Usually, PV systems are composed by arrays and electric converters, where arrays are formed by series-parallel combination of solar modules and converters can be *DC-DC* or *DC-AC*. The efficiency is low compared to other conventional sources. The performance of a photovoltaic module is mostly affected by array configuration, irradiance, and module temperature.

PV cells convert solar energy into electric energy, based on the photovoltaic effect. [14]. Modeling cells and panels of a PV module allows understanding its operation under different conditions. Technologies such as cristalline silicon; (*i*) monocrystalline (m-Si) or (*ii*) pollycristallyne (*p-mi*), thin-film; (*iii*) amorphous silicon, (*iv*) copper indium-gallium diselenide (*CI-GS*) or (*v*) cadmiun telluride (*CdTe*) exist in the market [14]. However, crystalline silicon are still the most widely used material for manufacturing PV cells, while crystalline *Si* technologies are the most commonly employed for grid-connected applications.

2.3.1 Construction and structure

The solar cell is composed of two layers of semiconductor material. These materials are doped differently [15]. The photovoltaic cell is a *P-N* junction which is very similar to that of the classical diode with a *P-N* junction and is formed by the semiconductor material. The structure of a simplified silicon solar cell is shown in Figure 2.3. The upper side of the

electrode is made with silicon embedded metal elements to avoid obstruction of direct solar irradiation. The size and shape of the solar cell are designed to maximize the absorption of the surface and reduce the losses caused by contact resistance. The solar cell behaves as a *P-N* junction diode in the absence of solar irradiation [15].

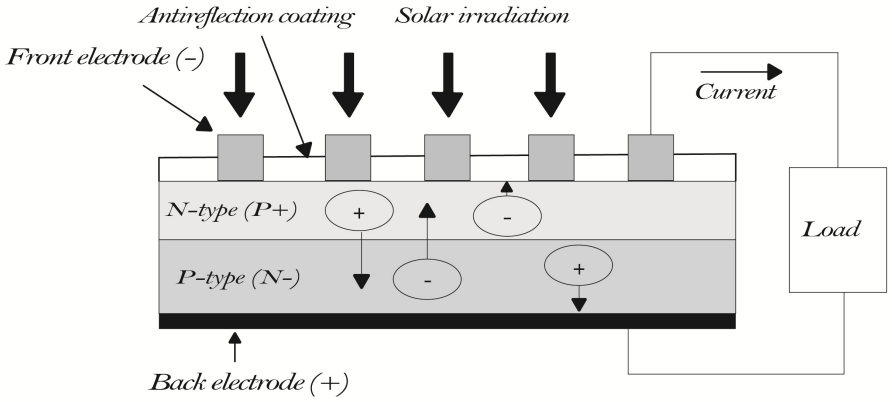

Figure 2.3: Solar cell structure.

2.3.2 Operation

As mentioned above, the production of power from solar cells depends on solar energy and the irradiation. With an incident light on the *P-N* junction of the two semiconductor materials, a *DC* electricity generation process occurs inside the photovoltaic cell as consequence of electron-hole pair [15].

During the absorption process of the light, the energy of the absorbed photon is transferred to the electron-proton system of the material, creating charge carriers that are separated at the junction. While absorbing solar irradiation, the *P-N* junction generates charge carriers which create a potential gradient, get accelerated under the electric field and circulate as the current through an external circuit.

This current is known as the photocurrent or current generated by the incident light I_{ph} and its magnitude depends upon the intensity of solar irradiation and the type of semiconductor material. [15].

Then, if a load is connected to the terminal of the solar cell, the excesses of charge flow through the load. This causes to the charge carriers to flow across the external circuit,

helping to build potential difference across the junction. The whole phenomenon is called *photovoltaic effect* [16].

2.3.3 Photovoltaic Model

A current modeling based on the Shockley and Queisser diode equation, allows to model the output current of a PV generator. The characteristics of the solar cell are determined by the Shockley diode equation [15]. The diode current I_d is related by an exponential relation, which is represented as in Eq. (2.2):

$$I_D = I_0 \cdot \left[\exp \left(\frac{q \cdot V}{N_s \cdot m \cdot K \cdot T_c} \right) - 1 \right] \tag{2.2}$$

where I_0 is the diode reverse bias saturation current, m is the diode ideality factor, N_s is the number of solar cells associated in series, K is the Boltzmann's constant in J/K and equals to $1.3807x10^{-23}$, T_c is the absolute temperature in K, V, is the voltage across the load, and q is the absolute value of the charge of an electron equals to $1.60217662x10^{-19}$ C [17].

The current source and diode make up the ideal PV model, the output current of the ideal model is expressed by (2.3):

$$I_{PV} = I_{ph} - I_D \tag{2.3}$$

where I_{PV} is the total output current, obtained from the superposition of I_{ph} and I_D, writing Eq. (2.2) on Eq. (2.3).

$$I_{PV} = I_{ph} - I_0 \cdot \left[\exp \left(\frac{q \cdot V}{N_s \cdot m \cdot K \cdot T_c} \right) - 1 \right] \tag{2.4}$$

where Eq. (2.4) represents the output current of a ideal model PV panel. As we can see, only three parameters allows modeling the output current, i.e., m, I_0, and I_{ph} which

is expressed in Eq. (2.5).

$$I_{ph} = q \cdot N \cdot A \tag{2.5}$$

where N is the number of photons in cm^2/s and A is the area of the semiconductor surface in m^2.

2.3.4 Considering the losses

Enhancing the current model means including the fundamental mechanism of loss in a solar cell. There are different non-ideal resistive components to be considered. The first mechanism is related to current flowing through the electrodes and silicon material through a resistance.

These losses can be represented as a resistance in series connection, R_s. After incorporating the series resistance, the output current of Eq. (2.4) is expressed as Eq. (2.6) which does not take into account the temperature variations.

$$I_{PV} = I_{ph} - I_0 \cdot \left[\exp^{\left(\frac{q \cdot (V + I \cdot R_s)}{N_s \cdot m \cdot K \cdot T_c} \right)} - 1 \right] \tag{2.6}$$

Other mechanism corresponds to one resistance to the P-N junction leakage current which can be represented by a parallel resistance, R_{sh} also called shunt resistance. Therefore, it is possible represents the equivalent circuit considering series and parallel resistance as shown in Figure 2.4. With the two new parameters, the model is represented by five unknown parameters.

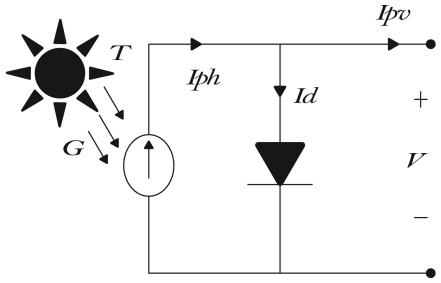

Figure 2.4: Equivalent circuit of a solar cell.

The output current I_{PV} is the difference between the photocurrent I_{ph}, the normal diode current I_D, and leakage current I_P, as expressed in Eq. (2.7).

$$I_{PV} = I_{ph} - I_D - I_P \tag{2.7}$$

Using Kirchhoff's circuit laws Eq. (2.7) can be written as Eq. (2.8).

$$I_{PV} = I_{ph} - I_0 \cdot \left[\exp\left(\frac{q \cdot (V + I \cdot R_s)}{N_s \cdot m \cdot K \cdot T_c} \right) - 1 \right] - \frac{V - I \cdot R_s}{R_{sh}} \tag{2.8}$$

Defining V_t as the thermal voltage for a single PV cell, which is expressed by Eq. (2.9),

$$V_t = \frac{m \cdot N_{cs} \cdot K \cdot \ T_c}{q} \tag{2.9}$$

Equation (2.8) can be written as Eq. (2.10):

$$I_{PV} = I_{ph} - I_0 \cdot \left[\exp\left(\frac{(V + I \cdot R_s)}{V_t} \right) - 1 \right] - \frac{V - I \cdot R_s}{R_{sh}} \tag{2.10}$$

2.3.5 Equivalent circuit of a solar cell

A PV generator is traditionally represented by an equivalent circuit referred to five-parameters of the one-diode model [15]. As shown in Figure 2.5, solar cell is represented by a current source parallel with a P-N junction diode connected in anti-parallel. The five parameters are: (i) I_p, (ii) I_0, (iii) m , (iv) R_s, and (v) R_{sh}.

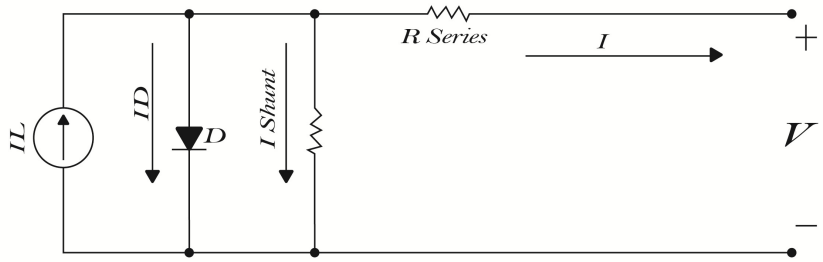

Figure 2.5: Equivalent circuit of a solar cell.

Applying the kirchoff's voltage and current laws to the equivalent circuit of a cell, the flow current to the load and the voltage can be obtained, show in Eq. (2.11) and Eq. (2.12) respectively:

$$I = I_{ph} - I_j - \frac{U_j}{R_{sh}} \tag{2.11}$$

$$U = U_j - R_s \cdot I \tag{2.12}$$

Where U is the voltage across the terminals of the load, and the current I as shown in Figure 2.5 is the current flowing inside the load.

2.3.6 Connection

To obtain high power, a certain number of PV modules have to be connected in a specific configuration called array. An array of PV panels is a group of several modules electrically connected in series-parallel combination to generate the required current and voltage [16]. The total number of cells connected in series determine the operating DC voltage of the

system, while the parallel connection determines the capacity of the array [18]. Therefore, the final DC voltage and current of the PV array can be written as Eq. (2.13) and Eq. (2.14) respectively:

$$V_{PV_{Array}} = N_{PV_{series}} \cdot V_{PV} \tag{2.13}$$

$$I_{PV_{Array}} = N_{PV_{parallel}} \cdot I_{PV} \tag{2.14}$$

where $N_{PV_{series}}$ is the number of panels connected in series and $N_{PV_{parallel}}$ is the number of panels connected in parallel.

2.3.7 PV characteristic curves

The I-V curve of the PV panel is given by the superposition of the diode current generated by the incident light plus the current flowing through the resistances [15]. It is characterized by three points: (*i*) short-circuit current, I_{SC}; (*ii*) open-circuit voltage, V_{OC}; and (*iii*) the current and voltage maximum power point, I_{MPP} and V_{MPP}, respectively [17].

Equation (2.10) can be written for *short circuit condition* as Eq. (2.15).

$$I_{sc} = I_{ph} - I_0 \cdot \left[\exp\left(\frac{(V_{sc} + I_{sc} \cdot R_s)}{V_t} \right) - 1 \right] - \frac{V_{sc} - I_{sc} \cdot R_s}{R_{sh}} \tag{2.15}$$

At *short circuit point* ($V_{sc} = 0$) Eq. (2.15) can be written as Eq. (2.16).

$$I_{sc} = I_{ph} - I_0 \cdot \left[\exp\left(\frac{(I_{sc} \cdot R_s)}{V_t} \right) - 1 \right] - \frac{I_{sc} \cdot R_s}{R_{sh}} \tag{2.16}$$

For *open circuit condition* Eq. (2.10) can be expressed as Eq. (2.17).

$$I_{oc} = I_{ph} - I_0 \cdot \left[\exp\left(\frac{(V_{oc} + I_{oc} \cdot R_s)}{V_t} \right) - 1 \right] - \frac{V_{oc} - I_{oc} \cdot R_s}{R_{sh}} \tag{2.17}$$

And at *open circuit voltage point* ($I_{oc} = 0$), Equation (2.17) can be written as Eq. (2.18).

$$0 = I_{ph} - I_0 \cdot \left[\exp\left(\frac{V_{oc}}{V_t} \right) - 1 \right] - \frac{V_{oc}}{R_{sh}} \tag{2.18}$$

The maximum power point (MPP) depends on the solar radiation G and the cell temperature, see Figure 2.6 and Figure 2.7. At MPP the voltage and current of the PV panel are equals to $V_{PV} = V_m$ and $I_{PV} = I_m$ respectively. Therefore, Equation (2.10) can be written as Eq. (2.19).

$$I_m = I_{ph} - I_0 \cdot \left[\exp\left(\frac{(V_m + I_m \cdot R_s)}{V_t} \right) - 1 \right] - \frac{V_m - I_m \cdot R_s}{R_{sh}} \tag{2.19}$$

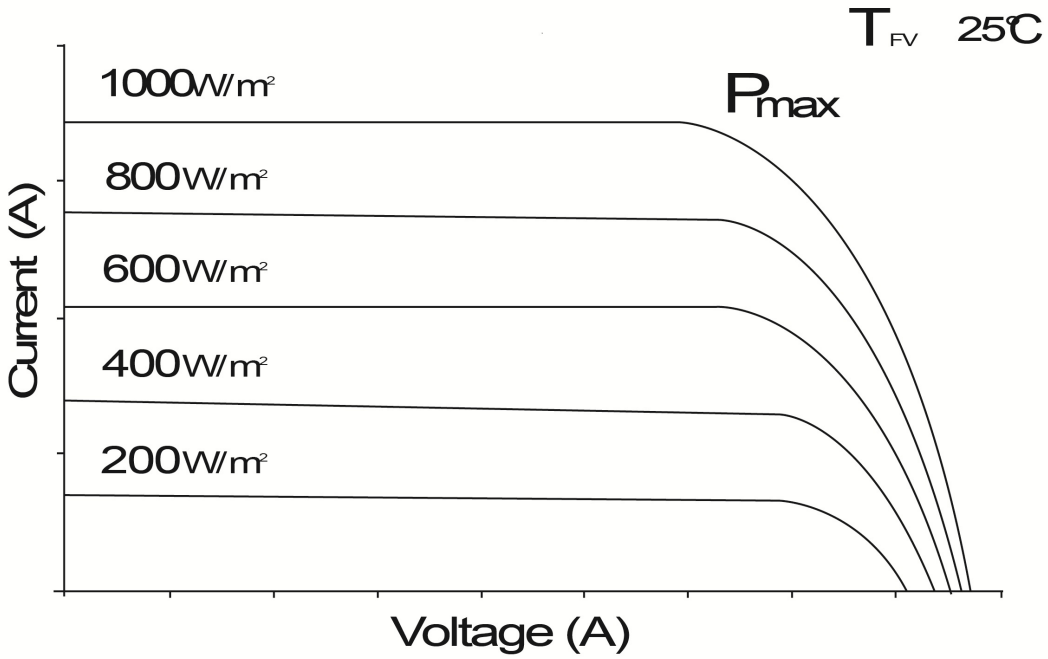

Figure 2.6: I-V characteristic of PV panel depending on irradiance and temperature at $T = 25$ °C.

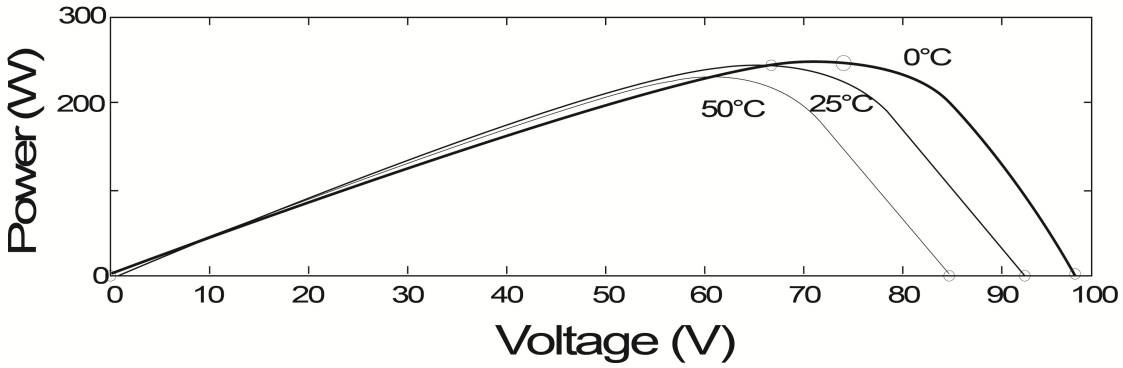

Figure 2.7: *V-P* characteristic of PV panel under different levels of radiation and temperature at $T = 25°C$.

In the presented work is implemented initially the dynamic model in order to build the look-up table of solar irradiation and temperature in function of the active power generated from photovoltaic system, then, in the second part, the model is changed to the simplified model which allows a reduction of the computational times and an easy integration with other submodels.

2.4 Wind turbine System

The turbine produces on average more than 8 kWh of electricity per day, equivalent to half the annual consumption of a typical demand. This value was obtained from the actual amount of electricity produced by the turbine in one year divided by the number of days per year. The main features of the wind turbine are summarized in Table 2.2.

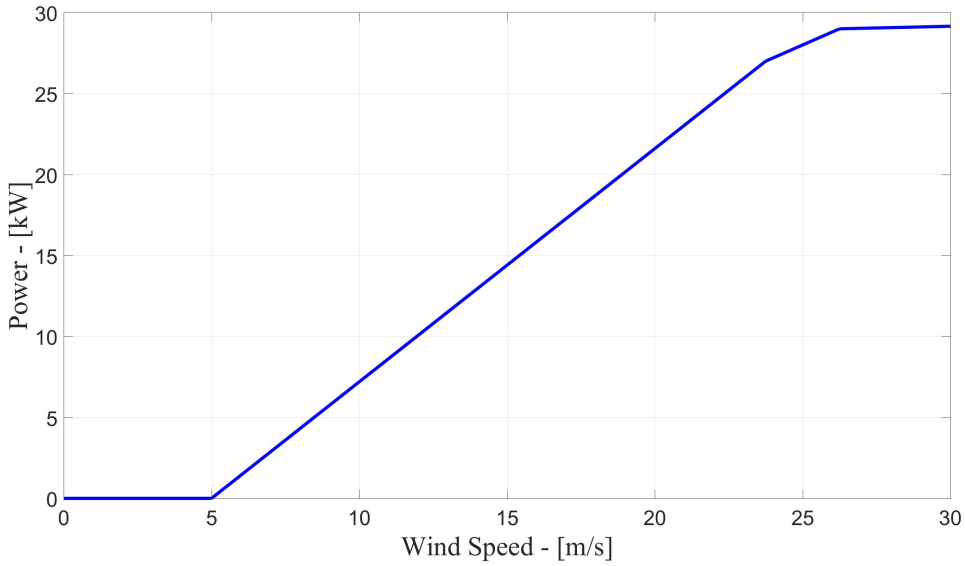

Figure 2.8: Power curve of wind turbine.

Figure 2.8 shows the power curve of the wind turbine.

Table 2.2: Parameters of wind turbine

Characteristic	**Unit**	**Value**
Cut in speed	6	m/s
Cut out speed	30	m/s
Rated speed	15	m/s
Rated power	15	kW

2.5 Modeling Wind Power System

Wind is a natural phenomenon related to the movement of air masses. It is caused primarily by the difference of solar heating on the earth's surface. This phenomenon is derived from solar energy, and only about 1 to 2 percent of the energy emitted by the sun can be converted into wind energy.

The kinetic energy contained in the wind is transformed in part into mechanical energy by the turbine, and then into electrical energy by the generator, also called aero-generator. Aero-generators capture the wind kinetic energy in a rotor consisting of two or more blades

mechanically coupled to an electrical generator. An important factor in how much power the wind turbine will produce is the height of the tower hence the turbine is mounted on a tall tower to enhance the energy capture [16]. There are three main factors which determine the power output of a whole wind energy conversion system:

1. *Power output curve*, determined by aerodynamic power efficiency, mechanical transmission η_n and converting electricity efficiency η_g of a chosen wind turbine [18];
2. *wind speed distribution*;
3. *hub height* of wind tower.

The performance of the turbine cannot be represented only by one parameter (wind speed). It is necessary to take into account other parameters: (*i*) height of the site, (*ii*) air temperature, (*iii*) electrical and control system considerations

2.5.1 Output of Wind Turbine

The output of the wind turbine is modeled as a DC current I_{wind}, which is given by Eq. (2.20).

$$I_{wind} = \frac{P_{wind}}{V_{wind}} \tag{2.20}$$

where V_{wind} is the voltage rating in V and P_{wind} is the power output in W [19], [20].

2.5.2 Wind Speed Variation with Height

Generally, two mathematical models can be used to model the vertical profile of wind speed over regions of homogeneous flat terrain. The the first approach is the log law, has its origins in boundary layer flow in fluid mechanics and in atmospheric research, while a second approach is the power law which is widely applied by researchers. The low law is represented by Eq. (2.21).

$$U(h) = U(ref) \cdot \frac{\ln\left(\frac{h}{z_0}\right)}{\ln\left(\frac{h_{ref}}{z_0}\right)} \tag{2.21}$$

where the parameter z_0 represents the roughness which defines the dependence of the height and the hub with the type of terrain.

In the second approach, the power law is represented with Eq. (2.22). Wind velocity changes with hub height and available wind data. The net hourly wind velocity is given by Eq. (2.22).

$$\nu = \nu_{ref} \cdot \left(\frac{H_{wt}}{H_{ref}} \right)^{\alpha} \tag{2.22}$$

where H_{wt} is the hub height of the wind turbine and H_{ref} is the reference hub height considered to obtain the wind velocity data, ν_{ref}, ν is the wind speed at the hub height H_{wt}, α is the power law exponent which varies with parameters such as elevation, time of day, season, nature of the terrain, wind speed, and temperature [13]

2.5.3 Turbine Models

The model of the wind turbine can be described either general or simplified model. In the follow both models they are presented.

General Model

The wind power is the derivative of the kinetic energy of a moving mass defined by: (*i*) air density named ρ (ρ's value is about 1.225 kg/m^3 at sea level and temperature of 15 °C), (*ii*) the surface swept by the rotor S, and (*iii*) the wind speed ν_{wind}. They allow the determination of the wind power P_{wind} which is represented by Eq. (2.23) [4].

$$P_{wind} = \frac{1}{2} \cdot \rho \cdot S \cdot \nu^3 \tag{2.23}$$

Another important factor is the coefficient of power. It allows to define the performance of the turbine. The coefficient of power is calculated as the ratio between the mechanical power P_{mec} generated by the blades and the power of the wind P_{wind} as Eq. (2.24).

$$C_p = \frac{P_{mec}}{P_{wind}} \tag{2.24}$$

So, substituting Eq. (2.23) on Eq. (2.24) the coefficient of power can be written as shown in Eq. (2.25).

$$C_p = \frac{P_{wind}}{\frac{1}{2} \cdot \rho \cdot S \cdot \nu^3} \tag{2.25}$$

It should be stressed that each turbine is characterized by its performance curve. This represents the coefficient of power as function of the ratio between the peripheral speed at the tip of the blades and the wind speed, called tip speed ratio. Equation (2.26) describes the performance coefficient of the wind turbine

$$\lambda = \frac{V}{U} = \frac{\omega \cdot R}{U} \tag{2.26}$$

where ω is the angular speed in rad/s, R is the radius or length of the blade in m, and U is the wind speed in in m/s.

Simplified Model

On the other hand there is a simplified model. In this model the power output of a wind turbine can be described by Eq. (2.27), Eq. (2.28) and Eq. (2.29).

$$P_w = P_r \cdot \frac{\nu - \nu_c}{\nu_r - \nu_c} (\nu_c <= \nu <= \nu_r) \tag{2.27}$$

$$P_w = P_r \cdot \frac{\nu - \nu_c}{\nu_r - \nu_c} (\nu_c <= \nu <= \nu_r) \tag{2.28}$$

$$P_w(\nu) = 0 (\nu_r <= \nu, and, \nu >= \nu_f) \tag{2.29}$$

where P_r is the rated electrical power of a wind turbine, ν_c is the cut-in wind speed; ν_r is the rated wind speed, ν_f is the cut-off wind speed and ν is the net hourly wind velocity [18].

Analog to the photovoltaic system, in the wind power system is implemented in the first part the dynamic model to build a look-up table of the wind speed in function of the active power generated from the wind turbine, then, in the second part, the model is changed to the simplified model.

2.6 Alkaline Electrolyzer

Electrolyzers are devices used for dissociating water molecules into hydrogen and oxygen. Currently there are three main types of water electrolyzers: (i) alkaline, (*ii*) *PEM* and (*iii*) solid oxide. In the system, an alkaline electrolyzer is used for its maturity, cost and availability in the market [5].

An alkaline electrolyzer is a type of electrolyzer where the electrolyte is an alkaline solution (typically *KOH* 30 wt %). The electrolyzer of the $H\mu G$ has a maximum power input of 8 kW, with a nominal hydrogen production of 1.255 Nm^3/h. The outlet hydrogen delivering pressure is 12 barg, reaching a purity of 99.3-99.8 %. The electrolyzer comprises one stack of 8 kW composed by 5 cells connected in series. Its average performance efficiency is around 54.4 % referred to low heating value. The electrolyzer specifications are presented in Table 2.3.

Table 2.3: Parameters of alkaline electrolyzer

Characteristic	**Value**	**Unit**
Power	8	kW
Nominal voltage	45	V
Nominal current	130	A
Minimum Power	2	kW
Pressure	12	barg
H2 production	1.255	Nm^3/h
Electrolyte	*KOH* 30	%
Operation temperature	31	C
Cells	5	-
Electrode area	0.15	m^2

2.7 Modeling Alkaline Electrolyzer

An electrolyzer uses electricity to break the water into hydrogen and oxygen. There are different types of electrolyzers, the most commons are classified as: (*i*) *PEM electrolyzer* and (ii) *alkaline electrolyzer*. Traditionally, in conventional alkaline electrolyzers is used aqueous potassium hydroxide electrolyte *KOH*, where the potassium ion K^+ and OH^- take care of the ionic transportation [3].

2.7.1 Splitting-Water Process

The decomposition of water into hydrogen and oxygen can be achieved by passing an electric *DC* current between two electrodes separated by an aqueous electrolyte with good ionic conductivity. To make see the reaction occurring a minimum electric voltage must be applied to the two electrodes. In Figure 2.9 is represented the operation principle of an alkalyne electrolyzer.

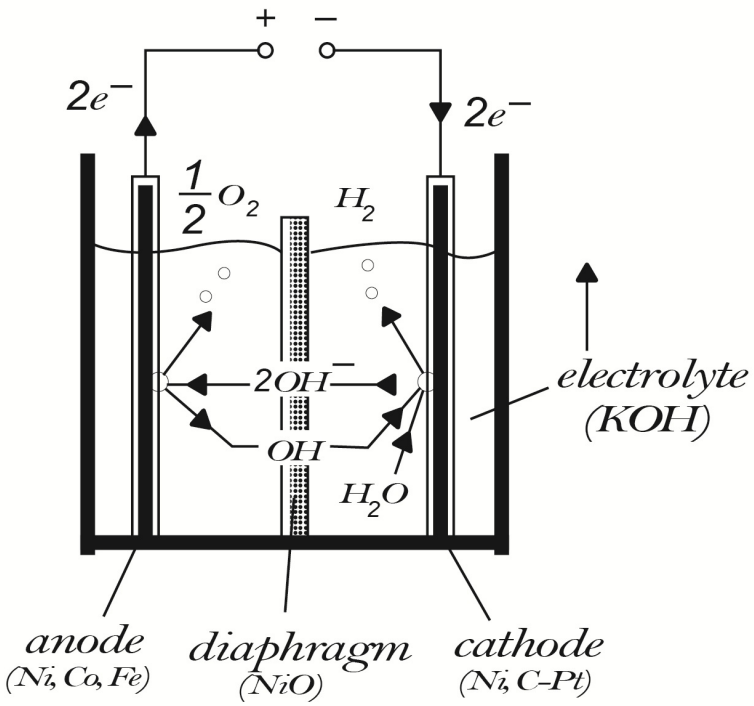

Figure 2.9: Operation principle of an alkalyne electrolyzer.

The overall reaction for splitting water is shown in Eq. (2.30):

$$H_2 \cdot O(1) + ElectricalEnergy \rightarrow H_2(g) + \frac{1}{2} \cdot O_2(g) \tag{2.30}$$

The anodic and cathodic reactions are described by Eq. (2.31) and Eq. (2.32) respectively:

$$Anode : 2OH^-(aq) \rightarrow \frac{1}{2} \cdot O_2(g) + 2e^- \tag{2.31}$$

$$Catod : 2H_2O(1) + 2e^- \rightarrow H_2(g) + 2OH^-(aq) \tag{2.32}$$

The electrodes must be resistant to corrosion and they must have good electric conductivity and catalytic properties, as well as good structural integrity, while the diaphragm should have low electrical resistance. This can, be achieved for instance, by using different materials. Anodes may be based on nickel Ni, cobalt Co, and iron Fe. Where cathodes may be based on Ni with a block of platinum activated carbon catalyst CPt, and nickel oxide NiO diaphragms.

For the water-splitting, the following assumptions are considered:
1. Hydrogen and oxygen are ideal gases.
2. Water is an in-compressible fluid.
3. Gas and liquid phases are separated.

2.7.2 Alkaline Electrolyzer Design

Physically, an electrolyzer stack consists of several cells linked in series. There are three different cell designs to study alkaline electrolyzer; (*i*) *Monopolar electrolyzer*, (*ii*) *Bipolar electrolyzer*, and (*iii*) *Advanced alkaline electrolyzers* [3].

Monopolar Electrolyzer

The first design for electrolyzer is the monopolar type. In this case the electrodes are either negative or positive with parallel electrical connection with individual cells. In Figure 2.10 is shown the monopolar electrolyzer design.

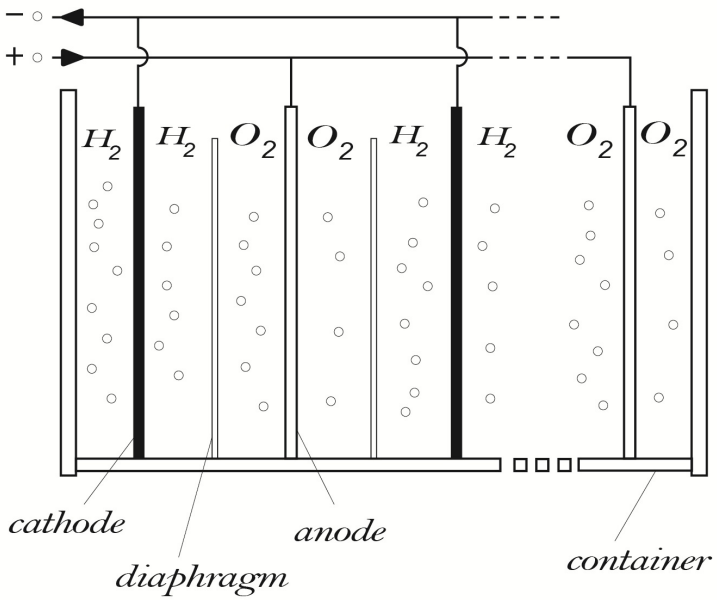

Figure 2.10: Monopolar alkaline electolyzer design.

Bipolar Electrolyzer

The second design type is the bipolar electrolyzer shown in Figure 2.11. It is the most manufactured today and it is more complex than monopolar electrolyzers. Therefore, it has a relative higher cost of manufacturing. In the bipolar electrolyzer, the individual cells are connected in series electrically and geometrically. One important advantage of this design is its compaction in stacks, which allows a shorter current paths in the electrical wires electrodes. This reduces the losses due to the internal ohmic resistance and this leads to an efficiency increase.

The main disadvantages are the parasitic currents and corrosion problems. Furthermore, the compactness and high pressures of the bipolar electrolyzers require relatively sophisticated and complex system designs, which increase the manufacturing costs.

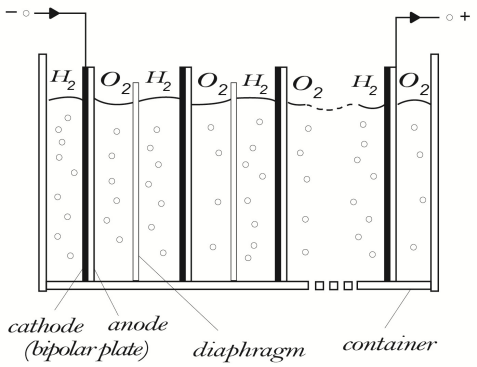

Figure 2.11: Bipolar alkaline electolyzer design.

Advanced Alkaline Electrolyzer

The last category is the the advanced alkaline electrolyzer. In this case, the operational cell voltage is reduced and the current density is increased compared to the more conventional electrolyzers. and with respect to the traditional electrolyzers, advanced designs have considerable advantages. They lead to a reduction of the operational and investment cost. However, the increase of the current density increases the ohmic resistance in the electrolyte temperature due to a variation of the gas bubbling. Hence, an increase of the current density leads to high over-potentials levels at the anodes and cathodes. As it concerns to design, there are three basic improvements implemented:

1. New cell configurations to reduce the surface-specific cell resistance despite increased current densities
2. Higher process temperatures (up to 160 °C) to reduce the electric cell resistance in order to increase the electric conductivity of the electrolyte
3. New electrocatalysis to reduce anodic and cathodic over-potentials

2.7.3 Model Description

The alkaline electrolyzer model presented is related to an *Advanced Alkaline Electrolyzer*. It describes with accuracy the electrochemical and thermal dynamic behavior is based on a combination of fundamental thermodynamics, heat transfer theory and empirical electrochemical relationships. In particular, the electrochemical model is based on temperature and pressure depending on Faraday efficiency relation and a temperature depending of current-voltage. [3], [21].

The model can be used to predict: (*i*) the cell voltage, (*ii*) hydrogen production, (*iii*) Faraday efficiency, and (*iv*) operating temperature. [3]. In Figure 2.12 is presented the

block diagram of the sub models.

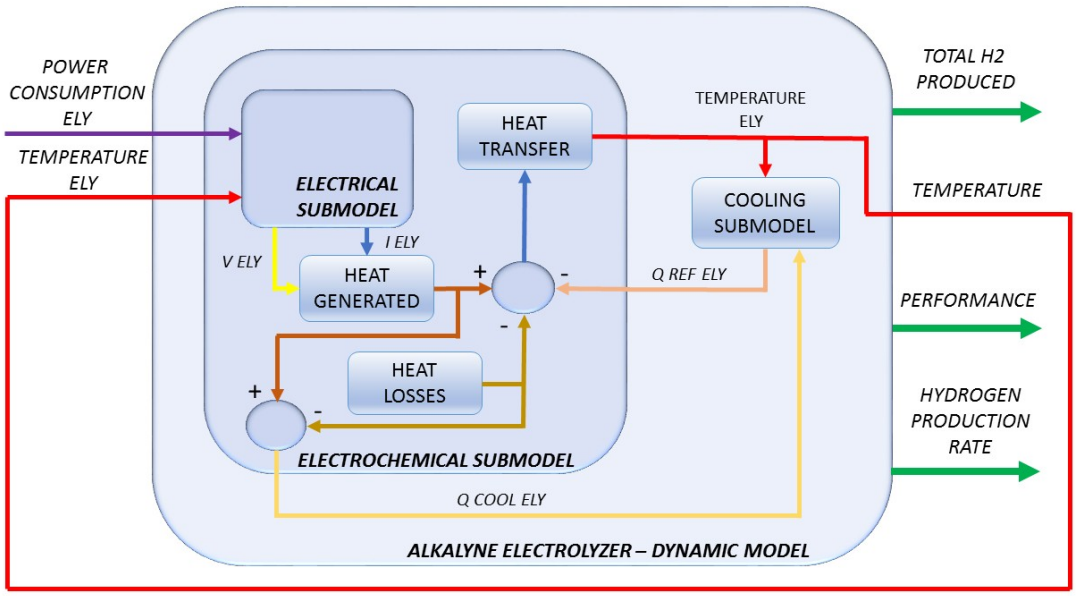

Figure 2.12: Block diagram of sub models for an advanced alkaline electrolyzer.

In the follow, the sub-models to modeling the advance alkaline electrolyzer are described. The operation of the whole electrolyzer is based on the interaction between the follow sub-models:

1. Thermodynamic Model
2. Electrical Sub-Model.
3. Hydrogen Production Sub-Model.
4. Thermal Sub-Model.

Thermodynamic Model

The reversible voltage is the minimum voltage that must be applied to slit the water molecule. In thermodynamic terms, the reversible voltage U_{rev} can be expressed as a function of the Gibbs Energy. With Gibbs energy can be determined the minimum voltage or reversible voltage that must be applied to occur splitting water reaction. The Faraday's law relates the electrical energy or electromotive force needed to split the water to the chemical conversion rate in molar quantities.

Thermodynamics provides a framework for describing equilibrium reaction and thermal effects in electrochemical reactors. It also gives a basis for the definition of the driving forces for transport phenomena in electrolytes and leads to the description of the properties of the electrolyte solutions.

Based on the assumptions done before for Advanced Alkaline Eltrolyzer, the change in enthalpy ΔH, entropy ΔS, and Gibbs energy ΔG of the water-splitting reaction can be calculated with reference to pure hydrogen (H_2), oxygen (O_2), and water (H_2O) at standard temperature and pressure. Specifically at 25 °C and 1 bar.

The total change in enthalpy for splitting water is the enthalpy difference between the products H_2 and O_2 and the reactants H_2O. The same applies to the total change in entropy. The change in Gibbs energy is expressed by Eq. (2.33).

$$\Delta G = \Delta H - T \cdot \Delta S \tag{2.33}$$

The Gibbs energy can be associated with reversible voltage and themoneutral cell voltage as shown in Eq. (2.34).

$$U_{rev} = \frac{\Delta G}{z \cdot F} \tag{2.34}$$

where the reversible voltage U_{rev} depends on the temperature and pressure of the reaction and it is measured in V, z is the number of electrons per hydrogen molecule, and F[1] is the Faraday constant in sA/mol.

The total energy demand ΔH is related to the thermoneutral cell voltage and it is expressed by Eq. (2.35)

$$U_{th} = \frac{\Delta H}{z \cdot F} \tag{2.35}$$

[1]Faraday Constant = 96485.3329 sA/mol

Electrical Submodel

The electrical submodel allows the estimation of the voltage-current relationship. The proposed model uses the electrical power and stack temperature as the electrical inputs calculating the voltage-current for each cell of the stack at different temperatures [2].

The relationship of the electrical power on the electrolyzer is given Eq. (2.36):

$$W = N_{ez}^{(st)} \cdot I_{ez}^{(st)} \cdot U_{cell} \tag{2.36}$$

where W is the electrolyser power consumption in W, $N_{ez}^{(st)}$ is the number of stacks cells, $I_{ez}^{(st)}$ is the stack current of the electrolyser in A, U_{cell} and is the electrolyser cell voltage in V.

In Eq. (2.36), the electrolyser cell voltage U_{cell} represents an empirical $I-U$ model for electrolyzers. The kinetics of the cell electrode are modeled with the $I-U$ curve that takes into account overvoltages, ohmic resistance and temperature on the stack cell. The current-voltage curve can be expressed by the sum of three terms, as Eq. (2.37): (*i*) reversible voltage U_{rev}, (*ii*) activation voltage U_{act}, and (*iii*) ohmic overvoltage U_{Ohm}. All the terms are expressed in V [22].

$$U_{cell} = U_{rev} + U_{Act} + U_{Ohm} \tag{2.37}$$

The first term of Eq. (2.37) represents the minimum electric voltage that must be delivered to the electrolyzer, expressed above in Eq. (2.34). The second and third terms express the activation and ohmic overvoltages that can be defined as in Eq. (2.38) and Eq. (2.39), respectively.

$$U_{act} = s \cdot log\left(\frac{t}{A_{ez}^{(st)}} \cdot I_{ez}^{(st)} + 1\right) \tag{2.38}$$

$$U_{Ohm} = \frac{r}{A_{ez}^{(st)}} \cdot I_{ez}^{(st)} \tag{2.39}$$

Inserting equations (2.34), (2.38) and (2.39) in Eq. (2.37), U_{cell} can be written as shown in Eq. (2.40):

$$U_{cell} = U_{rev} + \frac{r}{A_{ez}^{(st)}} \cdot I_{ez}^{(st)} + s \cdot \log\left(\frac{t}{A_{ez}^{(st)}} \cdot I_{ez}^{(st)} + 1\right) \tag{2.40}$$

where as mentioned before, U_{rev} is the reversible voltage, r is the parameter related to ohmic resistance of electrolyte in $\Omega \cdot m^2$, $A_{ez}^{(st)}$ is the electrolyser stack area in m^2 , s is the coefficient for overvoltage on electrodes in V, and t is also a coefficient for overvoltage on electrodes but in measured in $A^{-1} \cdot m^2$.

In Eq. (2.40), the terms r, s and t define the stack and the electrolyte type and the shape of the $U - I$ curve. These parameters are expressed by Eq. (2.41), Eq. (2.42) and Eq. (2.43) respectively [2], [3], [21].

$$r(T_{ez}^{(st)}) = r_0 + r_1 \cdot T_{ez}^{(st)} + r_2 \cdot \left(T_{ez}^{(st)}\right)^2 \tag{2.41}$$

$$s(T_{ez}^{(st)}) = s_0 + s_1 \cdot T_{ez}^{(st)} + s_2 \cdot \left(T_{ez}^{(st)}\right)^2 \tag{2.42}$$

$$t(T_{ez}^{(st)}) = t_0 + \frac{t_1}{T_{ez}^{(st)}} + \frac{t_2}{\left(T_{ez}^{(st)}\right)^2} \tag{2.43}$$

The variables r_0, r_1 and r_2 are expressed in $\Omega \cdot m^2$, $\frac{\Omega \cdot m^2}{K}$ and $\frac{\Omega \cdot m^2}{K^2}$, whereas s_0, s_1 and s_2 are expressed in V, $\frac{V}{K}$ and $\frac{V}{K^2}$. t_0, t_1 and t_2 are in $\frac{m^2}{A}$, $\frac{m^2 \cdot C}{A}$ and $\frac{m^2 \cdot K^2}{A}$ respectively.

Equation (2.42) can be rewritten as into a more detailed $I - U$ model, as follows in Eq. (2.44):

$$\begin{aligned} U_{cell} = U_{rev} + \frac{r_0 + r_1 \cdot T_{ez}^{(st)} + r_2 \cdot \left(T_{ez}^{st}\right)^2}{A_{ez}^{(st)}} \cdot I_{ez}^{(st)} + \\ \left(s_0 + s_1 \cdot T_{ez}^{(st)} + s_2 \cdot \left(T_{ez}^{(st)}\right)^2\right) \cdot \log\left(\frac{t_0 + \frac{t_1}{T_{ez}^{(st)}} + \frac{t_2}{\left(T_{ez}^{(st)}\right)^2}}{A_{ez}^{(st)}} \cdot I_{ez}^{(st)} + 1\right) \end{aligned} \tag{2.44}$$

Hydrogen production sub-model

In an electrolyzer cell the hydrogen production rate is directly proportional to the electrical current in the external circuit (transfer rate of electrons to electrodes):

$$m_{H_2} = \eta_F \cdot \frac{N_{ez}^{(st)} \cdot I_{ez}^{(st)}}{z \cdot F} \tag{2.45}$$

where m_{H_2} is the hydrogen flow rate in mol/s, η_F is the Faraday efficiency, and $I_{ez}^{(st)}$ is the stack current in A.

Faraday Efficiency Model

The Faraday efficiency represents the losses caused by parasitic currents. The parasitic currents increase with decreasing current densities due to an increasing share of electrolyte and a lower electrical resistance. An increase of temperature leads to a lower resistance, more parasitic currents losses, and lower Faraday efficiencies. Faraday efficiency is expressed as in Eq. (2.46):

$$n_F(\rho, T) = f_2(T_{ez}^{(st)}) \cdot \frac{\rho^2}{\rho^2 + f_1(T_{ez}^{(st)})} \tag{2.46}$$

Where f_1 and f_2 are empirical constants taken from [23], and ρ is the current density expressed by Eq. (2.47):

$$\rho = \frac{I_{ez}^{(st)}}{A_{ez}^{(st)}} \tag{2.47}$$

Thermal Model

The thermal inertia is important when the electrolyzer is connected to renewable energy sources, because operating temperature changes with time, and therefore, hydrogen production.

The temperature of the electrolyte can be determined using a simple or complex method. In the overall thermal energy, the thermal capacity Ct_{ez} and resistance R_t are

constants that can be determined analytically or empirically, depending to the model.

The thermal energy balance can be expressed as Eq. (2.48):

$$Ct_{ez}\frac{dT_{ez}^{(st)}}{dt} = \dot{Q}_{ez}^{(Gen)} - \dot{Q}_{ez}^{(Cool)} - \dot{Q}_{ez}^{(Loos)} \tag{2.48}$$

Where Ct_{ez} is the electrolyser stack thermal capacity in W/K , $T_{ez}^{(st)}$ is the electrolyser temperature in K, $\dot{Q}_{ez}^{(Gen)}$ is the heat generated in the electrolysis process in watts, $\dot{Q}_{ez}^{(Cool)}$ is the cooling flux in W, and $\dot{Q}_{ez}^{(Loos)}$ is the heat losses in W. All the variables are calculated as shown in equations (2.49), (2.51) and (2.52):

$$\dot{Q}_{ez}^{(Gen)} = N \cdot U_{ez}^{(st)} \cdot I_{ez}^{(st)} \cdot (1 - \eta_e) \tag{2.49}$$

$$\dot{Q}_{ez}^{(Cool)} = C_{cw} \cdot (T_i^{(cw)} - T_o^{(cw)}) = UA_{hx} \cdot LMTD \tag{2.50}$$

$$LMTD = \frac{(T_{ez}^{(st)} - T_i^{(cw)}) - (T_{ez}^{(st)} - T_o^{(cw)})}{ln[(T^{(st)} - T_o^{(cw)})/(T^{(st)} - T_o^{(cw)})]} \tag{2.51}$$

$$\dot{Q}_{ez}^{(Loos)} = \frac{1}{R_t} \cdot (T_{ez}^{(st)} - T_a) + h_{ez}^{(f)} \cdot (T_{ez}^{(st)} - T_a) + h_{ez}^{(n)} \cdot (T_{ez}^{(st)} - T_a) \tag{2.52}$$

where $U_{(st)}^{ez}$ is the stack voltage of the electrolyzer in V, η_e is the energy efficiency of the process, $T_i^{(cw)}$ and $T_i^{(cw)}$ are the temperatures of the inlet and outlet cooling water respectively, C_{cw} is the thermal capacity of the water, AU_{hx} is the overall heat transfer coefficient-area product for heat exchanger in K/W, $LMTD$ is the log mean temperature difference in K, R_t is the thermal resistance in W/K, T_a is the environment temperature (assumed at 298 K), and h_f^{ez} and h_n^{ez} are the film coefficient for forced convection and film coefficient for natural convection of the electrolyer respectively.

2.8 PEM Fuel Cell

The *PEM* fuel cell (*FC*) consists of an electrolyte (membrane) conductor ions, a porous anode and cathode, which converts energy from chemical reactions into electrical energy. For a *PEM* fuel cell, the combination of fuel (hydrogen) with oxidizer (oxygen) continuously produces electricity, heat and water [5]. The fuel cell stacks reunite several cells

in series to obtain higher voltages and powers thus forming modules with outputs ranging from hundreds of watts to ten of hundreds of kilowatts with a efficiency around 40-60 %.

A 12.5 kW *PEM* fuel cell system is composed by one stacks of 110 cells. The *PEM* fuel cell is auto-humidified and takes the oxygen from air. The fuel cell specifications are summarized Table 2.4.

Table 2.4: Parameters of the *PEM* fuel cell

Characteristic	**Value**	**Unit**
Power	12.5	kW
Nominal voltage	83.7	V
Nominal current	150	A
H_2 consumption at rated power	178	lpm
Membrane thickness	178	μm
Nominal air fuel rate	250	lpm
Stack humidity	14	-
Number of cells	110	-
E0 potential at unity activity	1.229	V

2.9 Modeling PEM Fuel Cell

The fuel cell is a reliable energy source that provides electric power using hydrogen [2]. A common technology of fuel cells is the Proton Exchange Membrane (*PEM*), which uses a membrane that converts hydrogen into electric power [16]. In the *PEM* fuel cell, the electrochemical reaction occurs when hydrogen and oxygen are combined to produce electricity [24]. *PEM* electrolysis as a hydrogen production technique has many advantages such as high working current densities, production at high pressure, pure gas generation and compact design. It is a relatively new and promising technology. Modeling this technology has uttermost importance in understanding the operational behavior of a *PEM* fuel cell [25].

2.9.1 PEM Fuel Cell Design

Different existing models can describe with high accuracy the electrochemical process inside the fuel cell, as the model validated in [2]. This model takes into account parameters such as the dynamic of the compressor, the manifold filling dynamics and consequently the reactant partial pressure. Other empirical models presented in the literature can be a solution to characterize the fuel cell with the advantage of fast computational execution.

However, these models have a limited capacity to predict with accuracy the characteristic curve operation.

A key way of representing the fuel cell behavior is given by the operational curve or polarization curve. This curve is a representation of the voltage versus current. The voltage is a function of the reversible cell voltage, activation losses, and concentration losses. In the present model, fluid dynamics inside the cathode and water flooding are neglected. Nevertheless, the model maintains a high accuracy as it includes the cells dependency on temperature, membrane thickness, humidity, and partial gas partial pressure, which are defined as constants [25].

The architecture of the model is analog to the structure of the alkaline electrolyzer (presented before in Figure 2.12), shown for *PEM* fuel cell in Figure 2.13.

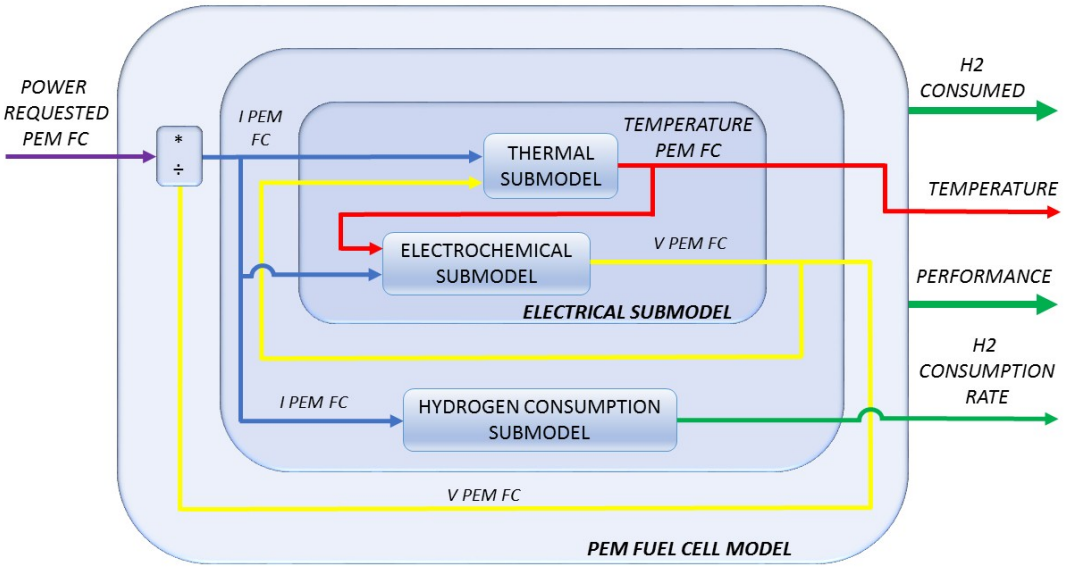

Figure 2.13: Block diagram of submodels for a *PEM* fuel cell.

In the model, the following assumptions are considered:

1. One-dimensional treatment of flow and distribution gases.
2. Ideal and uniformly distributed gases.
3. Constant pressures in the fuel cell gas flow channels .
4. The fuel is humidified pure hydrogen and the oxidant is humidified air.

5. Thermodynamic properties are evaluated at average stack temperature.
6. Temperature variations across the stack are neglected.
7. Stack heat capacity is constant.

2.9.2 Model Description

The presented model based on a semi-empirical model from [2]. It is based on electrical, thermal and flow calculations. The model describes with high accuracy the electrochemical process inside the fuel cell taking into account parameters such as the dynamics of the compressor the manifold filling dynamics and consequently the reactant partial pressures [2].

It is composed by three submodels and each one has its own model which can be run separately, but all the submodels are linked to the other ones. These are:

1. Electrical submodel.
2. Thermal submodel.
3. Hydrogen consumption submodel.

2.9.3 Electrical sub-model.

As the alkaline electrolyzer, the PEM fuel cell model is based on a combination of fundamental thermodynamics, heat transfer theory and empirical relationships [3]. In Eq. (2.53) is expressed the operating cell voltage:

$$V_{cell} = E - V_{act} - V_{ohm} - V_{conc} \tag{2.53}$$

where E is the open circuit voltage, V_{act} is the activation overvoltage, V_{ohm} is the ohmic overvoltage, and V_{conc} is the concentration overvoltage, all terms measured in V. The single models composing electrical sub model are presented in the follow subsections:

Open Circuit Voltage

The open circuit voltage can be calculated by applying the thermodynamic laws to the reaction inside to PEM fuel cell and based on the Nernst equation. Equation (2.54) describes the open circuit voltage E:

$$E = c_1 - c_2 \cdot 10^{-4} \cdot (T_{fc}^{(st)} - c_3) + c_4 \cdot 10^{-5} \cdot T_{fc}^{(st)} \cdot \ln(P_{H_2} \cdot \sqrt{P_{O_2}}) \tag{2.54}$$

where $T_{fc}^{(st)}$ is the stack temperature of the fuel cell in K and P_{H_2} and P_{O_2} are the hydrogen and oxygen partial pressure respectively in bar. Fuel cells are comprises by a number N_s of cells and thus, the open circuit voltage of the stack E_s is obtained by Eq. (2.55).

$$E_s = N_s \cdot E \tag{2.55}$$

Finally, the complete stack power is given by Eq. (2.56):

$$P_{fc} = N_{cells} \cdot V_{cell} \cdot I_{fc}^{(st)} \tag{2.56}$$

Activation Phenomena

The activation phenomena are due to the kinetics of the electrochemical reactions taking place inside the fuel cell. The transfer of the electrical charge between the chemical species and the electrodes involves an energy demand due to the variation of the Gibbs free energy, occurring at the different process stages [26]. This energy barrier is known as activation energy and it is shown in the form of overvoltage at the electrodes. The overvoltage caused by this phenomenon is known as activation voltages V_{act} and its expression is shown in Eq. (2.57):

$$\begin{aligned} V_{act} = x_1 - c_2 \cdot 10^{-4} \cdot (T_{fc}^{(st)} - c_3) + \\ c_4 \cdot 10^{-5} \cdot T_{fc}^{(st)} \cdot \ln(P_{H_2} \cdot \sqrt{P_{O_2}})[(x_2 \cdot T_{fc}^{(st)} + x_3) \cdot P_{O_2}^2 \\ + (x_4 T_{fc}^{(st)} + x_5) \cdot P_{O_2} + \\ (x_6 T_{fc}^{(st)} + x_7)] \cdot (1 - e^{-x_8 \cdot I_{fc}^{(st)}}) \end{aligned} \tag{2.57}$$

Where, $I_{fc}^{(st)}$ is the stack current of the fuel cell in A.

Ohmic Phenomena

The third term of Eq. (2.53), describing the ohmic overvoltage V_{ohm}, is presented in Eq. (2.58). The ohmic phenomenon is caused by the resistance of the various fuel cell elements to the flow of ions and electrons. The electrical current flow through the cells leads to voltage losses called ohmic overvoltage [24], therefore, the ohmic overvoltage is proportional to the electrical current flowing through the cell:

$$V_{ohm} = I_{fc}^{(st)} \cdot R_{ohm,i} \tag{2.58}$$

where $R_{ohm,i}$ is the ionic resistance in Ω which can be calculated by Eq. (2.59):

$$R_{ohm,i} = \frac{t_m}{\sigma_m} \tag{2.59}$$

where σ_m is the membrane conductivity. The membrane conductivity can be empirically expressed as a function of humidification/water content in the membrane. It is obtained by Eq. (2.60):

$$\sigma_m = (c_6 \cdot \lambda_m - c_7) \cdot e^{x_9 \cdot \left(\frac{1}{c6} - \frac{1}{T_{fc}^{(st)}} \right)} \tag{2.60}$$

With t_m indicating the membrane thickness in μm and λ_m referring to the stack humidity which varies between 0 (0% humidity) and 14 (100% humidity). Substituting Equations (2.59) and (2.60) on Eq. (2.58), the ohmic overvoltage V_{ohm} can be written as in Eq. (2.61).

$$V_{ohm} = \frac{I_{fc}^{(st)} \cdot t_m}{(c_6 \cdot \lambda_m - c_7) \cdot e^{x_9 \cdot \left(\frac{1}{c6} - \frac{1}{T_{fc}^{(st)}} \right)}} \tag{2.61}$$

Concentration Phenomena

The last term of (2.53), concentration phenomena V_{con} is described on Eq. (2.62).

$$V_{con} = I_{st}^{fc} \cdot \left[(x_{10} \cdot T_{st}^{fc} + x_{11} \cdot P_{O_2}) \cdot \frac{I_{st}^{fc}}{x_{12}} \right]^{x_{13}} \tag{2.62}$$

2.9.4 Thermal sub-model

The fuel cell thermal submodel is determined through a lumped thermal capacitance model. The thermal capacity is defined as the ratio between the quantity of heat energy transferred between the said body and its environment in any process, and the temperature change experienced [24]. The heat generated during the fuel cell operation is due to entropy changes, thus, the first law of thermodynamics is expressed as Eq. (2.63):

$$Ct_{ez}^{(fc)} \frac{dT_{fc}^{(ez)}}{dt} = \dot{Q}_{H_{reac}} - W_{elec} - \dot{Q}_a \tag{2.63}$$

where $\dot{Q}_{H_{reac}}$ describes the enthalpy of the chemical reaction of water formation, W_{elec} is the energy yielded in the form of electricity generation, and $\dot{Q}_a$ is the amount of heat dissipated through convection effects to the environment, which includes the heat removed by the cooling system when the fuel cell reaches the maximum temperature allowed. The terms of Eq. (2.63) can be calculated as equations (2.64), (2.65) and (2.66):

$$\dot{Q}_{H_{reac}} = \frac{-\Delta H_{reac} \cdot I_{fc}^{(st)}}{2 \cdot F} \tag{2.64}$$

$$W_{elec} = V_{fc}^{(st)} \cdot I_{fc}^{(st)} \tag{2.65}$$

$$\dot{Q}_a = (h_{fc}^{(c)} + h_{fc}^{(n)}) \cdot (T_{fc}^{(st)} - T_a) \tag{2.66}$$

where H_{reac} is the enthalpy of the reaction, $h_{fc}^{(n)}$ is the convective heat transfer coefficient in Wm^2/K and, $h_{fc}^{(c)}$ is the natural heat transfer coefficient in Wm^2/K.

2.9.5 Hydrogen Consumption Sub-Model

The hydrogen required for the fuel cell to produce power is calculated through the stoichiometric Eq. (2.67).

$$\dot{m}_{fc} = \frac{N_{cells} \cdot I_{fc}^{(st)}}{z \cdot F} \tag{2.67}$$

where $\dot{m}_{fc}$ is the flow of hydrogen required mol/s, N_{cells} is the number of cells in the fuel cell, $I_{fc}^{(st)}$ is the current delivered by the fuel cell stack A, z is the number of electrons per molecule, and F is the Faraday constant in sA/mol.

2.10 Hydrogen Storage Tank

Hydrogen can be accumulated in different ways: gaseous, liquid or in an intermediate compound. The hydrogen produced by the electrolyser is stored without further compression in a high pressure tank. [27]. The total tank storage capacity is 9 m^3 of hydrogen. Tank specifications are summarized in Table 2.5.

Table 2.5: Parameters of hydrogen storage tank

Characteristic	**Value**	**Unit**
Storage capacity	9	m^3
Maximum level	10	%
Minimum level	95	%

2.11 Hydrogen Storage Tank

The hydrogen storage tank model can be represented by Eq. (2.68).

$$m_{tk} = m_{ez} - m_{fc} - m_{leak} \tag{2.68}$$

where m_{tk} is the hydrogen storage tank level, m_{ez} is the hydrogen production from the electrolyzer, m_{fc} is the hydrogen flow required from the fuel cell, and m_{leak} is the leakage

rate to environmental. Despising the leakage, Eq. (2.68) can be written again as Eq. (2.69).

$$m_{tk} = m_o \cdot \int (m_{ez} - m_{fc}) \cdot dt \tag{2.69}$$

Assuming ideal gas conditions, the pressure inside the tank can be obtained as Eq. (2.70):

$$P_{tk} = \frac{\eta_{tk} \cdot R \cdot T_{tk}}{VL_{tk}} \tag{2.70}$$

where P_{tk} is the pressure in the tank, η_{tk} is the moles of hydrogen into the tank, R is the ideal gas constant, T_{tk} is the temperature of the hydrogen in the tank, and VL_{tk} is the volume of the tank.

Chapter 3

Simulink Models, Testing and Validation

This chapter describes the models implemented in the $H\mu G$. Furthermore, The testing and validation of the major components of the $H\mu G$ is presented t; (*i*) Alkaline electrolyzer, (*ii*) hydrogen storage tank and, (*iii*) *PEM* fuel cell. Below in the sections (3.1) to (3.6) are presented the block diagrams showing the inputs, outputs and representative connections of the composing models. The chapter is composed of the following sections.

1. Load demand.
2. Wind turbine system
3. *PV* system
4. Alkaline electrolyzer.
5. *PEM* fuel cell.
6. Hydrogen storage tank.
7. Central control system.
8. Integrated system simulation.

3.1 Load demand

The load is intended as an input of the $H\mu G$ loaded from a file. It is composed by a selector and a signal builder. According to the position of the selector it is possible to change the characteristic of the load between different profiles. A general scheme of the load model proposed is presented in Figure 3.1.

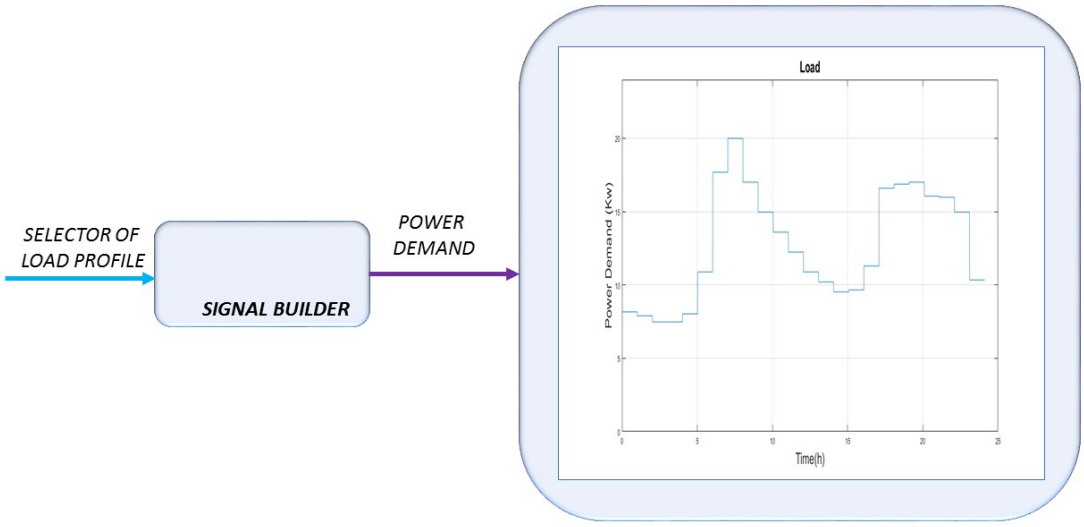

Figure 3.1: Load demand. Model proposed.

The model of the load is implemented in Simulink and it is presented in Figure 3.2. The signal builder contains three strategic profiles that lead to study the performance of the system under different behaviors. The first profile is an unrealistic case. It is built to verify the operation of the system in different scenarios. The other ones are obtained from measurements done in two summer days in an electrical substation of *Politecnico di Torino* with different types of loads. The three profiles: (*i*) validation profile, (*ii*) case 1 - variable load and (*iii*) case 2 - static load, are presented in Figure 3.3 to Figure 3.5.

3.1.1 Measure Descriptions

The measurements performed to build the loads corresponding to cases 1 and 2 are described as follows:

1. **Place**: *Politecnico di Torino*, Piedmont, Italy.
2. **Date**: June 18th and 19th of 2019.
3. **Description**: Summer load profiles measured in two days in an electrical substation of *Politecnico di Torino*.
4. **Instruments**: Data acquisition & analysis (CED), current probe TA 167 Pico technology and current probe Hioki 9018-50.
5. **Sample time**: 1 second (1 Hz).

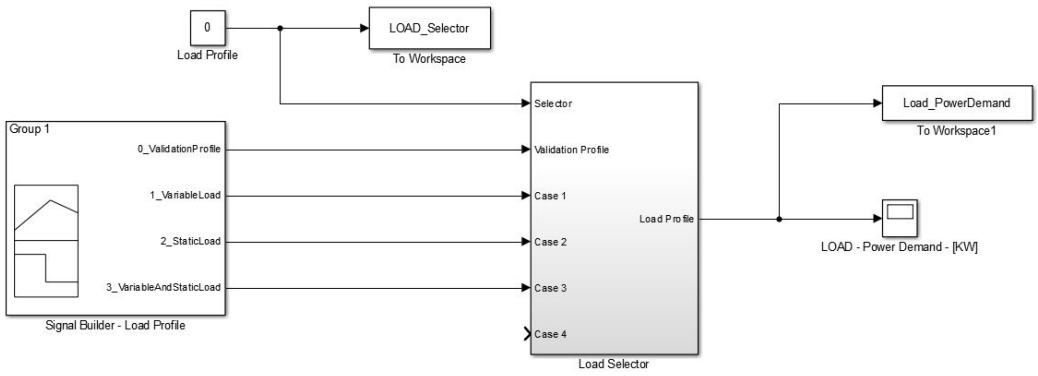

Figure 3.2: Load demand. Simulink model

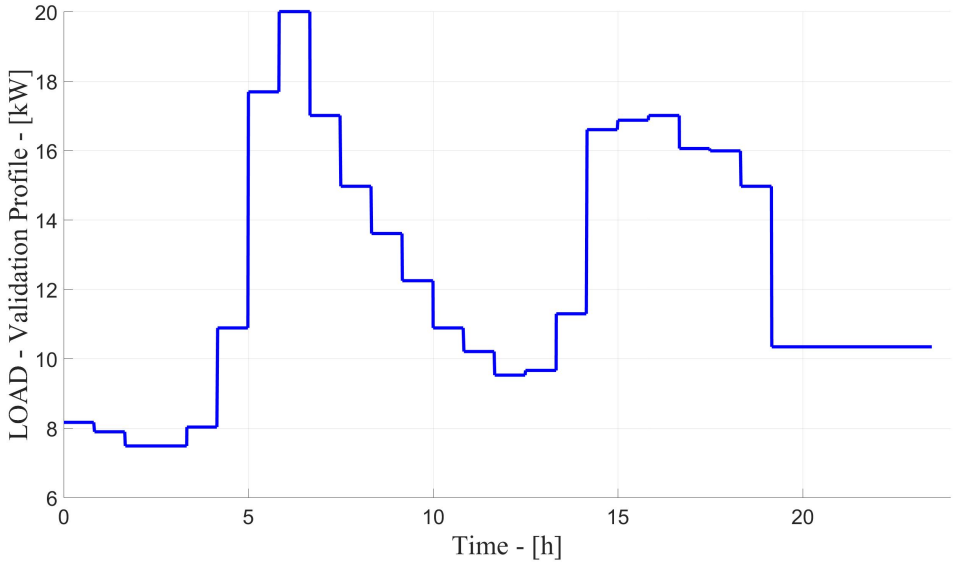

Figure 3.3: Load demand. Validation profile with active power in kW.

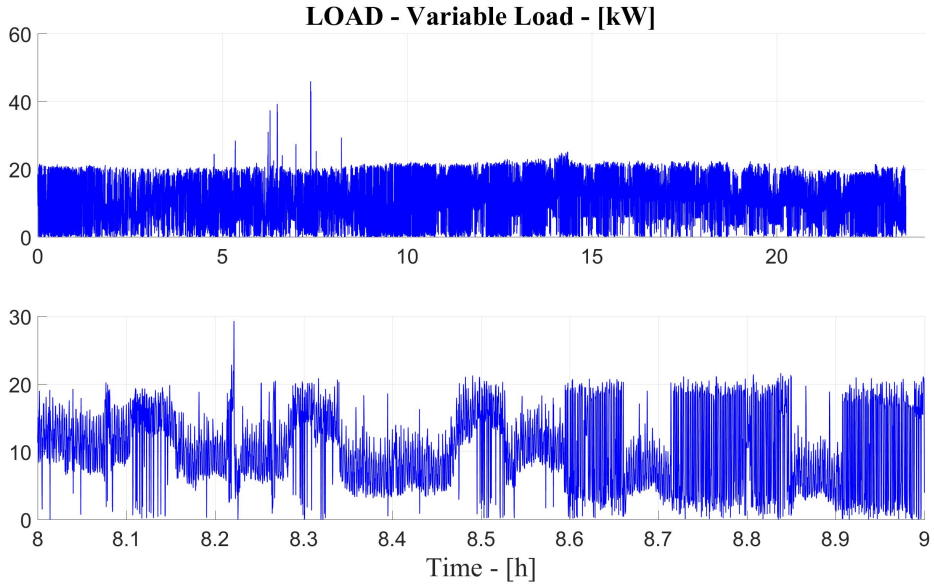

Figure 3.4: Load demand. Variable load measured in an electrical cabin of *Politecnico di Torino* with active power in kW. (*a*) 0 to 24 h, (*b*) 8 to 9 h.

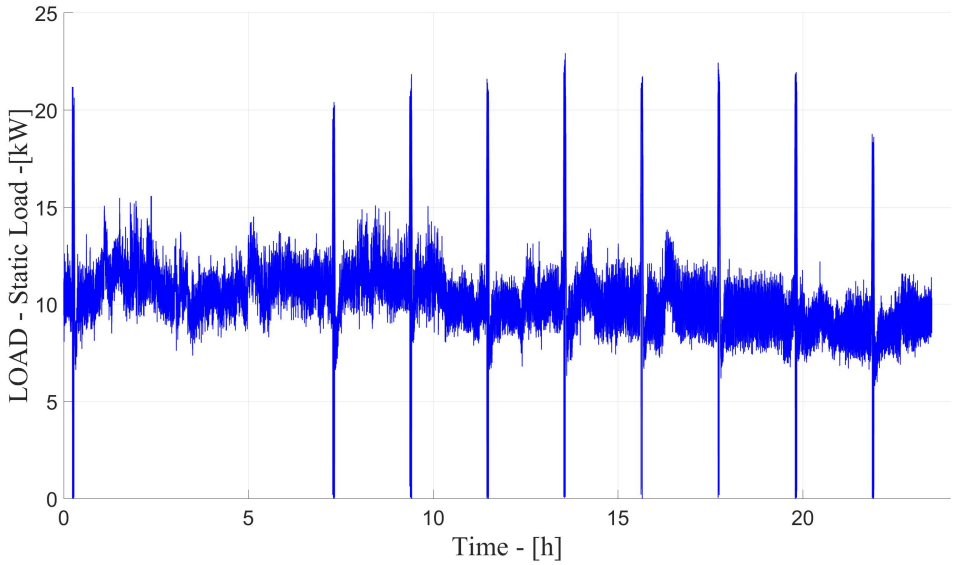

Figure 3.5: Load demand. Static load measured in an electrical cabin of *Politecnico di Torino* with active power in kW.

3.2 Wind turbine generator model

The model of the wind turbine generator is presented in two sections. The first part presents a dynamic model which shows the dynamic of the wind turbine. It is connected to the grid at the point of common coupling (PCC) at 380 V phase-to-phase. The second part presents a simplified model based on Look-up tables exported from the dynamic model.

3.2.1 Dynamic Model

The dynamic model proposed and its Simulink model are presented in Figures 3.6 and 3.8 respectively. It has one input: wind speed in m/s, and six outputs: (i) wind power in kW, (ii) mechanical power in kW, (iii) stator voltage V_{abc} in V, (iv) stator currents I_{abc} in A, (v) active power in kW, and (vi) reactive power in kvar.

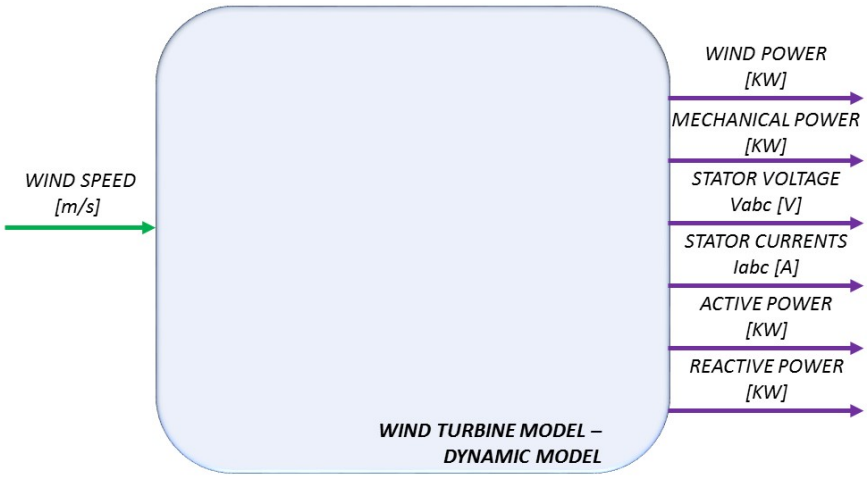

Figure 3.6: Wind turbine generator. Dynamic model proposed.

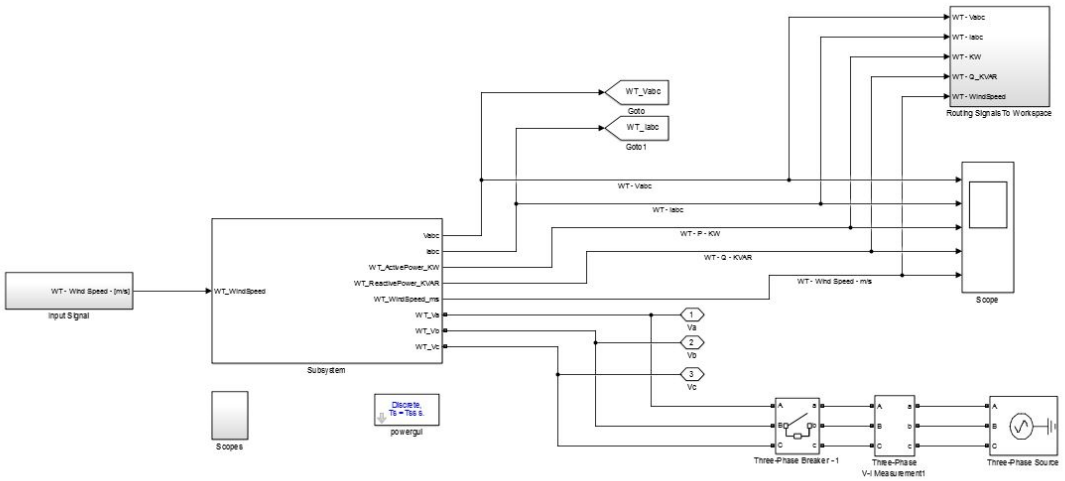

Figure 3.7: Wind turbine generator. Dynamic Simulink model.

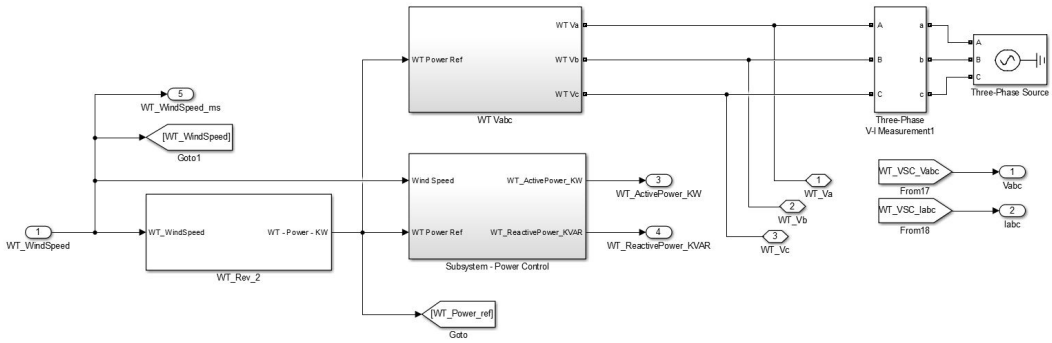

Figure 3.8: Wind turbine generator. Dynamic Simulink model.

The model is validated with a ramp of wind speed starting from 6 m/s and coming to 15 m/s. It covers all the speed compressed between the the cut-on and cut-off speeds of the turbine generator, as shown in Figure 3.9.

The responses of the model are presented in the following order: Figure 3.10 shows stator voltage V_{abc} and stator currents I_{abc}, Figure 3.11 active and reactive power and Figure 3.11 mechanical and wind speed power.

The stator voltage is constant at 380 V phase-to-phase, while the active power varies active power varies from 6 kW at the cut-on speed until 15 kW at the cut-off speed.

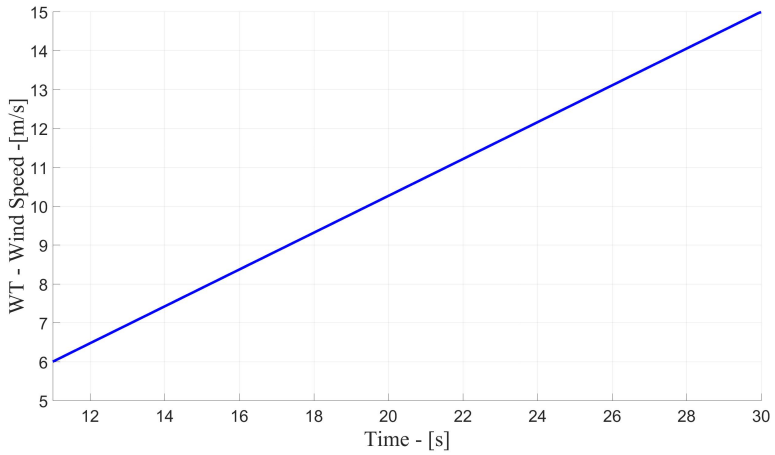

Figure 3.9: Wind turbine generator. Wind speed in m/s.

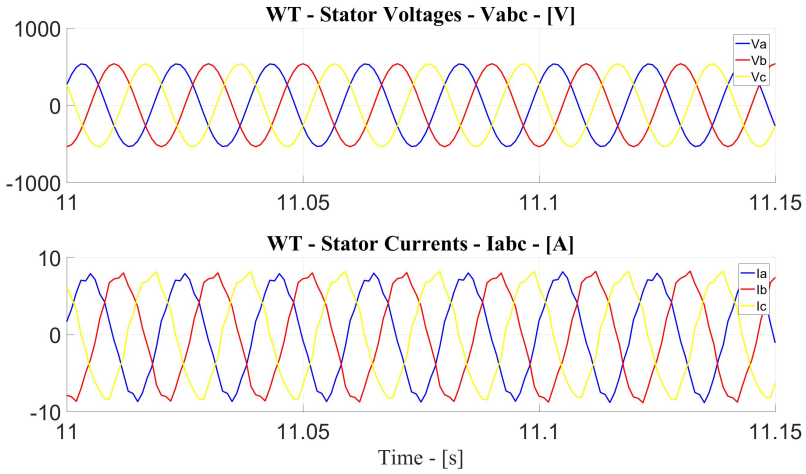

Figure 3.10: Wind turbine generator. (a) Stator voltage V_{abc} in V and (b) stator currents I_{abc} in A.

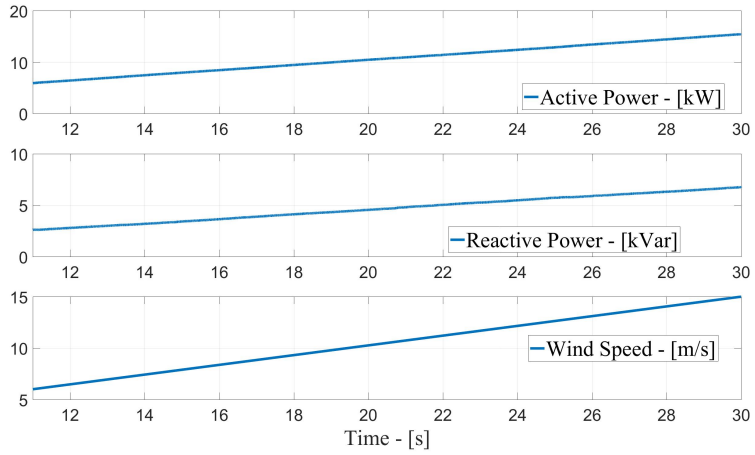

Figure 3.11: Wind turbine generator. Dynamic model. (a) Active power in kW, (b) reactive power in kvar, (c) wind speed in m/s.

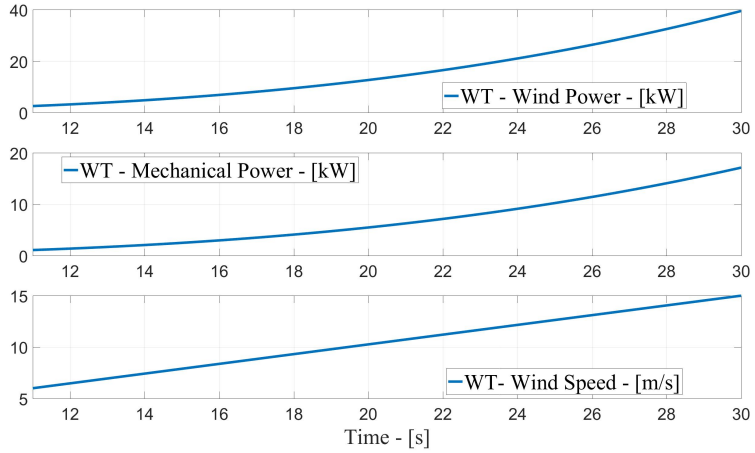

Figure 3.12: Wind turbine generator. Dynamic model. (a) Wind power in kW, (b) mechanical power in kW, (c) wind speed in m/s.

3.2.2 Simplified Model

The high computational time required by the dynamic model led to implement a simplified model in order to simulate long periods of time. Then, results obtained in the validation of the dynamic model are exported as an one dimensional look-up table. i.e. wind speed as input and active power as output. Figures 3.13 and 3.15 presents the simplify model

proposed and its Simulink model.

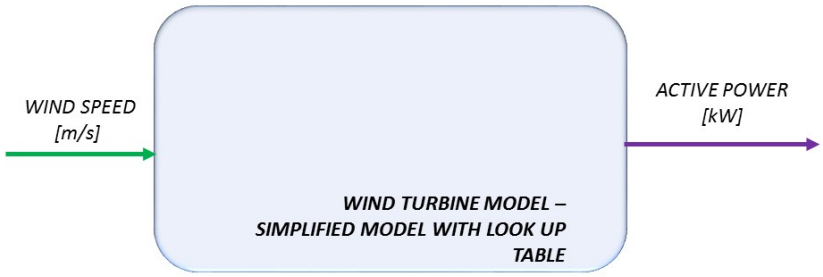

Figure 3.13: Wind turbine generator. Simplified model proposed.

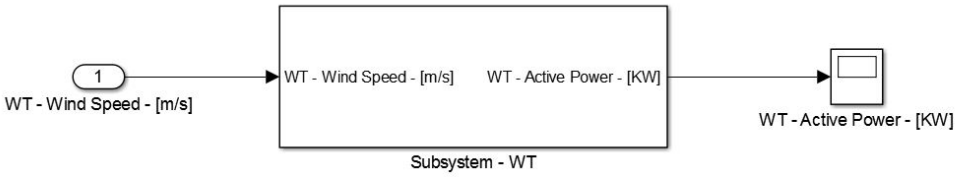

Figure 3.14: Wind turbine generator. Simplified Simulink model.

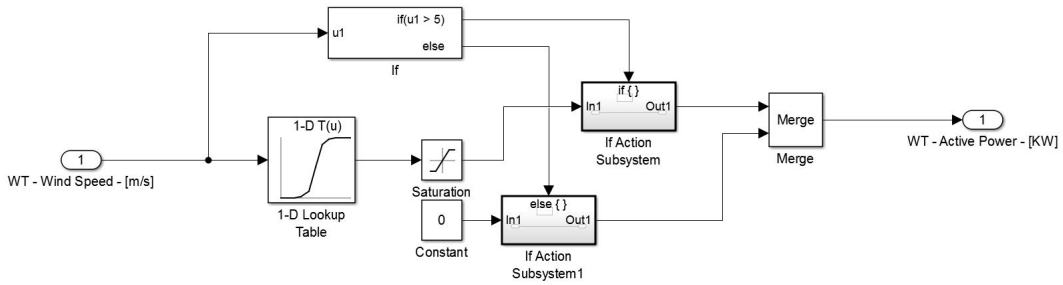

Figure 3.15: Wind turbine generator. Simplified Simulink model.

The response to the ramp of the model based on a look-up table follows the trend and the scale of the original response and its computational time is highly reduced.

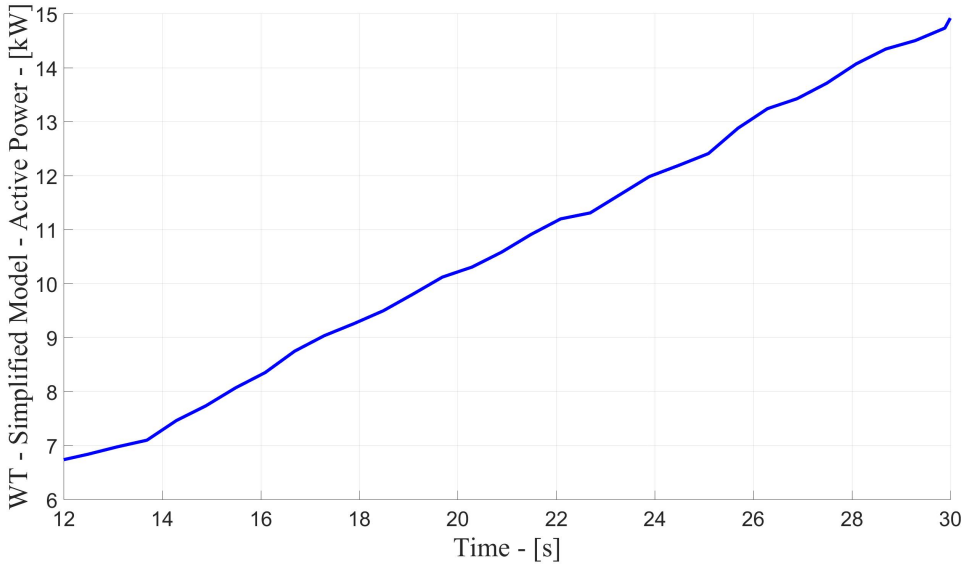

Figure 3.16: Wind turbine generator. Simplified model. Active power in kW.

3.3 PV system

With the same purpose of the wind turbine model, photovoltaic model is presented initially as a dynamic model. Then, it is reduced in a simplified model with a bidimensional dimensional look-up table.

3.3.1 Dynamic Model

In Figures 3.17 and 3.19 are shown the dynamic model proposed for the photovoltaic system and its Simulink model respectively. The inputs of the model are the solar irradiation in Wh/m^2 and the temperature in °C. The outputs are: (i) DC voltage in V, (ii) V_{ab} VSC in V, (iii) active power in kW, (iv) three phase voltages V_{abc} in V, and (v) three phase currents I_{abc} in A.

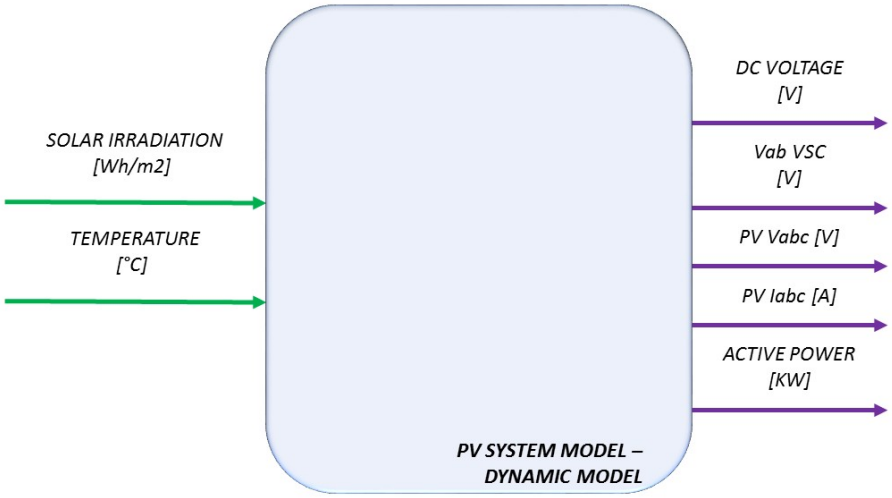

Figure 3.17: Photovoltaic model. Dynamic model.

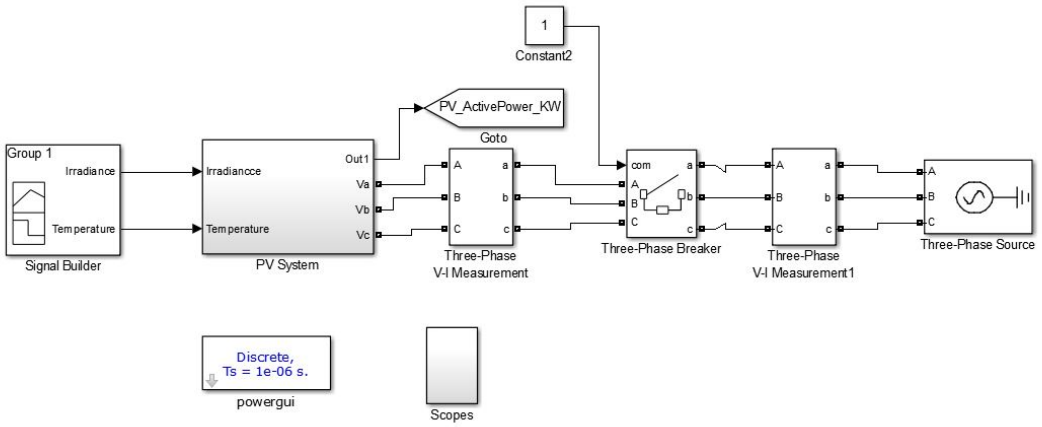

Figure 3.18: Photovoltaic system. Dynamic Simulink model.

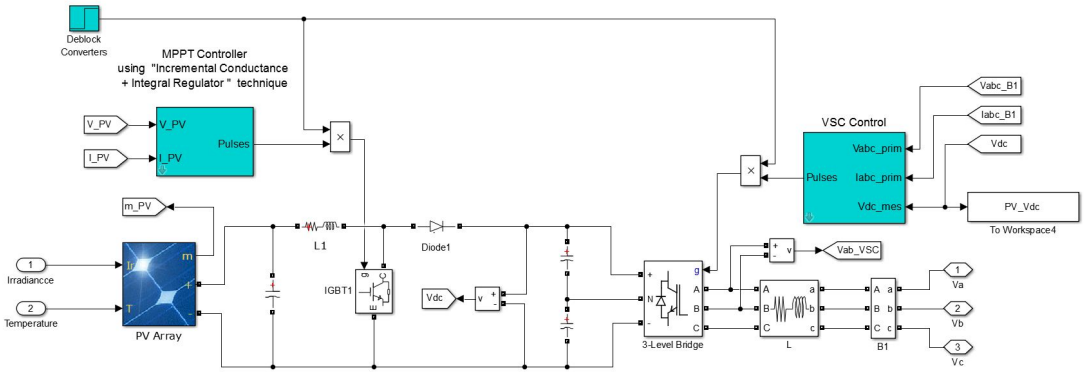

Figure 3.19: Photovoltaic system. Dynamic Simulink model.

The model is validated with a ramp of solar irradiation starting from 100 W/m^2 and coming to 1000 W/m^2 at a constant temperature of 25 °C. See Figure 3.20.

The responses of the model are presented in the following order: Figure 3.21 shows the three phase voltages V_{abc}, Figure 3.22 shows V_{ab} VSC, Figure 3.23 shows DC voltage and Figure 3.24 presents power produced by the PV system.

The three phase-to-phase voltage are 380 V and in the DC bus the voltage is constant at 625 V. The active power increases from 4 kW at 100 W/m^2 until 23 kW at 1000 kW.

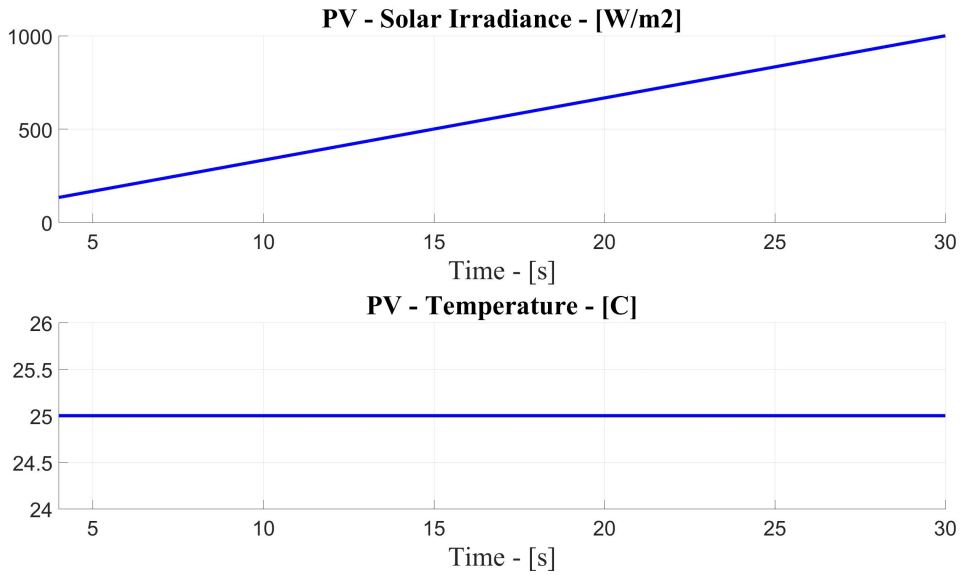

Figure 3.20: Photovoltaic system. Inputs. (a) Solar irradiation in W/m^2, (b) Temperature in °C.

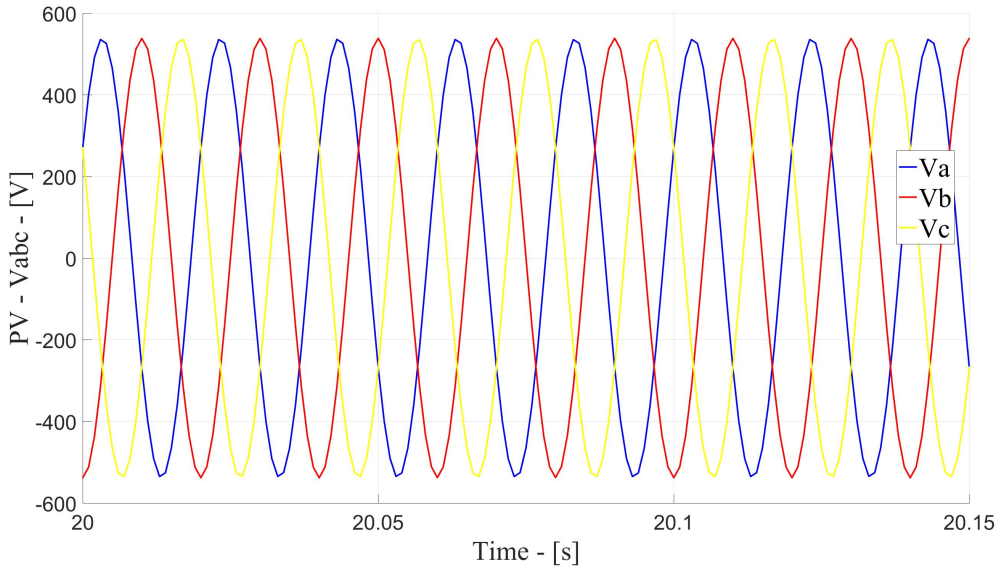

Figure 3.21: Photovoltaic system. Dynamic model. Three phase-to-phase voltages V_{abc} in A.

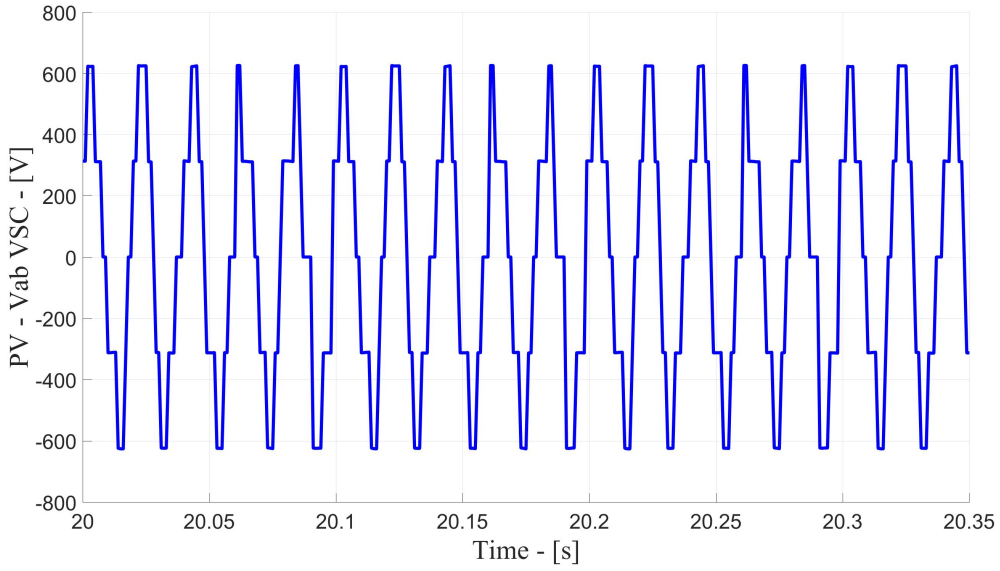

Figure 3.22: Photovoltaic system. Dynamic model. V_{ab} VSC in V.

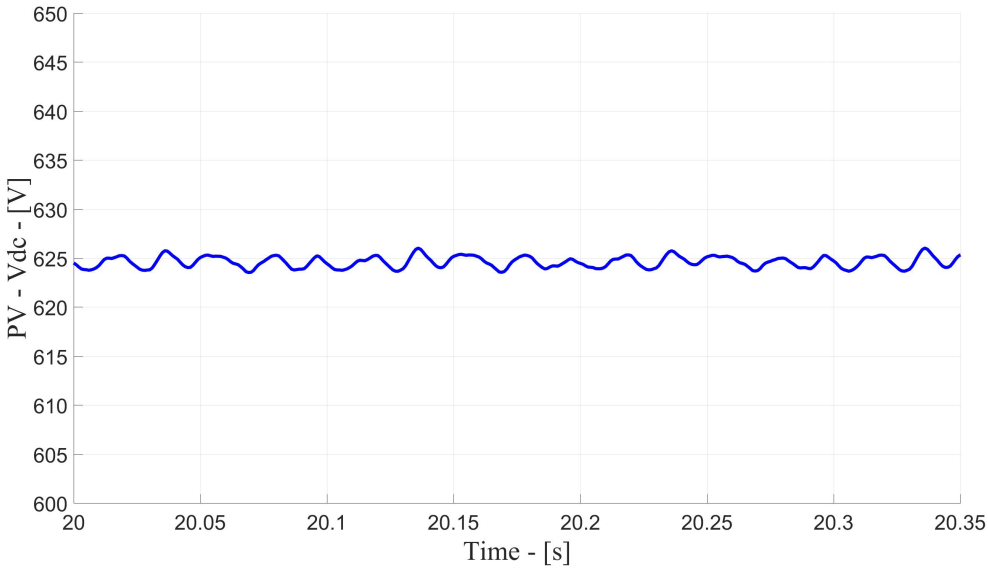

Figure 3.23: Photovoltaic system. Dynamic model. *DC* voltages V.

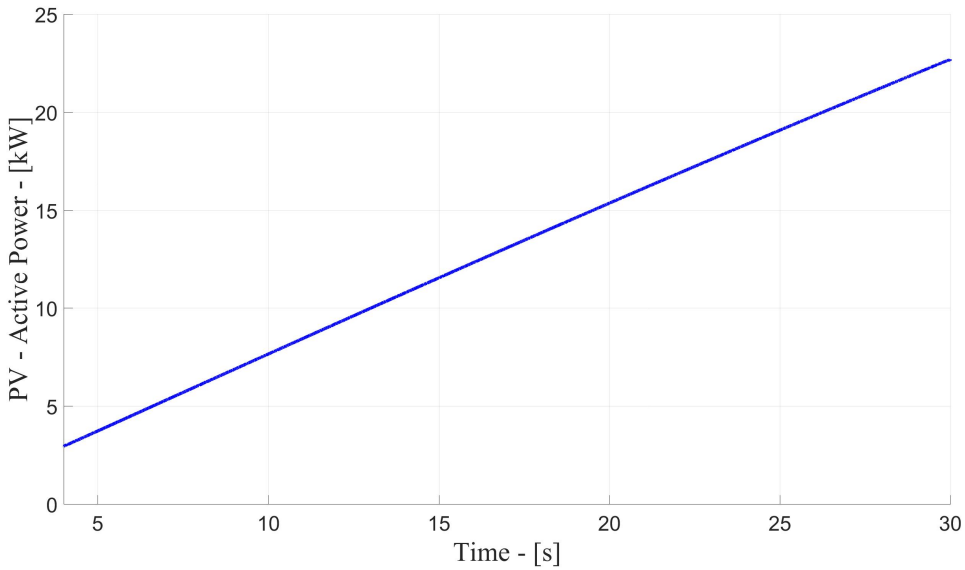

Figure 3.24: Photovoltaic system. Dynamic model. Active power in kW.

3.3.2 Simplified model

Figures 3.25 and 3.27 shown the simplified model and its Simulink model respectively. It inputs are: (*i*) Solar irradiation in Wh/m^2 and (*ii*) temperature in °C. The unique output is the power produced by the PV system in kW. The response of the model is presented in Figure 3.28.

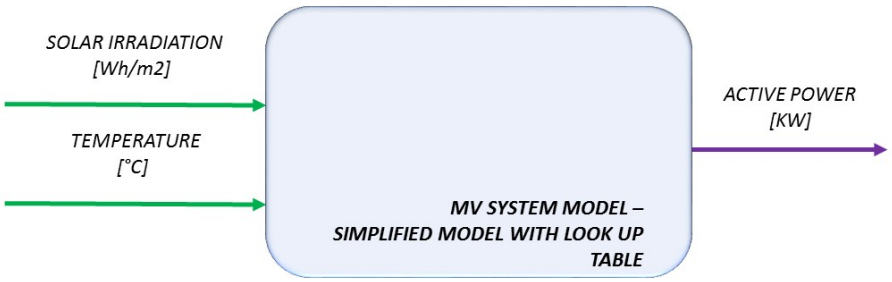

Figure 3.25: Photovoltaic system. Simplified model.

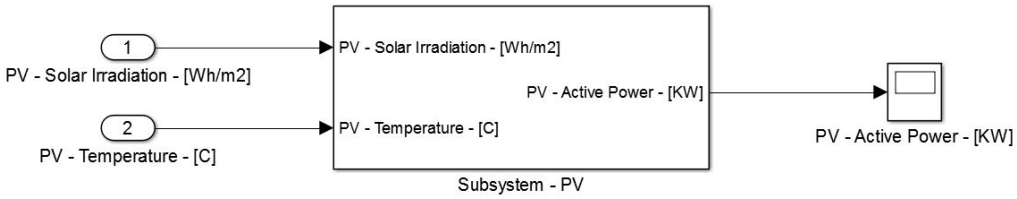

Figure 3.26: Photovoltaic system. Simplified Simulink model.

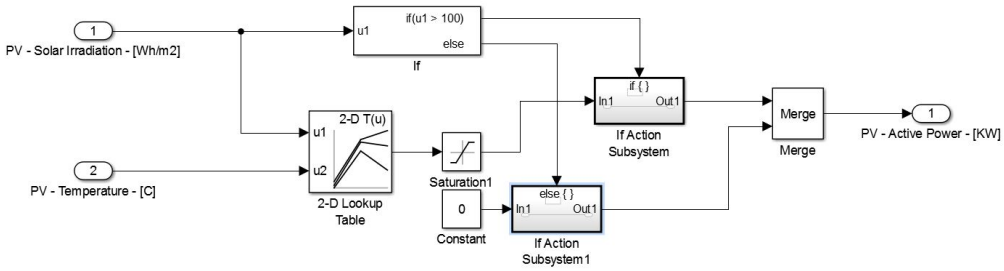

Figure 3.27: Photovoltaic system. Simplified Simulink model.

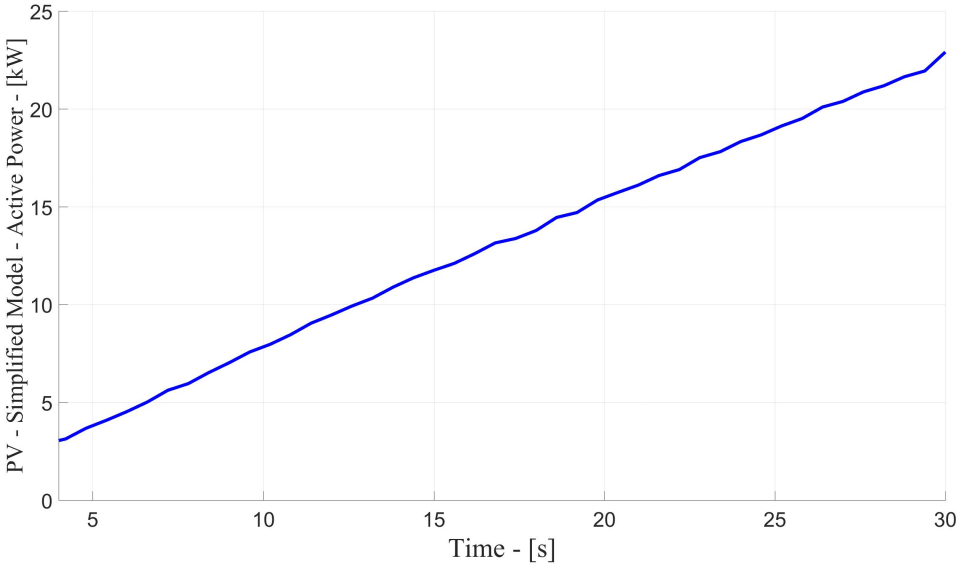

Figure 3.28: Photovoltaic system. Simulink model of simplified model with LU.

3.4 Alkaline Electrolyzer

Figures 3.29 and 3.32 present the dynamic model of the electrolyzer and its Simulink model respectively. The unique input of the dynamic model is the power requested in kW, while the outputs are: (*i*) temperature in °C, (*ii*) stack voltage in V, (*iii*) stack current in A, (*iv*) hydrogen produced in lpm and performance in %.

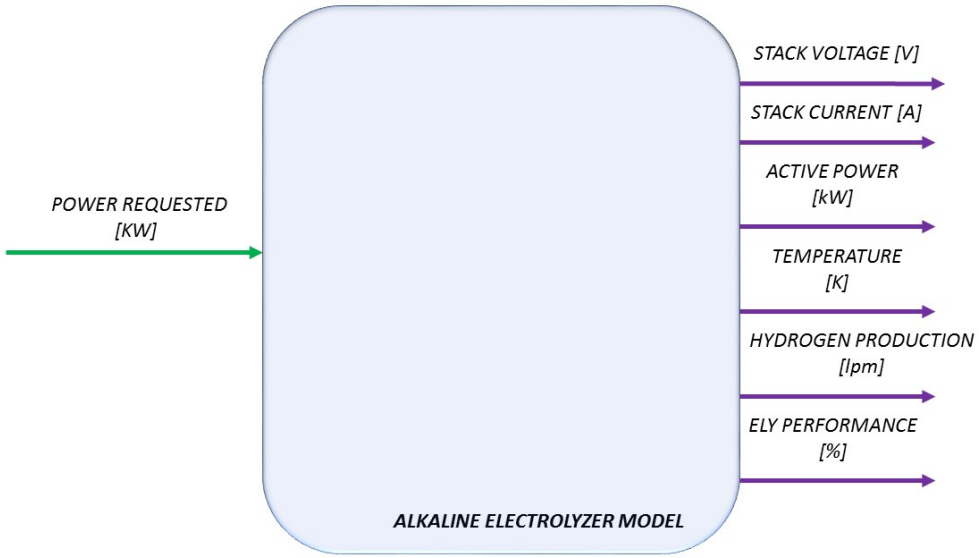

Figure 3.29: Alkaline electrolyzer. Proposed model

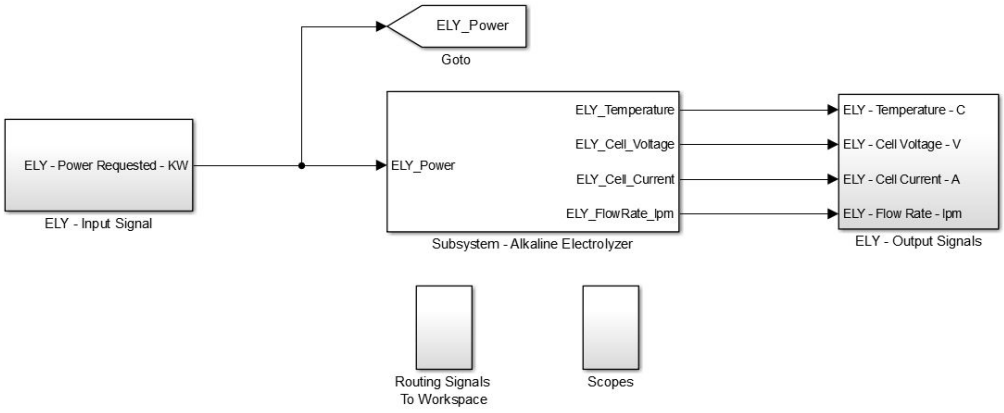

Figure 3.30: Alkaline electrolyzer. Simulink model.

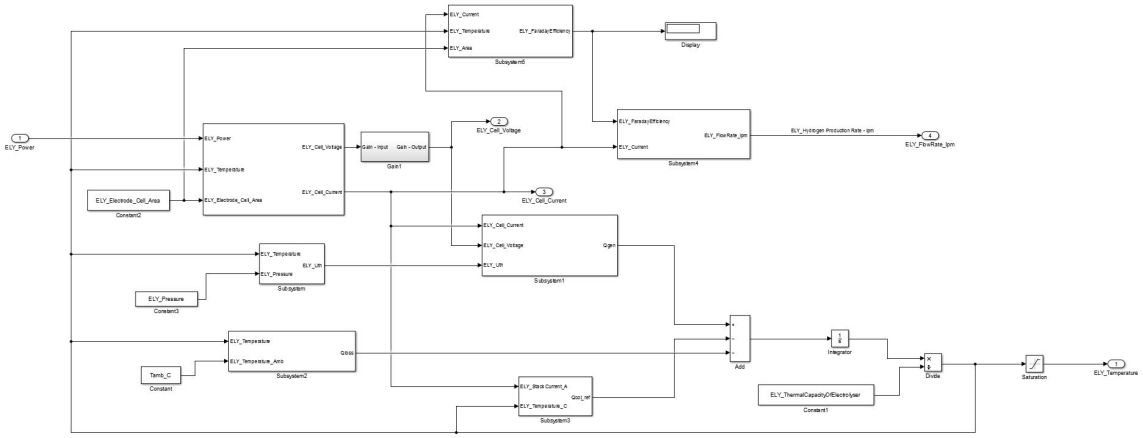

Figure 3.31: Alkaline electrolyzer. Simulink model.

The alkaline electrolyzer model is composed for a wide range of dynamics. It is composed by three submodels: (*i*) *electrical submodel*, (*ii*) *electrochemical submodel* and, (*iii*) *thermal submodel*. These dynamical models allow understand the complex interactions of all models when there are active at the same time. In Figure 3.32 is shown the structure of the model implemented for the alkaline eletrolyzer.

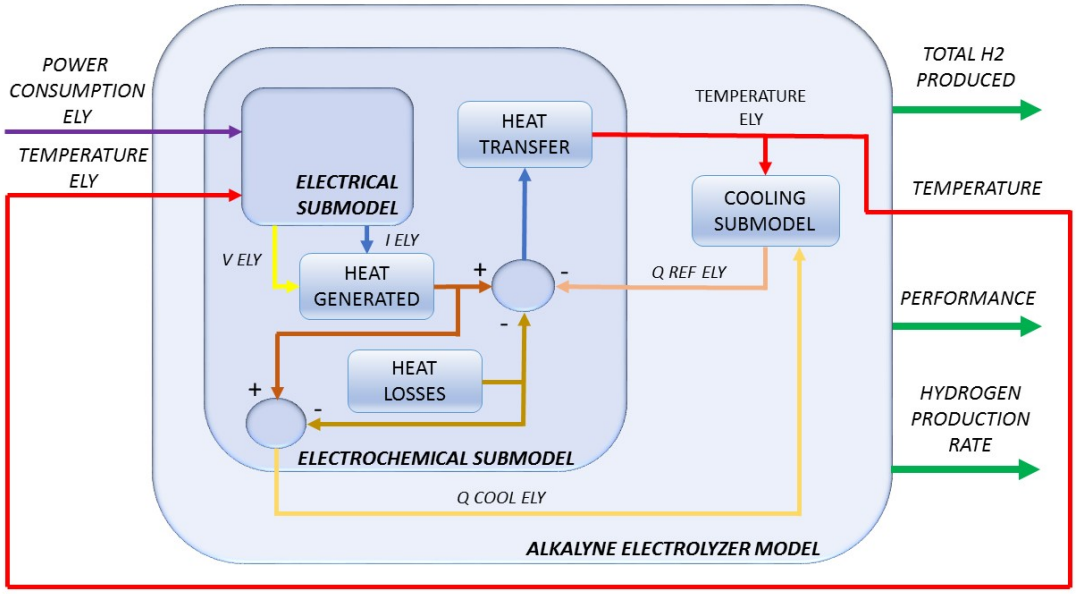

Figure 3.32: Alkaline electrolyzer. Structure of dynamic model.

The principal parameters of the dynamic model are shown in Table 3.1.

Table 3.1: Alkaline electrolyzer. Parameters of dynamic model.

Parameter	**Value**	**Unit**
s_0	1.586	V
s_1	1.378	V K^{-1}
s_2	-1.606	V K^{-2}
t_0	49.31	A m^{-2}
t_1	-0.3065	A m^2 K^{-1}
t_2	0.0004782	A m^2 K^{-2}
r_0	0.004747	Ω m^2
r_1	-1.367e-5	Ω m^2 K^{-1}
a_{conv}	3000	W A^{-1} K^{-1}
b_{cond}	600	W K^{-1}
C_{cw}	4184	J K^{-1}

The electrolyzer model is validated using data measured in a laboratory of a 8 kW alkaline electrolyzer. The input power is increased drastically from zero to around 8 kW with a step. Then, the electorlyzer is operated during 4 minutes. See Figure 3.33.

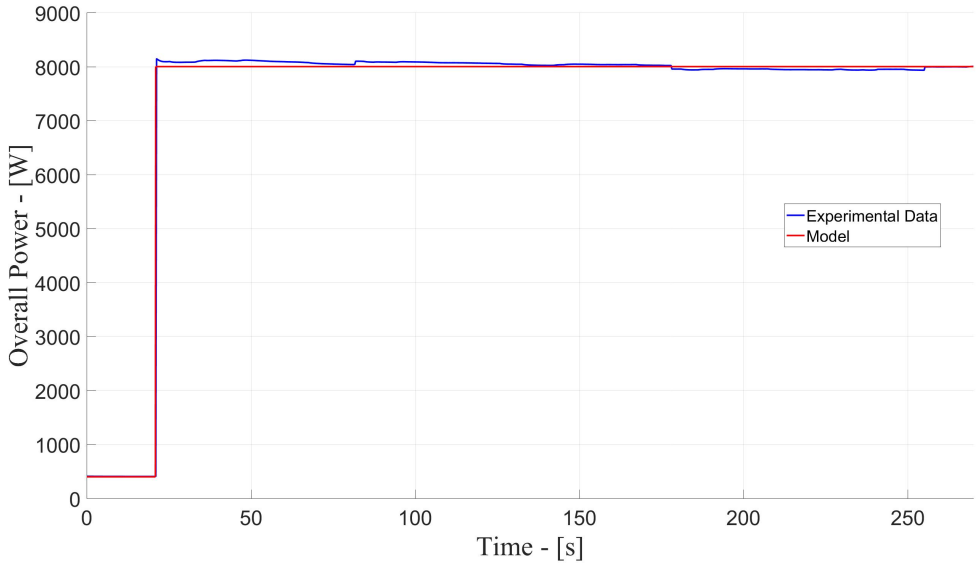

Figure 3.33: Alkaline electrolyzer validation. Active power in W.

In Figure 3.33 the active power corresponds to the overall power of the system. i.e. power requested by the electrolyzer and losses which are estimated as 400 W. The stack current and stack voltage of the validating model steadies at 145 A and 45 V with errors of 9.15 % and 2.5 % respectively. The temperature reaches its steady state to 31 °C after 200 s with an error of 2.13 % and, hydrogen production steadies at 19.91 lpm with an error of 1.89 %. See Figures 3.34, 3.35, 3.35 and 3.37 respectively.

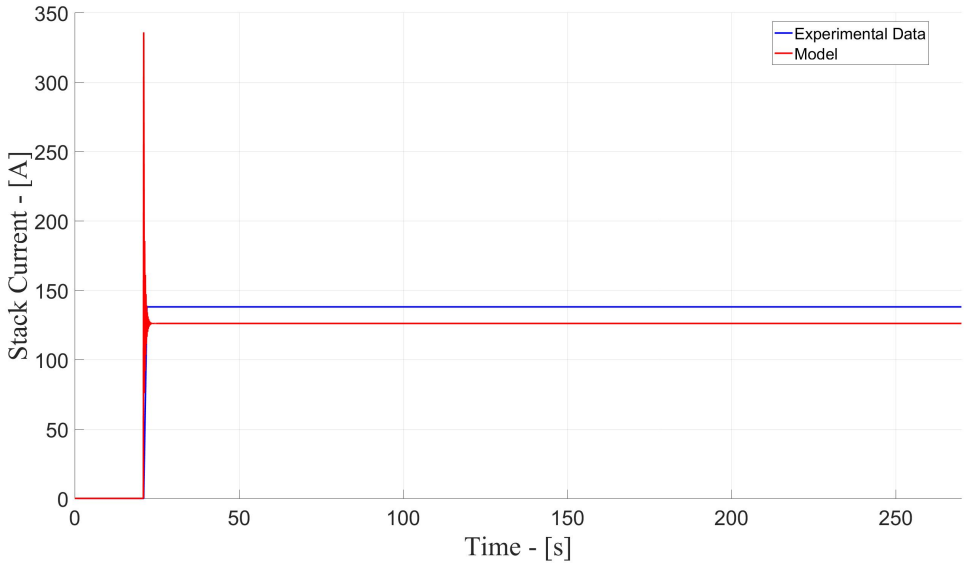

Figure 3.34: Alkaline electrolyzer validation. Stack current in A. Maximum error at steady state of 9.15 %.

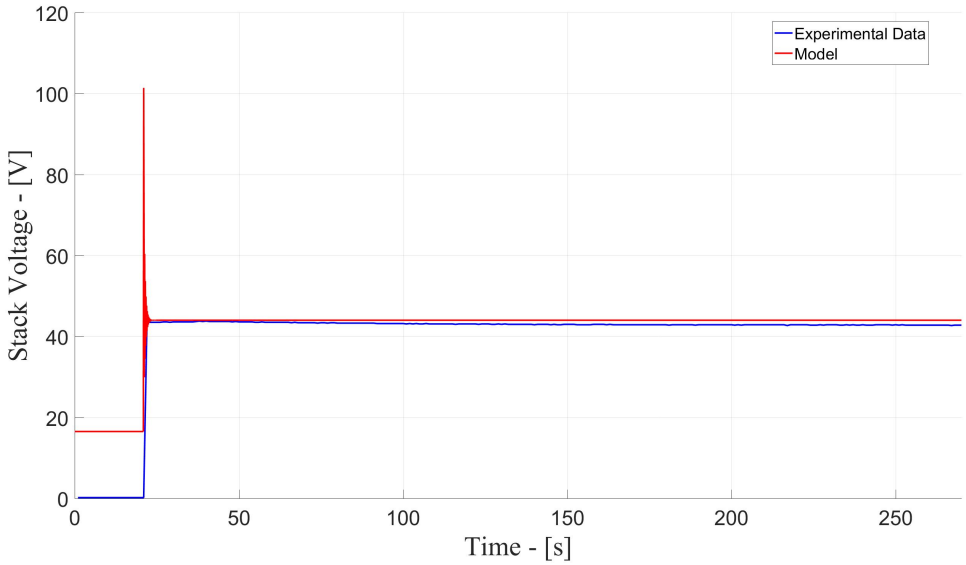

Figure 3.35: Alkaline electrolyzer validation. Stack voltage in V. Maximum error at steady state of 2.5 %.

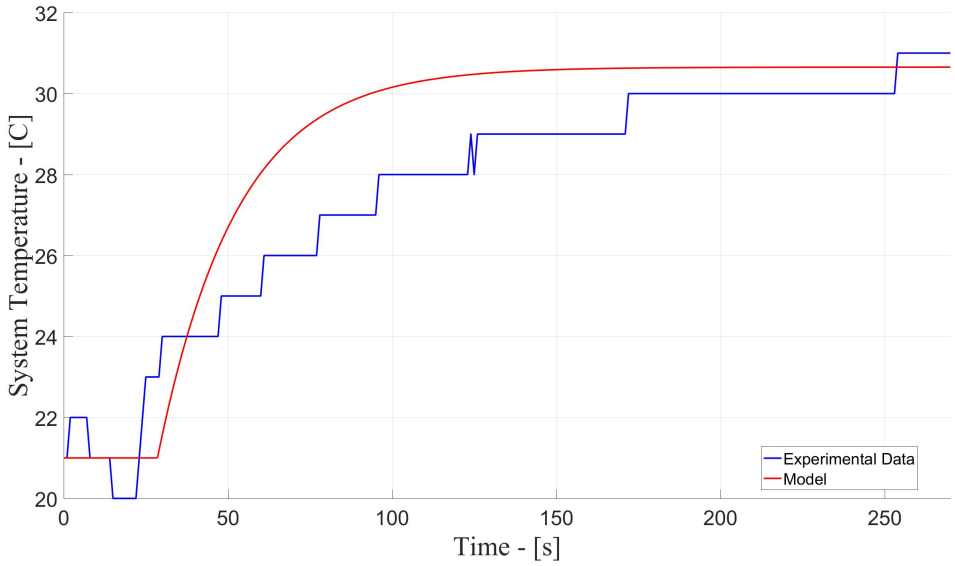

Figure 3.36: Alkaline electrolyzer validation. Stack temperature in °C. Maximum error at steady state of 2.13 %.

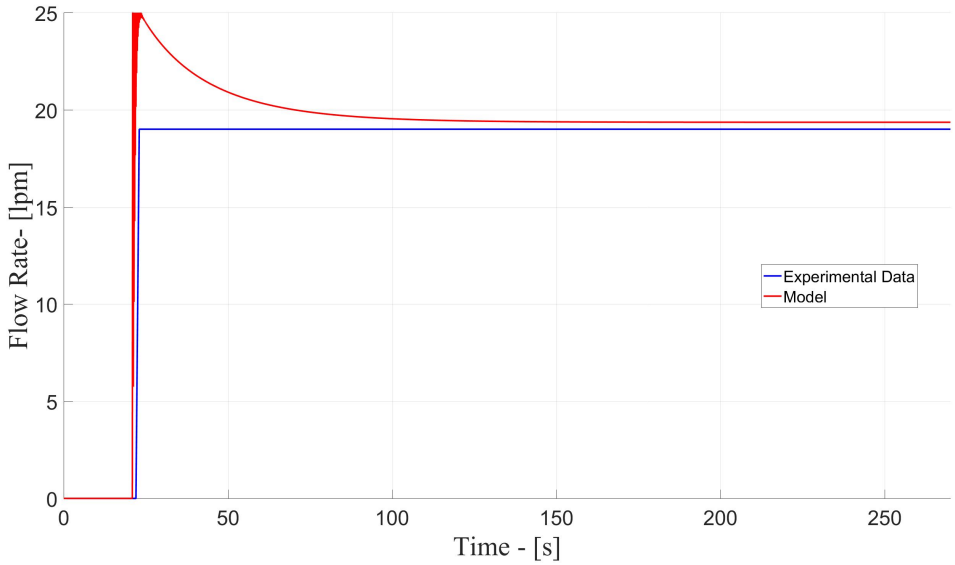

Figure 3.37: Alkaline electrolyzer validation. Flow rate in lpm. Maximum error at steady state of 1.89 %.

The characteristic curve of the electrolyzer at 35 °C is presented in Figure 3.38. The open circuit voltage of the cell is 1.229 V while at 50 A the cell voltage is equals to 4.5 V.

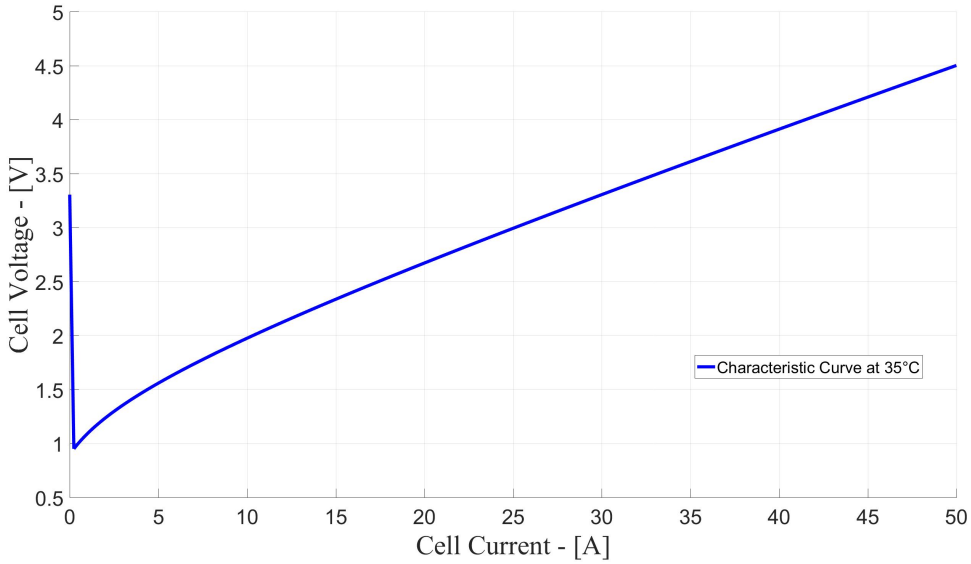

Figure 3.38: Alkaline electrolyzer. *I-U* characteristic curve at 35 °C.

The results demonstrate the accuracy of the model in predicting the dynamic behaviour of the electrolyzer: stack voltage and current, temperature variations and hydrogen production.

3.5 PEM Fuel Cell

The dynamic model of the *PEM* fuel system and its Simulink model are shown in Figures 3.39 and 3.41 respectively. The inputs of the Simulink model are: the hydrogen requested in lpm and the stack current in A, while the outputs are: (*i*) power produced in kW, (*ii*) stack voltage in V, (*iii*) stack current in A and, (*iv*) hydrogen consumption in lpm.

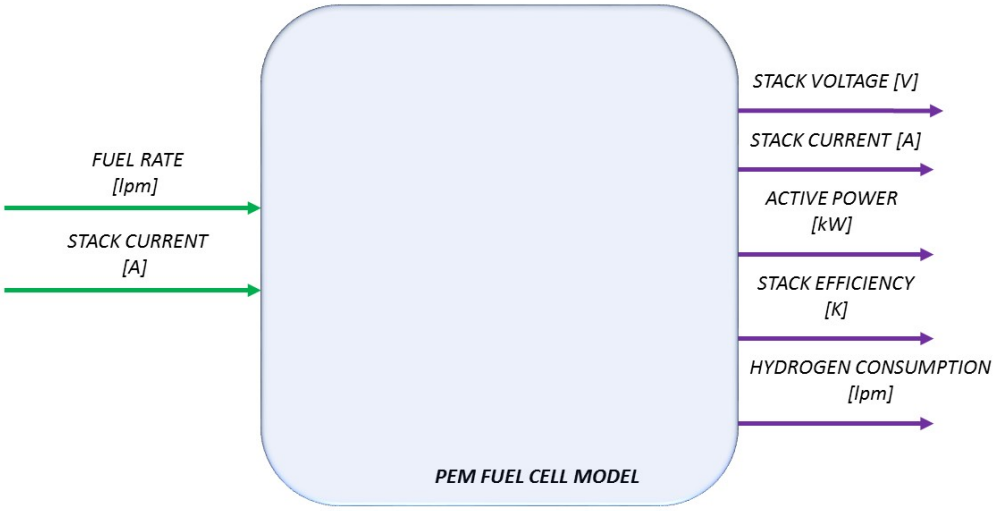

Figure 3.39: *PEM* fuel cell model. Proposed model

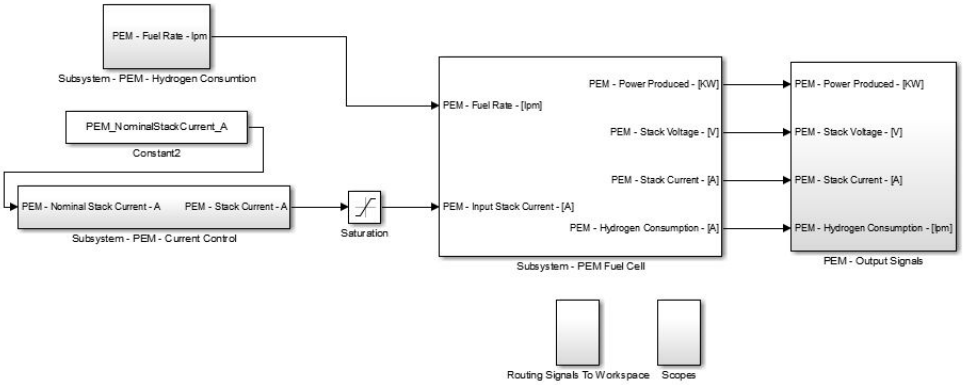

Figure 3.40: *PEM* fuel cell. Simulink model.

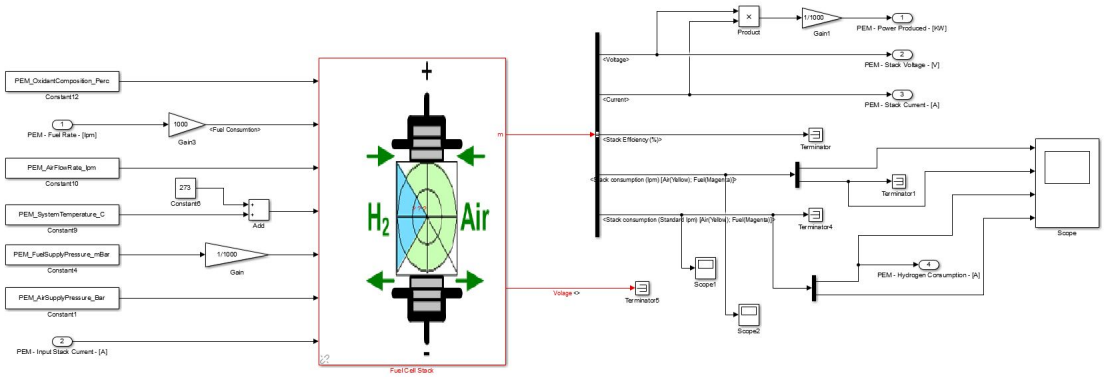

Figure 3.41: *PEM* fuel cell. Simulink model.

The dynamic model is composed by three submoodels: (*i*) *Thermal submodel* which calculates the temperature, (*ii*) *Electrochemical submodel* which calculates the cell voltage and, (*iii*) *hydrogen consumption submodel* which calculates the consumption rate. The structure of the dynamic model is shown in Figure 3.42.

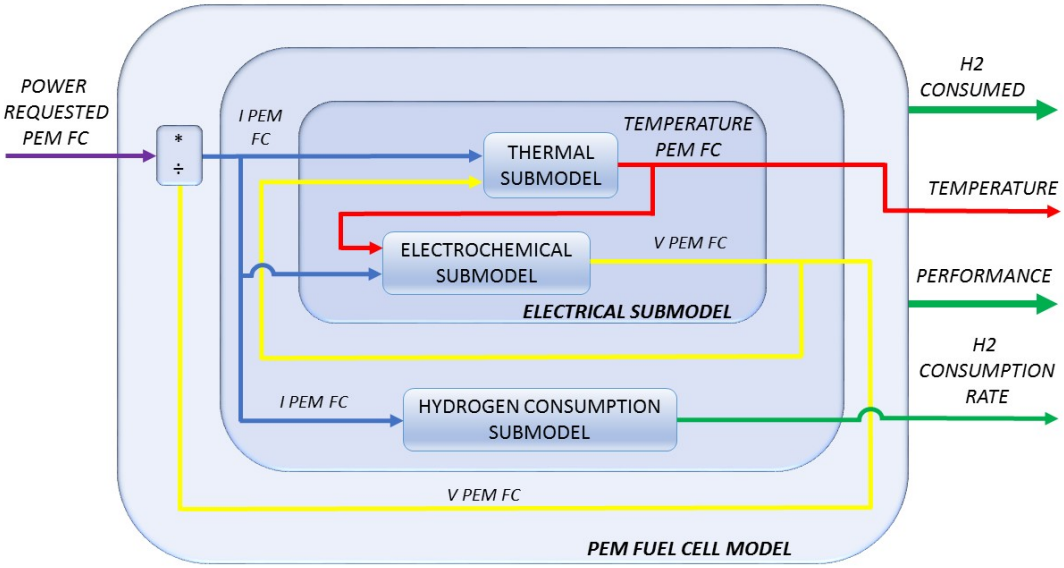

Figure 3.42: Structure of dynamic *PEM* fuel cell model.

The validation of the model is performed from measured data in a laboratory of a *PEM* fuel cell 12 kW stack composed by 110 cells. Measured data correspond to the following conditions:

1. 40 % of oxidant composition (O_2).
2. Air pressure at 1 bar.
3. Variable load.

The data used to validate the model are presented in Figure 3.43. It is observed: that H_2 increases from 100 to 200 lpm, whereas temperature oscillates between 50 to 65 °C. Air flow rate and fuel pressure are almost constant at 200 lpm and 225 mbar respectively.

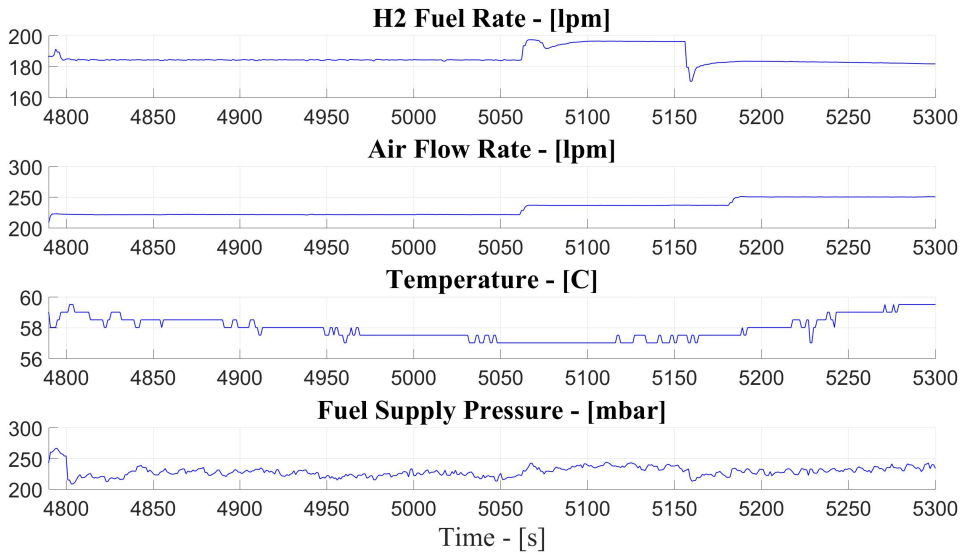

Figure 3.43: *PEM* fuel cell. Validation at 40 % of oxidant composition (O_2) and 1 bar of air pressure. H_2 and air fuel rate in lpm, temperature in °C and, fuel pressure in mbar.

The stack current, stack voltage and active power produced are shown in Figures 3.44, 3.45 and, 3.46 respectively. The maximum error obtained on the current is 7.5 %, on the voltage is 3.3 % and on the power is 5.9%.

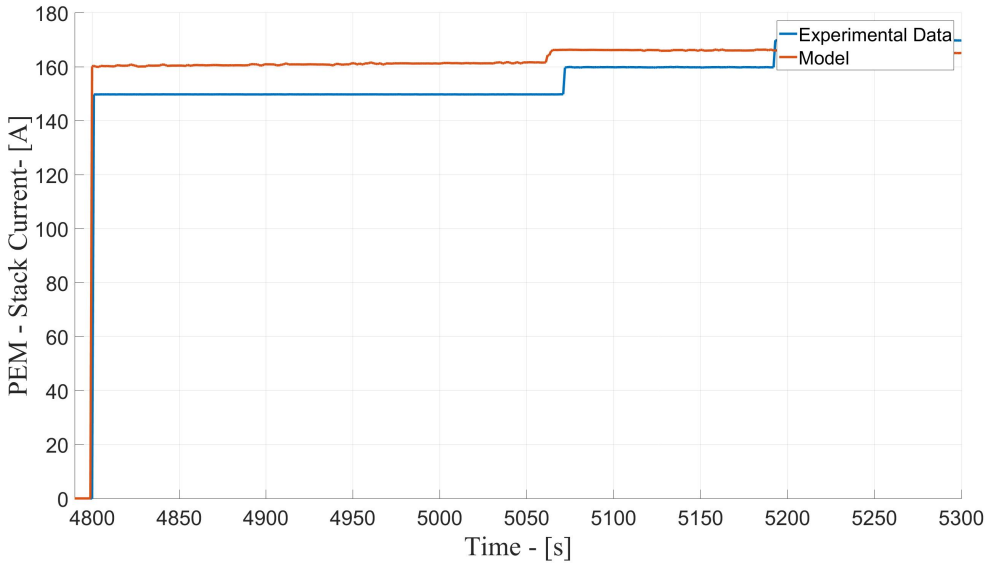

Figure 3.44: *PEM* fuel cell validation. Current in A. Maximum error of 7.5 %.

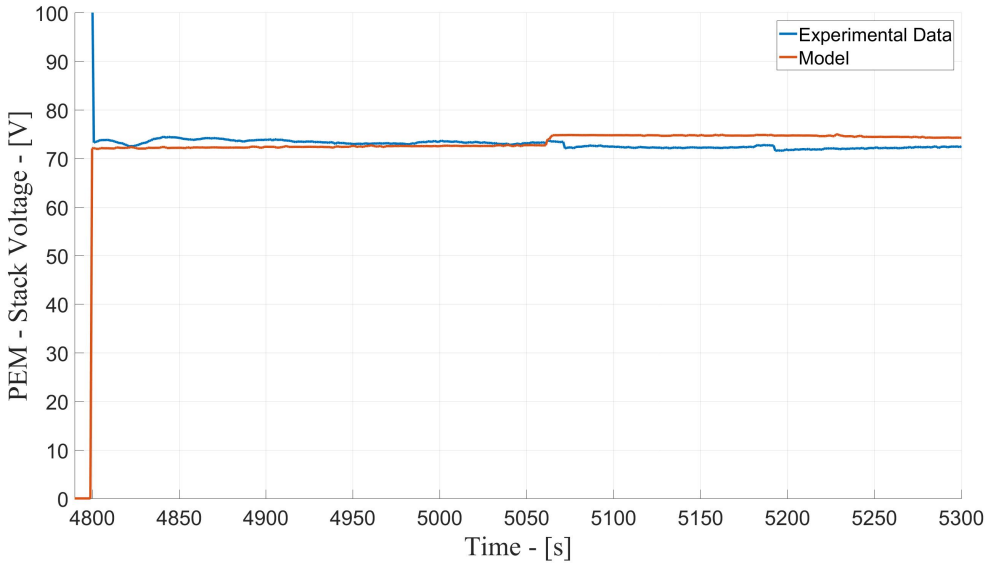

Figure 3.45: *PEM* fuel cell validation. Voltage in V. Maximum error of 3.3 %.

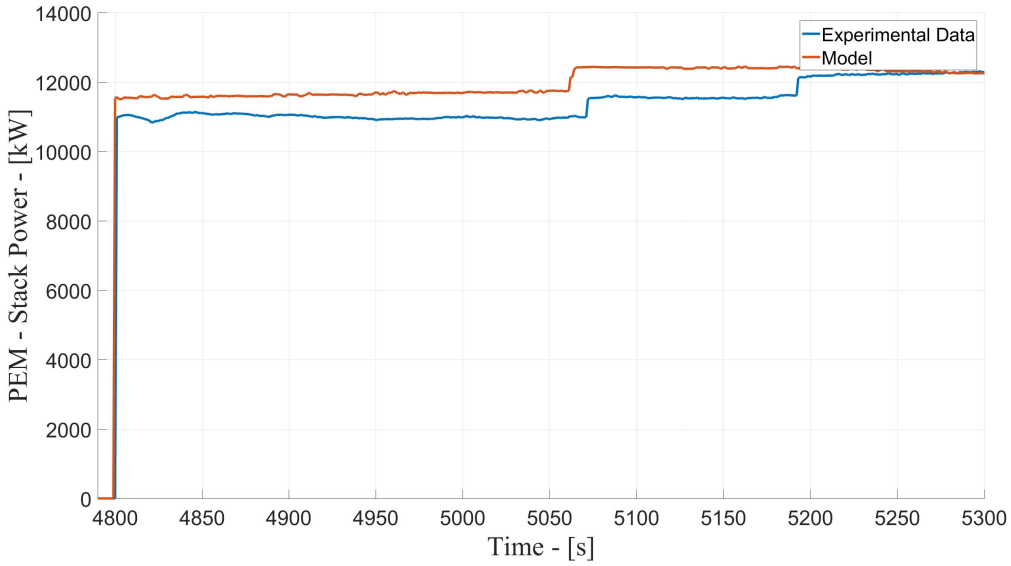

Figure 3.46: *PEM* fuel cell validation. Active power in W. Maximum error of 5.9 %.

3.6 Hydrogen Storage Tank

The general model for the hydrogen storage tank is presented in Figure 3.47. The inputs of the model are the hydrogen production by the electrolyzer in lpm and the hydrogen consumption by the *PEM* fuel cell in lpm. The output is the tank level expressed in %, Nm^3, kg or m^2.

Figure 3.47: Hydrogen storage tank model.

The general model is written in Simulink. Unlike the general model, Simulink model has four inputs. These are: (*i*) hydrogen production by electrolyzer, (*ii*) hydrogen consumption by *PEM* fuel cell, (*iii*) enable signal to charging tank and, (*iv*) enable signal to discharging tank. The unique output of the model is the tank level in %, see Figure 3.49.

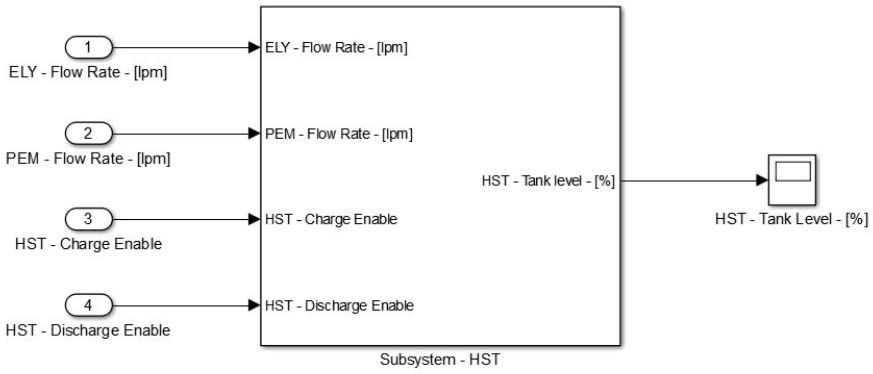

Figure 3.48: Hydrogen storage tank model.

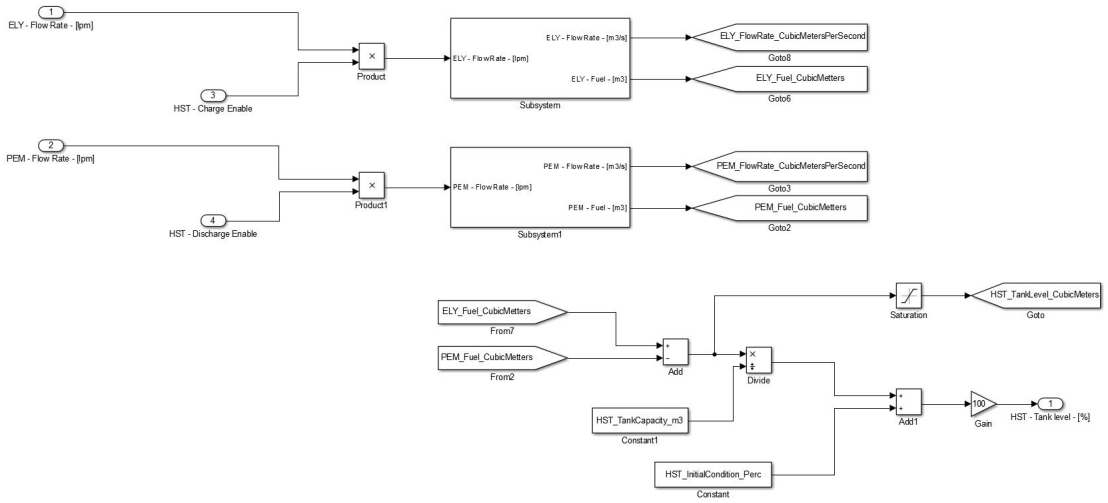

Figure 3.49: Hydrogen storage tank model.

The hydrogen tank has a capacity of 9 m^3. The simulink model is validated with a constant flow rate of 20 lpm . It is required supplying 7.5 h with a constant inlet flow of 20 lpm of hydrogen to charge the tank from its minimum capacity (0 m^3) until its maximum capacity (9 m^3) (See Figure 3.50).

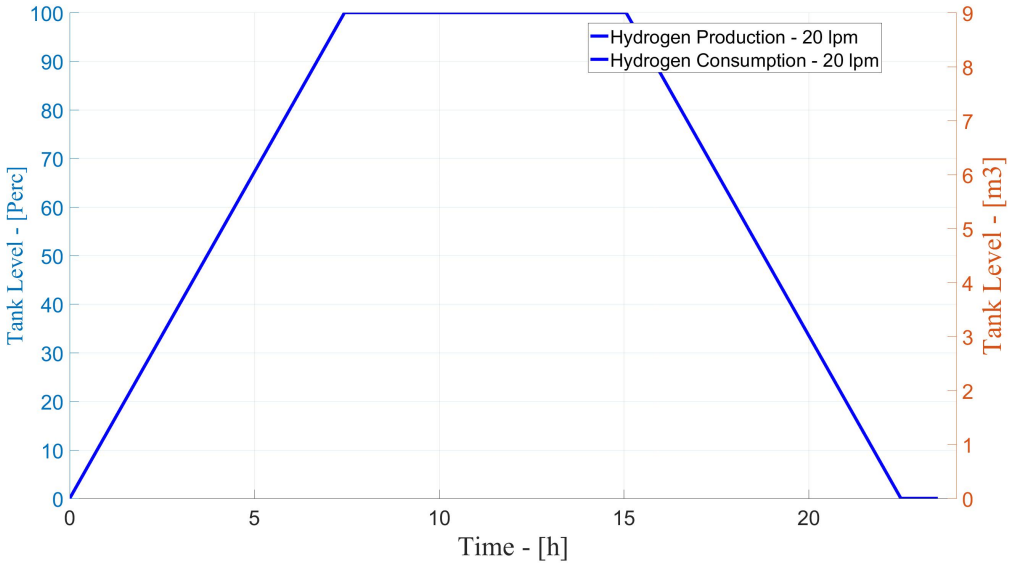

Figure 3.50: Hydrogen storage tank model. Charging - discharging hydrogen tank with a constant flow rate of 20 lpm.

Chapter 4

Control Strategy

4.1 Central Control System

In this chapter is proposed a strategy of control for the $H\mu G$ and its Simulink model. This block receives the state variables as inputs and computes the control signals as outputs. In the next section are presented one by one the conditions to enable/disable the single models. Furthermore, The control signals are described. To complete the calculations of the integrated system without incurring in algebraic loops, variable initial values must be set into the central control system *CCS*. The sections are organized in the following order.

1. Section (4.1.1) - Central control system.
2. Section (4.1.2) - WT system.
3. Section (4.1.3) - PV system.
4. Section (4.1.4) - Alkaline electrolyzer.
5. Section (4.1.5) - PEM fuel cell.
6. Section (4.1.6) - Hydrogen storage tank.

The supervisory control of the CCS is presented in Figure 4.1.

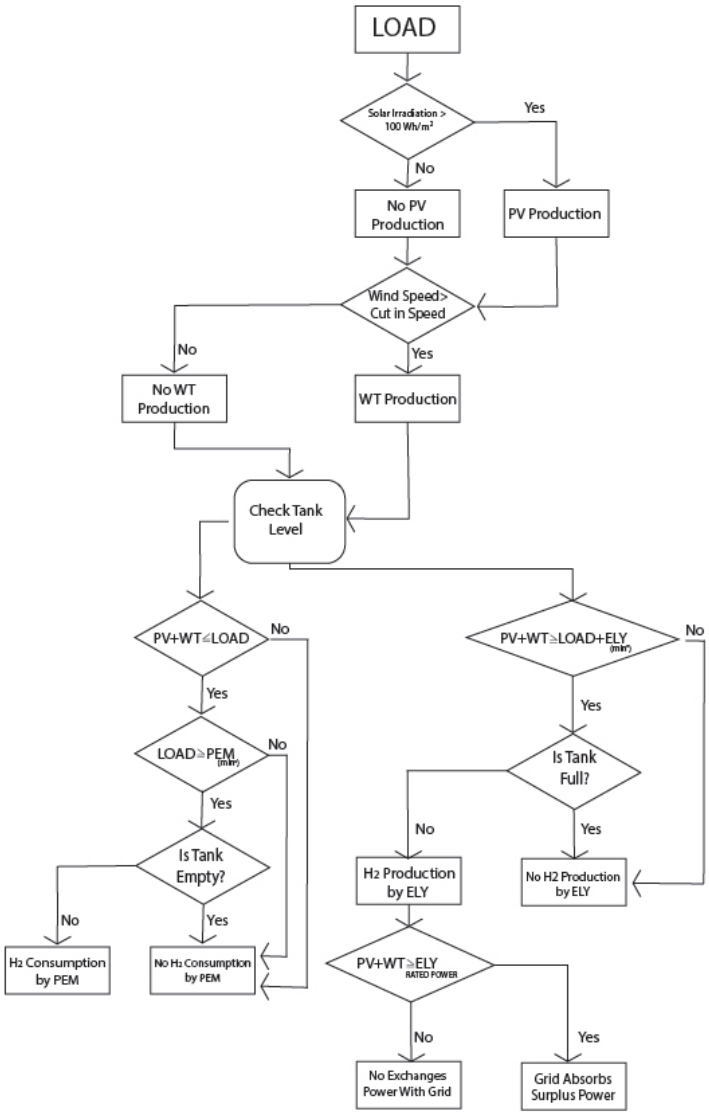

Figure 4.1: Central control system. Flow chart of model proposed.

In Sections 4.1.2 to 4.1.6 can be note the enable signals which allow the connection and disconnection of the models (simulation of switcher breaks).

4.1.1 Central Control System

In the *CCS* all individual models are combined, exchanging the state variables through the integrated structure. Figures 4.2 and 4.3 show inputs and outputs of the *CCS* system

model and the implementation in Simulink respectively. Inputs and outputs are summarized as below.

Inputs

1. PV System - Active power in kW.
2. PV System - Active solar irradiation in Wh/m^2.
3. WT System - Active power in kW.
4. WT System - Wind speed in kW.
5. Load - Power demand in kW.
6. PEM fuel cell - Power produced in kW.
7. Alkaline electrolyzer - Power requested in kW.
8. Hydrogen storage tank - Tank level in %.

Outputs

1. Enable signal to PV system.
2. Enable signal to WT system
3. Enable signal to alkaline electrolyzer.
4. Enable signal to PEM fuel cell.
5. Enable signal to charging system of hydrogen tank.
6. Enable signal to discharging system of hydrogen tank.

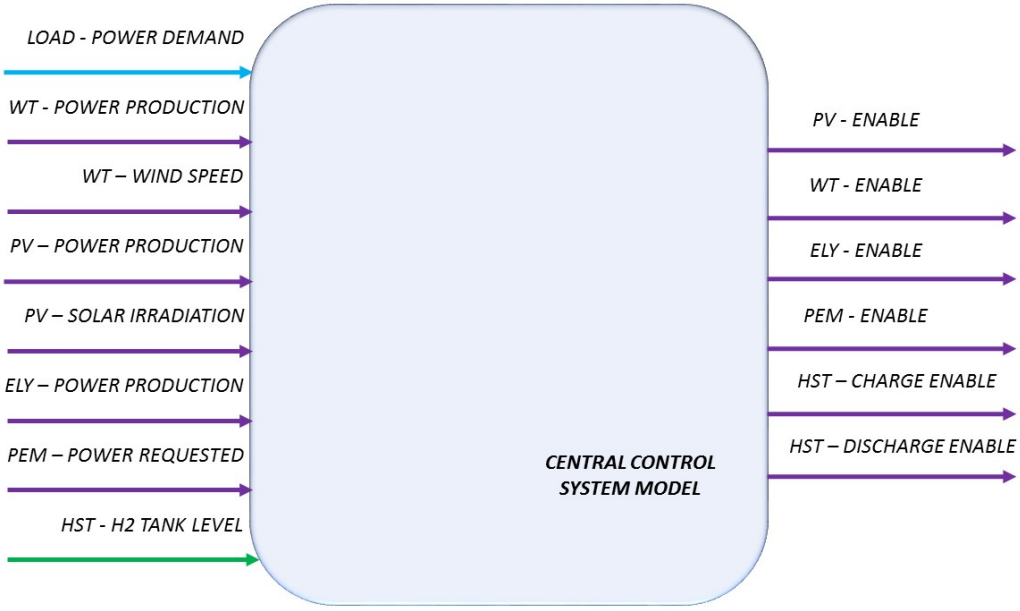

Figure 4.2: Central control system. Model proposed.

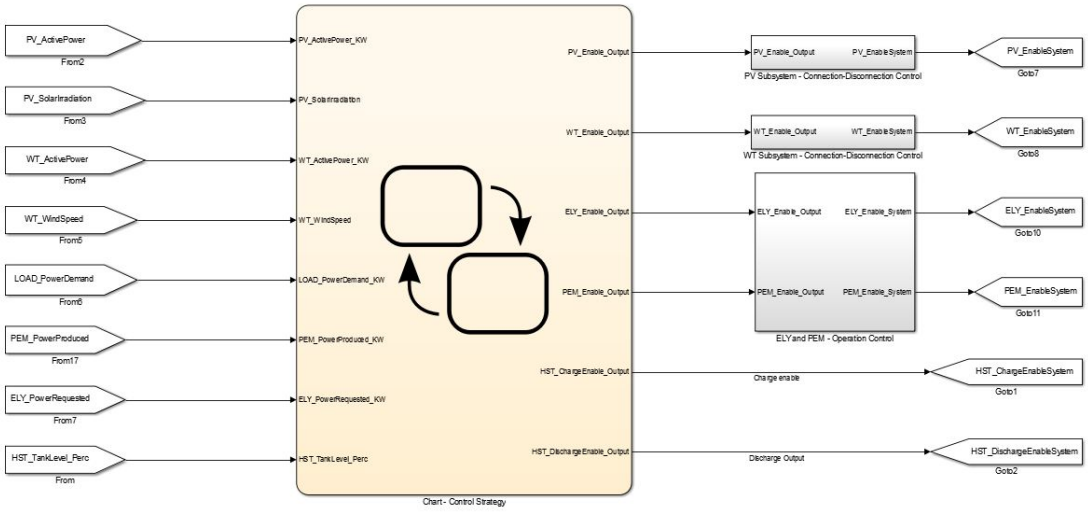

Figure 4.3: Central control system. Simulink Model.

In Simulink, the *CCS* is coupled with two additional subsystems: (*i*) *Connection-Disconnection control subsystem* and, (*ii*) *ELY and PEM - Operation control subsystem*, see Figures 4.4 and 4.5 respectively. The first subsystem filters the connection and dis-

connection of the systems under rapid fluctuations of the weather conditions. i.e. short periods without wind or cloudy. The second subsystem avoids the simultaneous operation of the electrolyzer and *PEM* fuel cell systems. When the electrolyzer is turned *on* the *PEM* fuel cell is blocked instantaneously during all the operation of the electrolyzer, and in the same way, when the *PEM* fuel cell is turned *on*, electrolyzer is blocked (turned *off*).

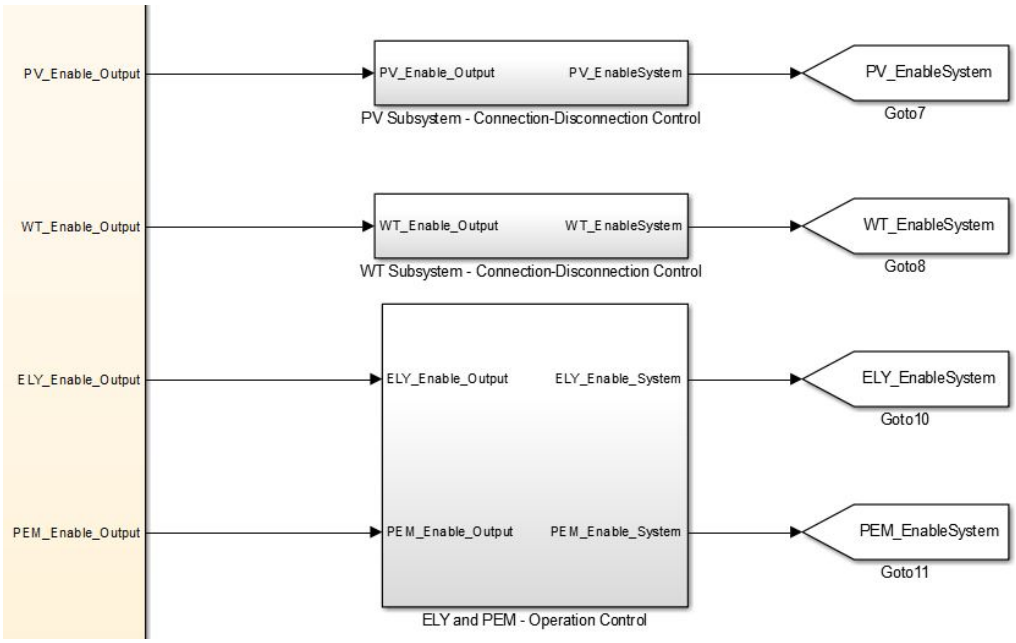

Figure 4.4: Central control system. Connection-Disconnection control.

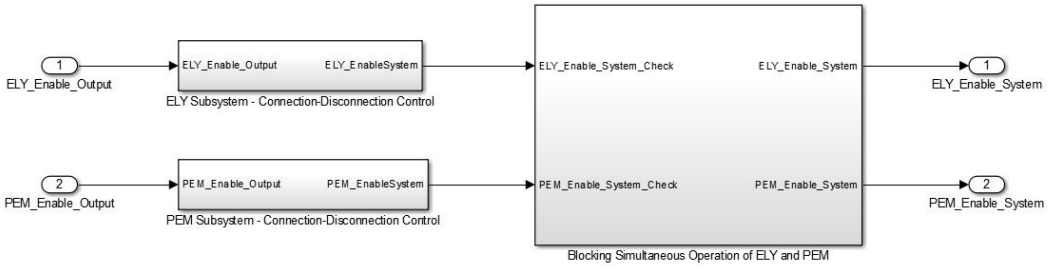

Figure 4.5: Central control system. *ELY* and *PEM* - Operation control subsystem.

4.1.2 Wind Turbine System

The simplified model of the wind system is activated according to the wind conditions. It is connected to the grid at the *PCC* when the wind speed is higher than 5 m/s and lower than 30 m/s, over a period of time of 500 s. Then, in this interval of wind speeds the *WT* may exchange active power to the grid or supply the alkaline electrolyzer. The model is disconnected commanding the enable signal. It switches to 0 the output, i.e. the active power, see Figure 4.6.

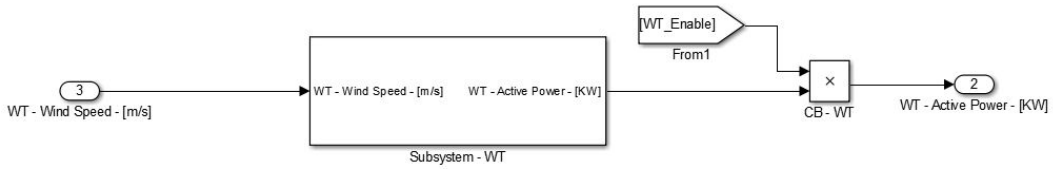

Figure 4.6: Simplified model of wind turbine system. Simulink Model.

4.1.3 Photovoltaic System

Analog to the wind turbine model, the photovoltaic model is enabled when the solar irradiation is higher than 100 Wh/m^2 over 500 s. In the same manner it may exchange active power either with the local demand or the electrolyzer. To disconnect the system the output is switched to 0 through the enable signal. See Figure 4.7.

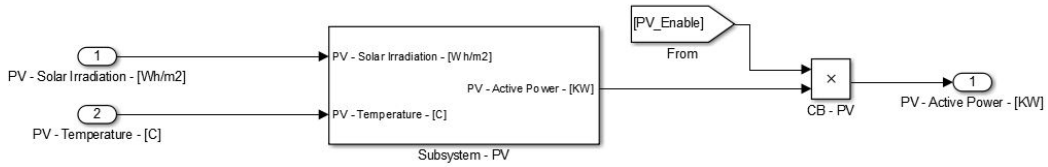

Figure 4.7: Simplified model of photovoltaic system. Simulink Model.

4.1.4 Alkaline Electrolyser

Electrolyzer is switched *On* when the following conditions are satisfied: (i) the sum of the power produced by the wind turbine P_{WT} and photovoltaic system P_{PV} are higher than the power demanded P_{Load} and the minimum operating power of the electrolyzer $P_{ELY}^{(min)}$, over

an average of 500 s. (*ii*) the level of charge of the hydrogen tank is between its minimum and maximum capacity. Conditions (4.1) and (4.2) shows the primary conditions to turn *On* the electrolyzer.

$$P_{PV} + P_{WT} >= P_{Load} + P_{ELY}^{(min)} \tag{4.1}$$

$$HST_{Level}^{(min)} < HST_{Level} < HST_{Level}^{(max)} \tag{4.2}$$

Once satisfied both of these conditions the electrolyzer is switched *on* and in a safe condition the *PEM* fuel cell is automatically blocked (switched *off*). To turn *off* the electrolyzer the primary conditions are expressed by conditions (4.3) (over a period of time higher than 500 s), (4.4) and (4.5).

$$P_{PV} + P_{WT} < P_{Load} + P_{ELY}^{(min^*)} \tag{4.3}$$

$$HST_{Level} > HST_{Level}^{(max)} \tag{4.4}$$

$$HST_{Level} < HST_{Level}^{(min)} \tag{4.5}$$

Being $P_{ELY}^{(min)}$ and $P_{ELY}^{(min^*)}$ the 20 % and 15 % of the rated power of the electrolyzer respectively. In Figure 4.8 is presented the simulink model. It is disconnected switching to 0 the input of the model, i.e, power requested by the electrolyzer.

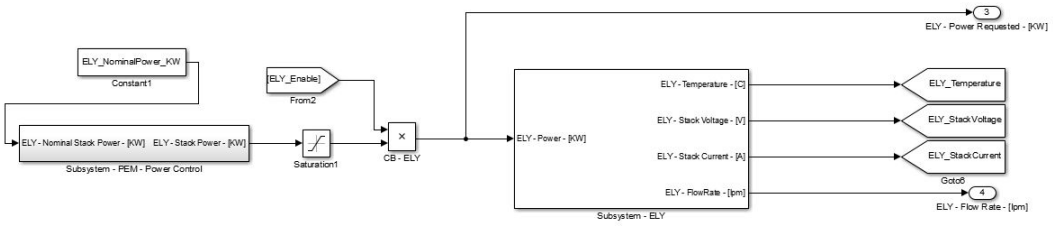

Figure 4.8: Alkaline electrolyzer. Simulink Model

4.1.5 PEM Fuel Cell

The primary conditions to switch *On* the *PEM* fuel cell are: (*i*) the tank level is as condition (4.2), (*ii*) the sum of P_{WT} and P_{PV} is lower than P_{Load}, over an average of 500 s. (*iii*) demand to satisfy is higher than the minimum operating power of the PEM fuel cell $P_{PEM}^{(min^*)}$. See conditions (4.6) and (4.7) respectively.

$$P_{PV} + P_{WT} < P_{Load} \tag{4.6}$$

$$P_{PEM}^{(min)} < P_{Load} \tag{4.7}$$

In the same way of the electrolyzer, when the *PEM* fuel cell is switched *on* the electrolyzer is automatically blocked (turned *off*). To turn *off* the electrolyzer: (*i*) tank level of hydrogen is out of its minimum or maximum value as conditions (4.4) and (4.5), (*ii*) the sum of P_{WT} and P_{PV} is higher than P_{Load}, over an average of 500 s. (*ii*) demand to satisfy is lower than the minimum operating power of the *PEM* fuel cell $P_{PEM}^{(min)}$. Conditions (4.8) and (4.9) respectively.

$$P_{PV} + P_{WT} > P_{Load} \tag{4.8}$$

$$P_{PEM}^{(min^*)} > P_{Load} \tag{4.9}$$

The enable signal is shown in Figure 4.9.

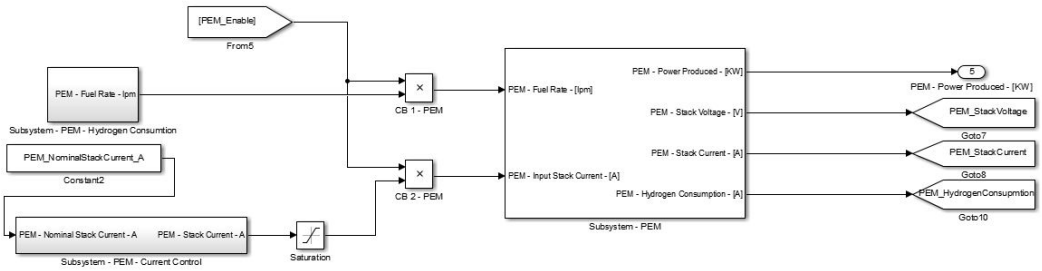

Figure 4.9: *PEM* fuel system. Simulink Model.

The values of $P_{PEM}^{(min)}$ and $P_{PEM}^{(min^*)}$ are choosen as the 20 % and 15 % of the rated power of the *PEM* fuel cell respectively. In Figure 4.9 is presented the Simulink model. It is disconnected switching to 0 the inputs of the model, i.e, fuel rate of hydrogen consumption and stack current of the *PEM* fuel cell.

4.1.6 Hydrogen Storage Tank

The hydrogen storage tank may operate between the 10 % and 95 % of its capacity. As mentioned before, it is controlled by the state of charge of the electrolyzer and the *PEM* fuel cell. When the state of charge of the tank reaches its maximum capacity and the electrolyzer is producing hydrogen (electrolyzer *on*), electrolyzer is turned *off*. While in the case of the *PEM* fuel cell, when it is producing power i.e. consuming hydrogen (*PEM* fuel cell *on*) and the tank level decreases until its minimum capacity, the *PEM* fuel cell is turned *off*.

The tank model has two enable signals. The first one allows to active the charging system of the tank, while the second one actives the discharging system. See Figure 4.10.

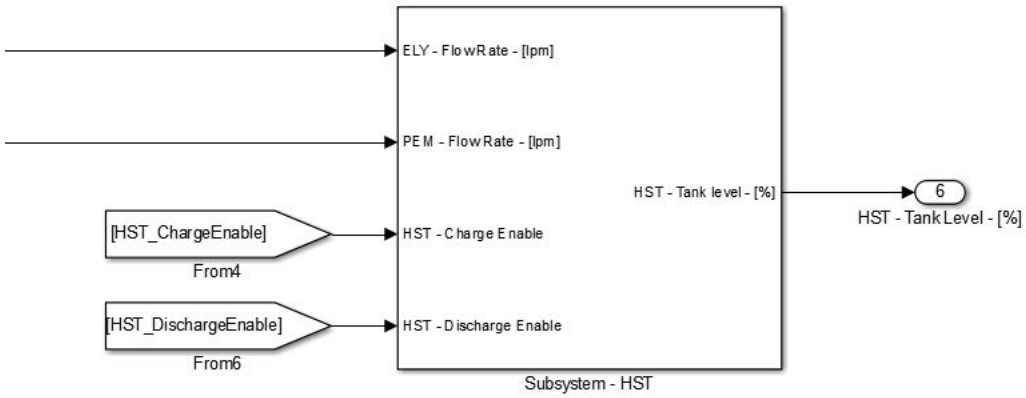

Figure 4.10: Hydrogen storage tank. Simulink Model.

Chapter 5

Simulation Description and Results

5.1 Introduction

The main goal of this chapter is to simulate the operation of the $H\mu G$ as much as possible close to the reality. The main focus is the description of the integration of the models in order to perform a global system simulation. The outline of the chapter is the following one:

1. Global model: Integration of single models to the central control system (CCS).
2. Testing global model: Validation with load profile.
3. Analyzing validation load profile under different scenarios.
4. Case of study 1 (realistic case): Variable load profile.
5. Case of study 2 (realistic case): Static load profile.
6. Analyzing performance of the global model.

5.2 Integration of Models to CCS

The global model of the $H\mu G$ and its Simulink scheme are presented in Figures 5.1 and 5.2. As we can see, the model is composed by eight submodels. The CCS receives information simultaneously from six subsystems as shown in Figure 5.1: (i) wind turbine, (ii) photovoltaic, (iii) load, (iv) grid, (v) hydrogen tank and (vi) fuel cell. At the same time, CCS commands the electrolyzer subsystem.

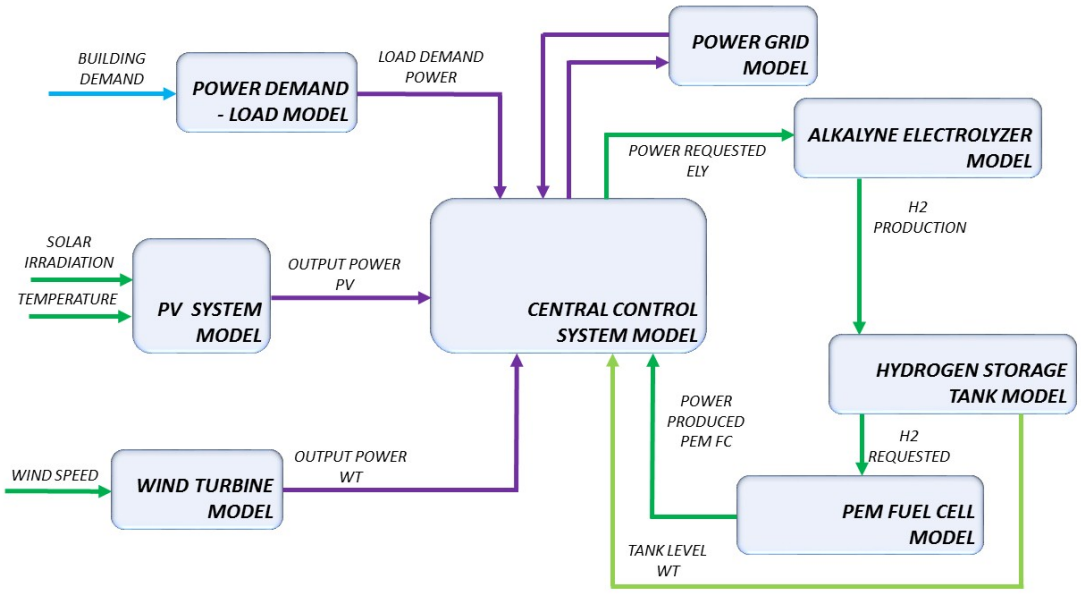

Figure 5.1: Global model. Integration of single models to central control system.

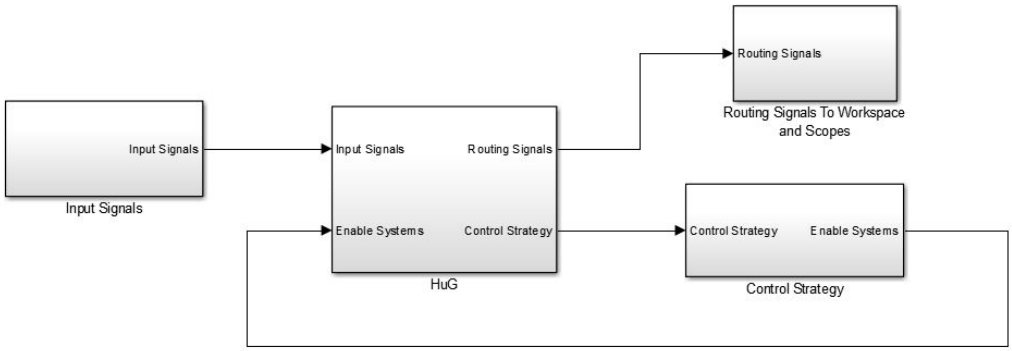

Figure 5.2: Global model. Simulink model

The Simulink model shown in Figure 5.2 is composed basically by four sub systems: (*i*) input signals block which groups all the signals intended like inputs of the $H\mu G$, i.e *RES* and demand curve, (*ii*) $H\mu G$ submodel which includes the integration of all subsystems composing the hydrogen system (*PEM* fuel cell, hydrogen storage tank and alkaline

electrolyzer), (*iii*) control strategy subsystem which commands the whole hydrogen system and (*iv*) routing signals block to sent data to the scopes or Matlab-workspace.

Once the hydrogen system is integrated with the microgrid, the *RES* sources are connected to the medium voltage level utility grid at the point of common coupling (*PCC*). In this point, the power balance is figured out like the difference between all the loads (demand curve and electrolyzer) and all the power produced (*RES* and *PEM* full cell). In Figure 5.3 is shown the power balance scheme in Simulink, which can be described mathematically by Eq. (5.1).

$$P_{GRID} = P_{LOAD} - P_{GEN} = P_{LOAD} - P_{PV} - P_{WT} + P_{ELY} - P_{PEM} \tag{5.1}$$

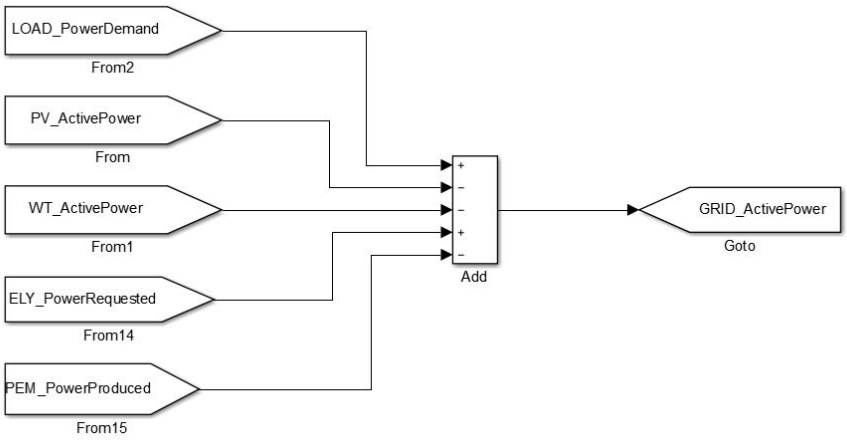

Figure 5.3: Power exchange at the point of common coupling (*PCC*).

In Eq. (5.1) $P_{GRID} > 0$ when $P_{LOAD} > P_{GEN}$, whereas $P_{GRID} < 0$, the sources of power generation are: (*i*) *PV* system, (*ii*) *WT* system and, (*iii*) *PEM* fuel cell. The loads, instead, are positive: (*iv*) power demanded and (*v*) alkaline electrolyzer. In Eq. (5.1) some considerations can be done:

1. $P_{GRID} = 0$: Absolute equilibrium between the load demand, the power produced by the *RES* and the contribution of the hydrogen system.
2. $P_{GRID} > 0$: Independently of the contribution of the hydrogen system and the *RES*, the grid is necessary for meeting the demand.

3. $P_{GRID} < 0$: The $H\mu G$ is injecting power into the grid.

Figure 5.4 presents the scheme in Simulink of the $H\mu G$. On the top-left of the figure, there is the load and two distributed power generations: PV and WT subsystems. On the right and on the bottom are positioned the alkaline electrolyzer and the PEM fuel systems, respectively. These are connected to the hydrogen storage tank which is positioned on the bottom-right. All the power signals are routing to the subsystem Grid - Power exchange positioned on the middle of the top-right and presented previously in Figure 5.3.

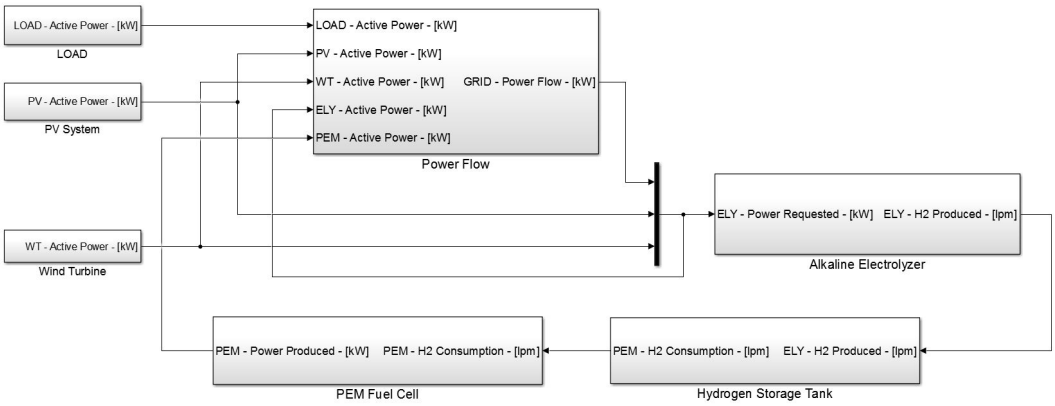

Figure 5.4: Global model. $H\mu G$ subsystem.

5.3 Testing Global Model

In this section the global model is tested by using a test profile. Once the integrated model has been completed, its performance is assessed by means of representative simulations. The simulations are performed under variable wind speed and solar irradiation conditions with a validation load profile considering different scenarios, in order to demonstrate the operation of the whole hydrogen system, i.e. (*i*) alkaline electrolizer, (*ii*) *PEM* fuel cell and (*iii*) hydrogen storage tank. The scenarios selected for the assessment are summarized below:

Scenario 1: Extremely favorable wind condition.
Scenario 2: Extremely favorable solar irradiation condition.
Scenario 3: Both favorable wind and solar irradiation condition.

Scenario 4: Scarce wind speed.
Scenario 5: Scarce solar irradiation.
Scenario 6: Both scarce wind and solar conditions.

The expected operation of the components is a leading role for the alkaline electrolyzer in **Scenarios 1, 2 and 3**. In contrast, in **Scenarios 4 and 5**, it is expected an intermittent operation of the electrolyzer. For the *PEM* fuel cell, it is not probable to be activated in **Scenarios 1 to 5**, while in **Scenario 6** its operation should be predominant.

Subsections 5.3.1 to 5.3.6 outline the simulations performed under a validation load profile. The solar irradiation and temperature of the *PV* system and the the wind speed of the *WT* system data have been created randomly, and then, they were processed to select six types of representative scenarios.

5.3.1 Validation load profile

The validation hourly load profile is one input of the *CCS*. It is presented in Figure 5.5. This profile is a characteristic case of a residential load which is composed by 2 peaks during a period of 24 h, i.e, 20 kW at 8 h and 18 kW at 17 h. The energy demand during the day is 12.35 kWh and the time stamp of the validation profile is 40 min.

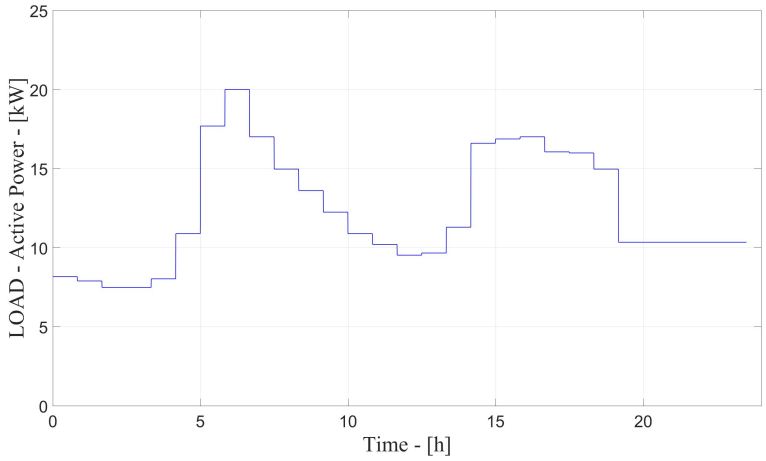

Figure 5.5: Validation load profile. Active power in kW.

5.3.2 Photovoltaic system

Hourly data of solar irradiation on the horizontal plane and temperature getting from a previous in the laboratory are presented as inputs of the PV system, see Figure 5.6. As mentioned before, the unique output of the simplified PV system is the active power produced as shown in Figure 5.7. The energy produced during the day is 5.37 kWh and the profiles of solar irradiation and temperature have been chosen strategically in order to have with the photovoltaic system an energy production about the 50% of the demand curve.

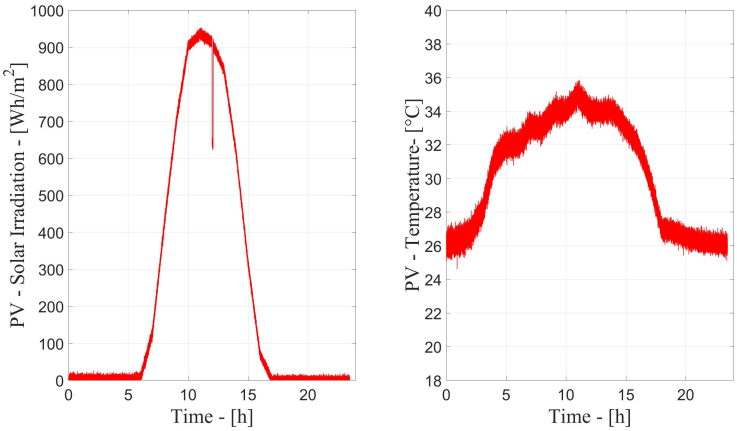

Figure 5.6: Inputs of photovoltaic system. (a) Solar irradiation in Wh/m^2 and (b) Temperature in °C.

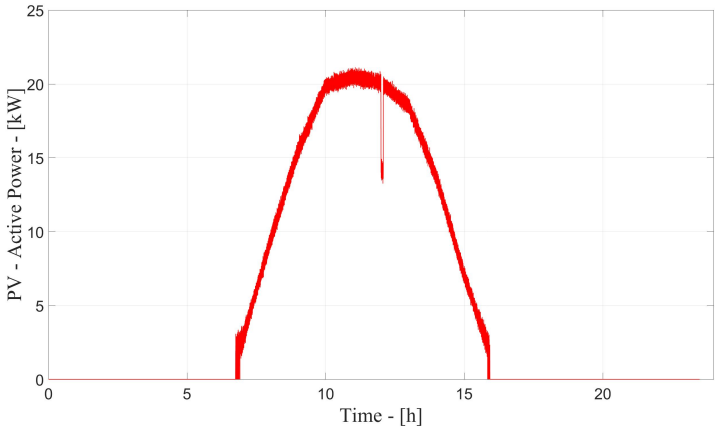

Figure 5.7: Output of photovoltaic system. Active power in kW.

5.3.3 Wind turbine system

The wind turbine model has one input (wind speed) and one output (active power produced). The profile of the wind speed has been build from experimental data obtained in a previous work in the laboratory. It is almost constant over the rated speed of the wind turbine. In the same way that the photovoltaic system, the wind turbine system produces 5.38 kWh contributing with the another 50% of the demand curve. The input and the output of the wind turbine model are presented in Figures 5.8 and 5.9, respectively.

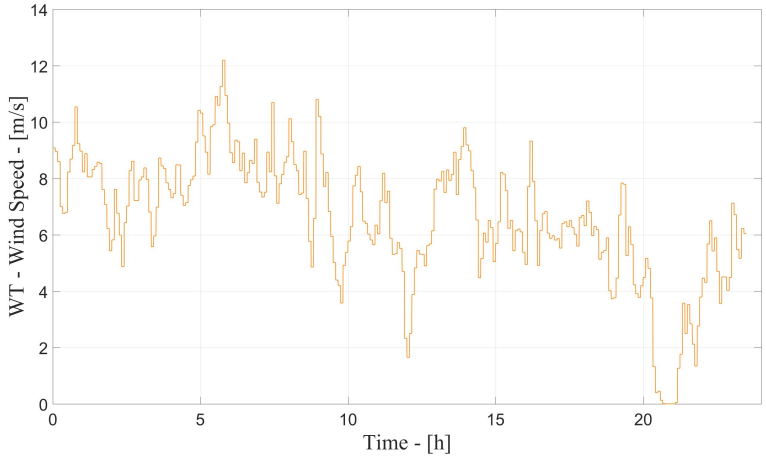

Figure 5.8: Input of wind turbine system. Wind speed in m/s.

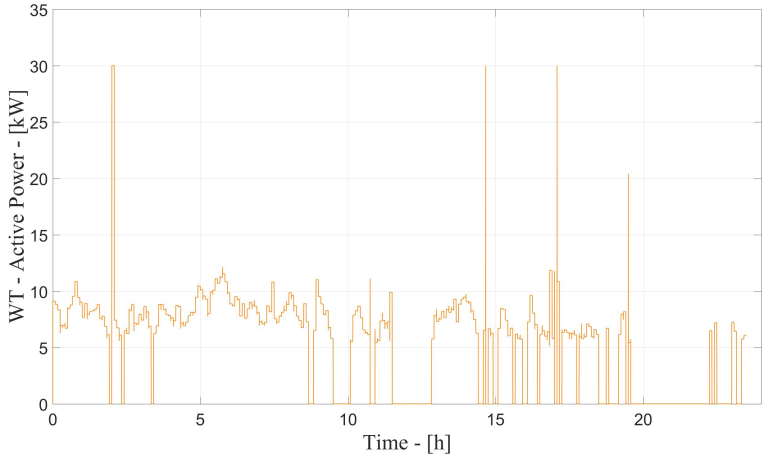

Figure 5.9: Output of wind turbine system. Active power in kW.

5.3.4 Alkaline electrolyzer

The performance of the electrolyzer is managed by the *CCS*. Figure 5.10 shows the electrolyzer power input, whereas the response of the system under the validation load profile is presented as follows: Figure 5.11 shown (a) the stack voltage, (b) the stack current and (c) the operational temperature, whereas Figure 5.12 presents (a) the flow rate and (b) the hydrogen production.

In Figure 5.10 (a), during the first 8 h the electrolyzer works at its minimum power (10% of its rated capacity, i.e. 0.8 kW) and charges the hydrogen storage tank, then, after 8 h there is an operation at the rated power (8 kW) due to the increase of *RES* over the midday hours. After 14 h the hydrogen storage tank reaches its maximum level (95 % out of 7 m^3 of its capacity) and the electrolyzer is turned off, see figure 5.12 (b). The energy requested by the electrolyzer during the day is 2.12 kWh.

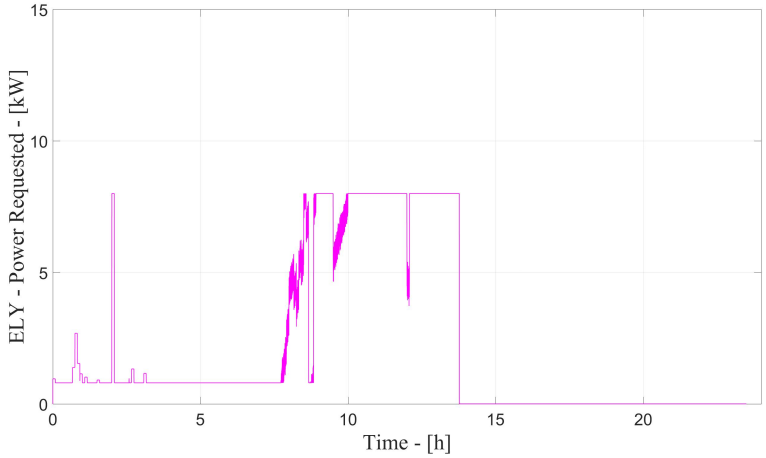

Figure 5.10: Input of alkaline electrolyzer. Active power requested in kW.

The response of the electrolyzer is reported in Figure 5.11 and 5.12. When it is operating at its the rated power, the electrical values are: nominal voltage 45 V, nominal current 130 A and H_2 production 21 lpm. We can note a constant operating temperature at 30°C.

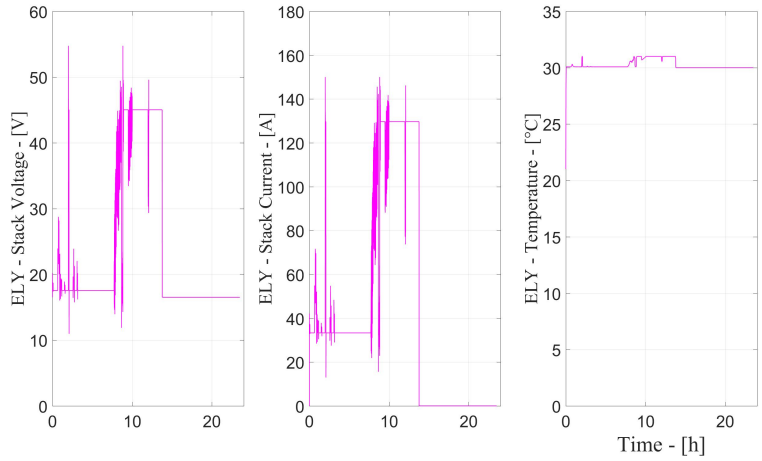

Figure 5.11: Outputs of alkaline electrolyzer. (a) Stack voltage in V, (b) Stack current in A and (c) Operational temperature in °C.

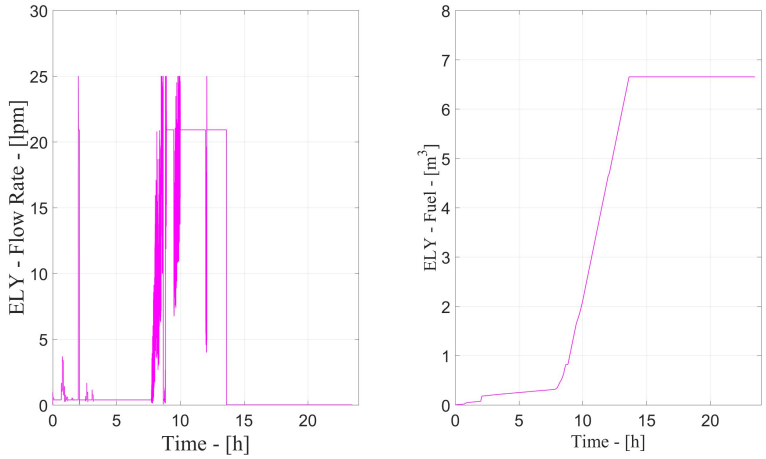

Figure 5.12: Outputs of alkaline electrolyzer. (a) Flow rate in lpm and (b) hydrogen production m^3.

5.3.5 PEM fuel cell

The validation of the *PEM* fuel cell is reported in Figure 5.13, which shows the inputs of the system, i.e., (a) the flow rate and (b) the hydrogen consumption, whereas the outputs of the system are presented in Figure 5.14. Figure 5.14 (a) shows the power produced, Figure 5.14 (b) the stack voltage and Figure 5.14 (c) the stack current.

In figure 5.13 (a) we can note the *PEM* fuel cell works during 1.5 h out of 24 h, where it consumes the H_2 available into the hydrogen storage tank until it reaches its minimum capacity (10 % of 7 m^3), see Figure 5.13 (b). During this short period of 90 min the *PEM* fuel deliveries 6.66 kWh corresponding to 0.41 kWh during a period of 24 h as shown in Figure 5.14 (a). The voltage of the *PEM* fuel cell is almost constant and about 80 V whereas the current follows the power requested to reach the demand, see Figure (b) 5.14 and (c) 5.14, respectively.

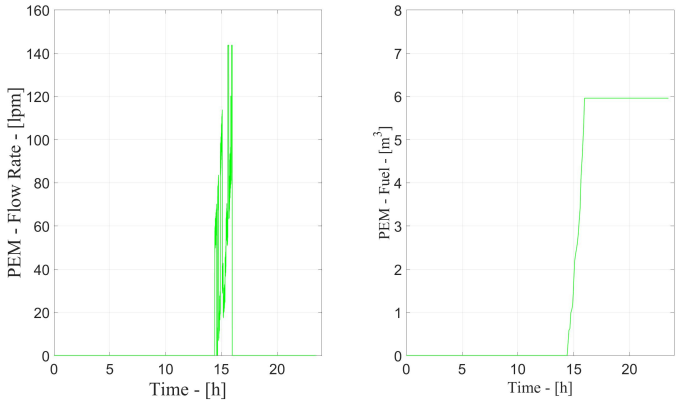

Figure 5.13: Input of *PEM* fuel cell. (a) Flow rate in lpm and (c) hydrogen consumption in m^3.

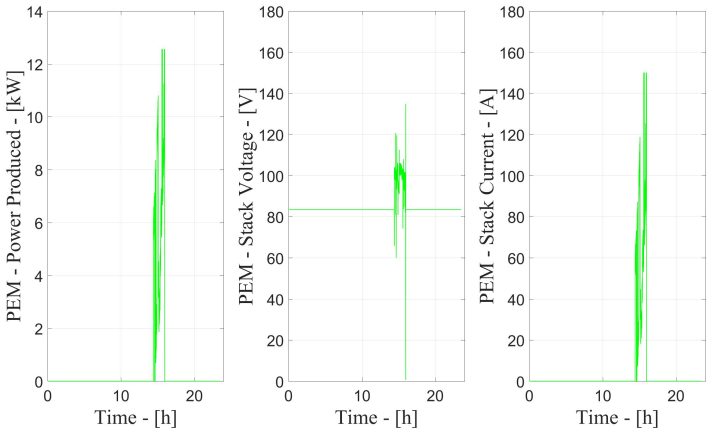

Figure 5.14: Outputs of *PEM* fuel cell. (a) Stack voltage in V, (b) Stack current in A and (c) Power produced in kW.

5.3.6 Hydrogen storage tank

The outputs of the hydrogen tank are presented in Figure 5.15: (a) the H_2 level in % and (b) the tank level in m^3. If the tank is charging, the tank level increases until it reaches the 95 % of its capacity (6.5 m^3), whereas when the tank is discharging, it decreases until the 10 % of its minimum capacity (0.7 m^3). The capacity of the tank has been chosen 7 m^3 in the validation case, in order to charge until its maximum level (6.5 m^3) in 5.5 hours with a constant inlet flow of hydrogen of 20 lpm.

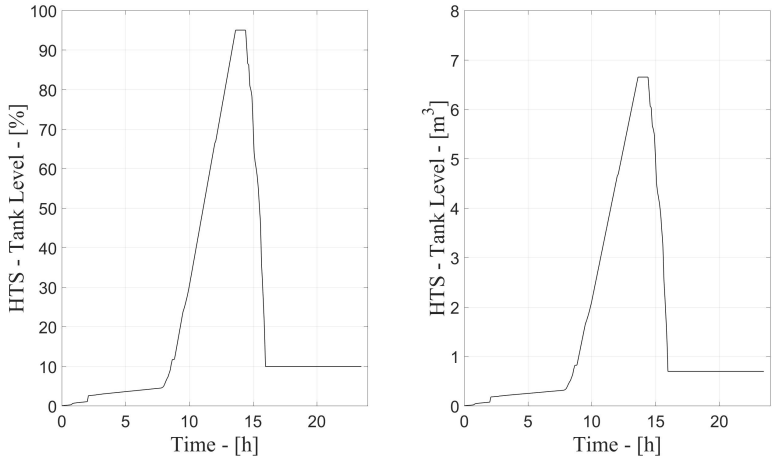

Figure 5.15: Outputs of hydrogen storage tank. (a) H_2 level in % and (b) H_2 level in m^3.

5.3.7 Grid

The power balance at the *PCC* is presented in Figure 5.16. As mentioned before in Section 5.2 when the $P_{GRID} < 0$ the $H\mu G$ is injecting power into the grid, whereas, when $P_{GRID} > 0$ a grid power contribution is necessary to meet the demand curve. In the figure is noted during the first 5 hours a small contribution of the grid due to the presence of the *RES*. Hours later (midday) when the power produced by the photovoltaic system reaches its peak, it is reported an exchange of power with the grid. Finally, in the last part of the day (night hours) when there is not solar irradiation, the quantity of power requested from the grid is almost the power demand.

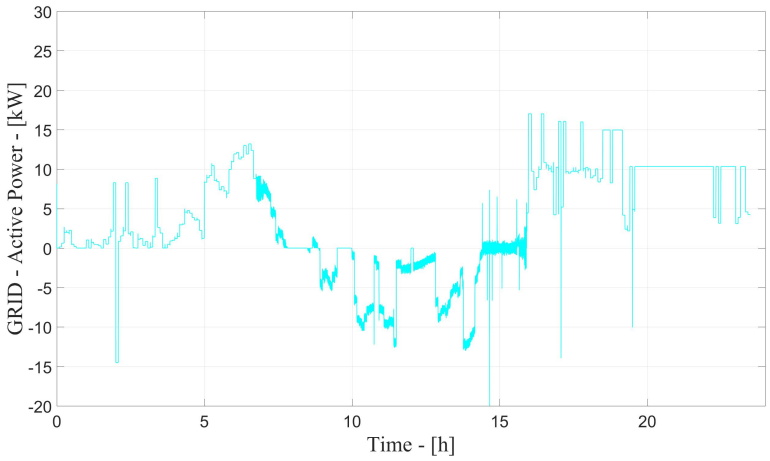

Figure 5.16: Grid. Active power exchange with the grid in kW.

5.3.8 Performance of HuG

The performance of the $H\mu G$ under a validation load profile is summarized in Figure 5.17. The blue line shows the demand profile, the light blue line the power generated from the *RES* coupling with a hydrogen system and the purple line presents the power generated without the hydrogen system. When the hydrogen system is installed, we can note a constant reduction of the power exchanged with the grid over the operating period of the electrolyzer (from 0 h until 16 h). During the fist 6 hours the value of the energy generated from *RES* is few and the electrolyzer works at is minimum capacity. Then, during the earlier hours, the response of the system with and without hydrogen system are almost the same.

At midday (between 9 h and 14 h), when the power generated from the photovoltaic system plays an important role, the electrolyzer tends to work at is rated power. Then, in this period the level of the hydrogen storage tank reaches its maximum capacity. After, between 14 h and 17 h, with the presence of the hydrogen system, there is an equilibrium of the power flow ($P_{GRID} = 0$) due to the response of the *PEM* fuel cell: over this period, the demand is reached by the sum of the power generated from the *RES* and the *PEM* fuel cell. Finally, in the nights hours (after 18 h), the hydrogen storage decreases until its minimum capacity and the *PEM* fuel cell is turned off. Being during the night a poor production of power from the photovoltaic system, the electrolyzer cannot be turned on, and as a consequence the demand curve is meet mainly by the contribution of the grid.

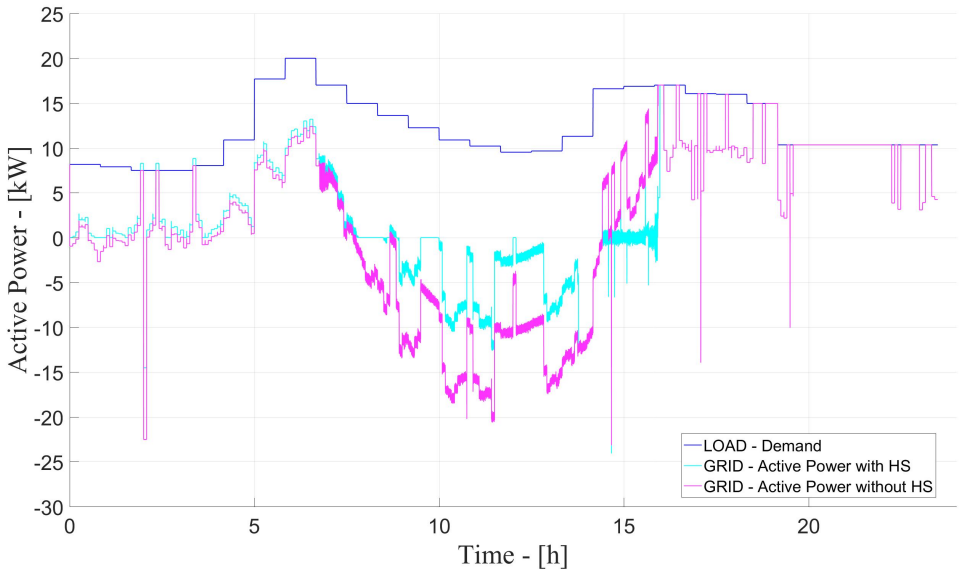

Figure 5.17: Integrated System Simulation. Confronting performance of the system with-/without hydrogen system. Active power exchange with the grid in kW.

5.4 Analyzing Validation Profile

Figure 5.18 shows the power flow of the $H\mu G$ at the *PCC*. As a result, the power demanded can be completely fulfilled during the whole simulation. The operation of the alkaline electrolyzer and the *PEM* fuel is not simultaneously: in other words, when the electrolyzer is powered, the *PEM* fuel cell cannot produce active power and vice versa. Furthermore, with a surplus of power produced by WT and PV systems, it is allowed the injection of power into the grid only when the surplus is higher than the rated power of the electrolyzer. Then, the performance of the global model is as expected and we can see the hybrid configuration adapts to the grid requirements during most of the simulation.

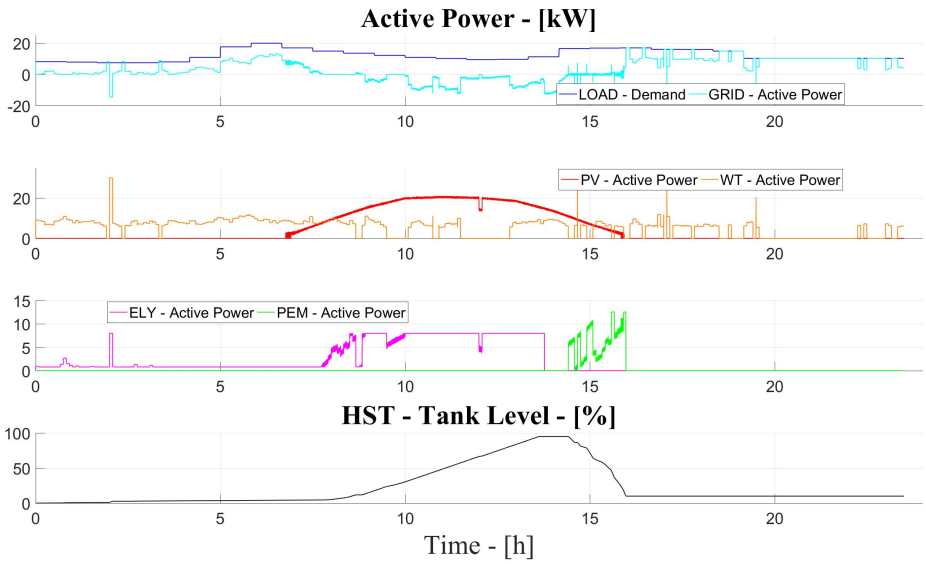

Figure 5.18: Global model of $H\mu G$. Response to validation load profile. Power flow at PCC with active power in kW.

To evaluate the performance of the model it is necessary to study different scenarios. Figure 5.19 presents the match between the load and the power generated by primary sources, i,e. WT and PV system. Then, it is possible to classify the six different scenarios mentioned before in Section 5.3.

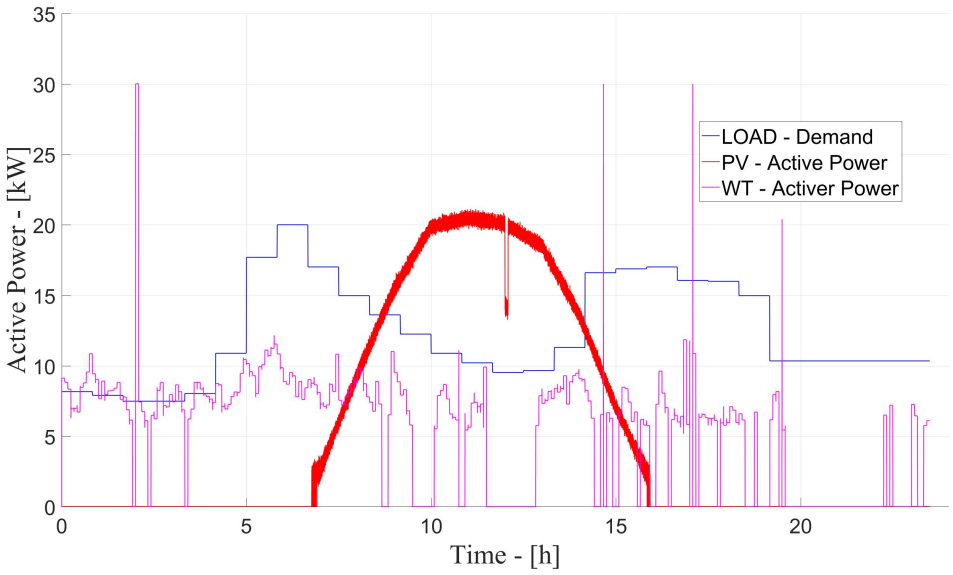

Figure 5.19: Global model of $H\mu G$. Validation load profile. Classifying different scenarios.

As we can see, between 3.43 h and 8.67 h there is a extremely wind favorable condition which correspond to **Scenario 1**. Above midday hours, between 10.23 h and 13.08 h it is possible to find the same extremely favorable condition to the *PV* system which corresponds to **Scenario 2**. **Scenario 3** could be found between 12.88 h and 14.40 h when there are high values of solar irradiation and wind speed over the same period. Regarding the least favorable conditions, **Scenario 4** can be established from 11.47 h until 12.81 h, while over the early and later hours when there is not sun **Scenario 5** may be easily found (before 6.92 h and after 15.92 h, respectively). Finally, **Scenario 6** corresponding to a wind and solar irradiation and being the most critical, can be found over the period compressed in the time 19.66 h and 22.23 h .

Figures 5.20 and 5.21 show the **first** and **second scenario** respectively. In these condition are expected: on one hand, an operation of the alkaline electrolyzer, and on the other hand, the *PEM* fuel cell should be not operated. However, the value required to meet the power demand is essential to perform the operation of the hydrogen absorption/consumption system. Moreover, if there is an extremely favorable conditions of wind or solar irradiation and if the power demand requested is higher than power generated by primary sources, the *PEM* fuel system may contribute to meet the demand.

5.4.1 Scenario 1

In the most favorable wind condition there is a constant operation of the electrolyzer, as is shown in Figure 5.20. Between 3 h and 7.5 h the electrolyzer is operated at its minimum power (0.8 kW) even when the power demand is higher or equal than the power generated from the WT system above a mean of 500 s. Further later, at 6.5 h, occurs an increase of the power generated from the PV system, then, there is a surplus of power respect to the demand and as consequence the electrolyzer stars to produce hydrogen with a higher flow rate. About 8 h the hydrogen storage tank is charged quickly from 0 % to 20 % in 1.8 h. However, between 8.7 h and 8.9 h, there is a great decline of the wind turbine contribution being its power generated 0: in this moment, the electrolyzer is turned off until there are good enough wind conditions at 8.9 h. We can also note, in this scenario the PEM fuel cell is not operated.

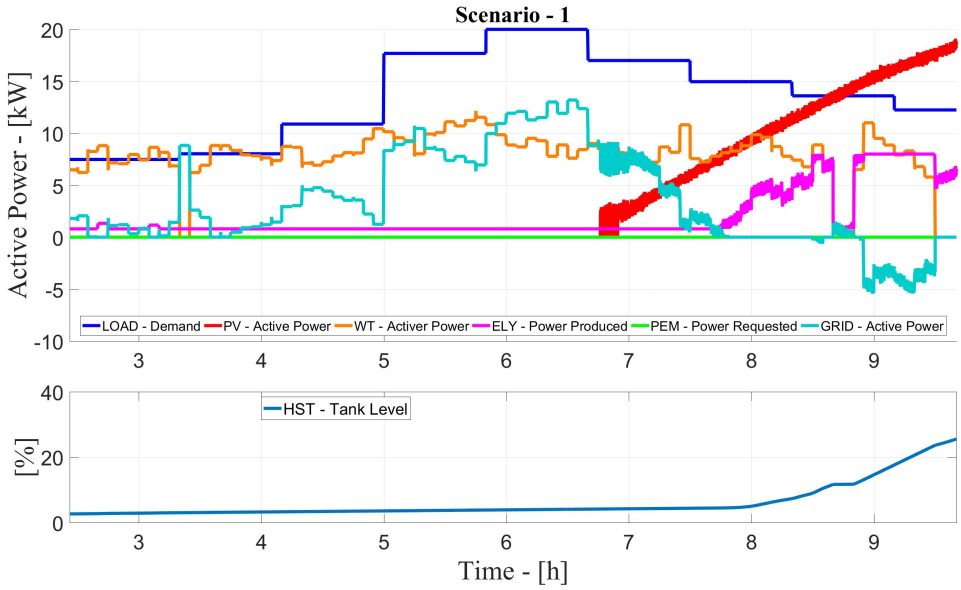

Figure 5.20: Global model of $H\mu G$. Validation load profile. Scenario 1. Extremely favorable wind conditions.

5.4.2 Scenario 2

Figure 5.21 corresponds to the favorable solar irradiation conditions. As expected, there is a prominent operation of electrolyzer. Considering this period with a power production from PV system higher than the power demanded, we can see a constant operation of the electrolyzer, even at its rated power (8 kW) over much of the period. The hydrogen tank

is charged at its maximum capacity (95 %). In this case a power exchange into the grid is noted when the surplus is higher than the rated power of the electrolyzer. Being the midday hours the most favorable period for the operation of the photovoltaic system, over all this period, there is a constant exchange of power with the grid. The fuel cell, instead, is not operated.

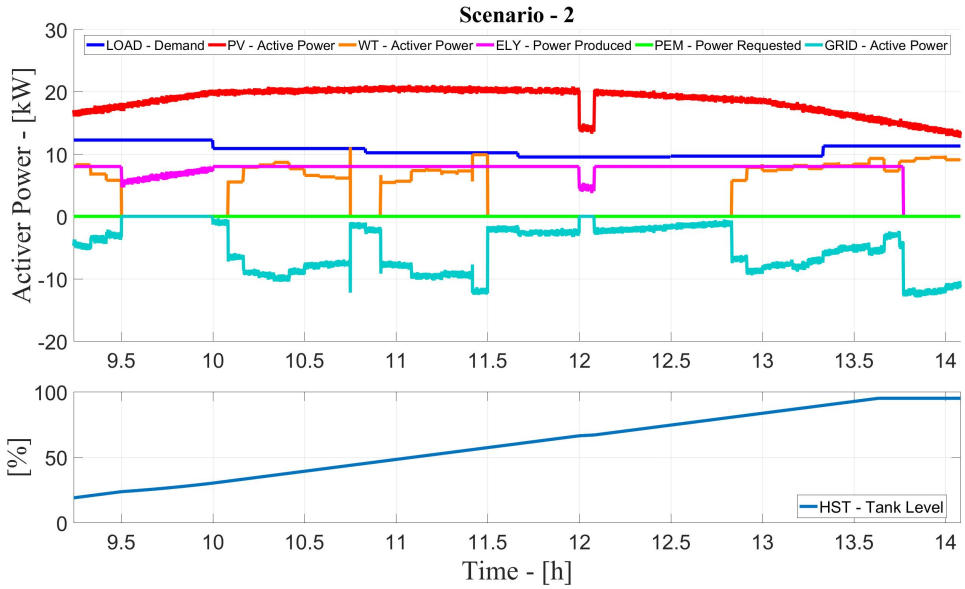

Figure 5.21: Global model of $H\mu G$. Validation load profile. Scenario 2. Extremely favorable solar conditions.

5.4.3 Scenario 3

For both wind and solar irradiation favorable conditions, the electrolyzer should be constantly operated while the *PEM* fuel cell should be disabled. Between 12.5 h and 14.5 h there is a high density of power generated from renewable sources and the hydrogen tank is charged until its maximum level (95 %). Over much of the period, the electrolyzer works at its rated power and power is injected into the grid as well.

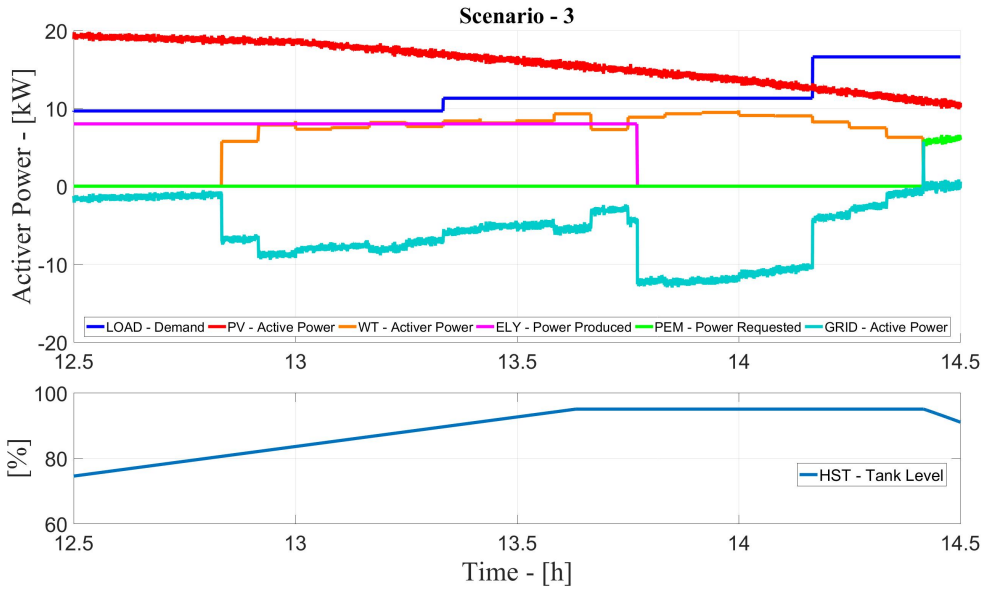

Figure 5.22: Global model of $H\mu G$. Validation load profile. Scenario 3. Both wind and solar irradiation favorable conditions.

5.4.4 Scenarios 4 and 5

Figure 5.23 to Figure 5.25 show poor conditions of wind and solar irradiation, respectively. In these conditions is expected an intermittent operation of the fuel cell, while the electrolyzer should not be considered. Moreover, it is not probable the power injection into the grid. Hydrogen tank tends to discharge constantly.

In Figure 5.23 is noted some periods with poor wind speed and a decreasing trend of the solar irradiation, determining the operation of the *PEM* fuel cell: (*a*) 14.4 - 14.6 h (*b*) 14.7 - 14.8 h (*c*) 14.9 - 15 h and (*d*) 15.4 - 15.7 h. In contrast, in Figures 5.24 and 5.25 are noted poor values of solar irradiation, referred to early hours (before 7 a.m) and later hours (after 5 p.m) respectively when the sun is not available: in these cases, there is not a predominant production of hydrogen.

In both scenarios, the performance of the system follows the same way: (*i*) no operation of electrolyzer (*ii*) power supply to load from fuel cell according to state of charge of tank and (*iii*) no power exchange with the grid. It is evidenced that even though distributed generators are not protagonist, demand is met mainly with the modest response from wind and solar systems and the capability of fuel cell.

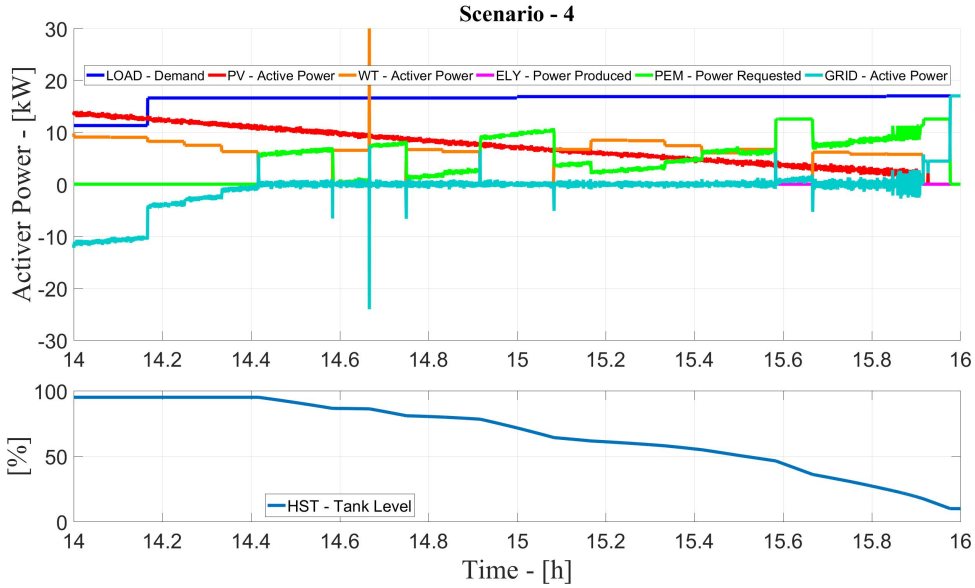

Figure 5.23: Global model of $H\mu G$. Validation load profile. Scenario 4. Scarce wind condition.

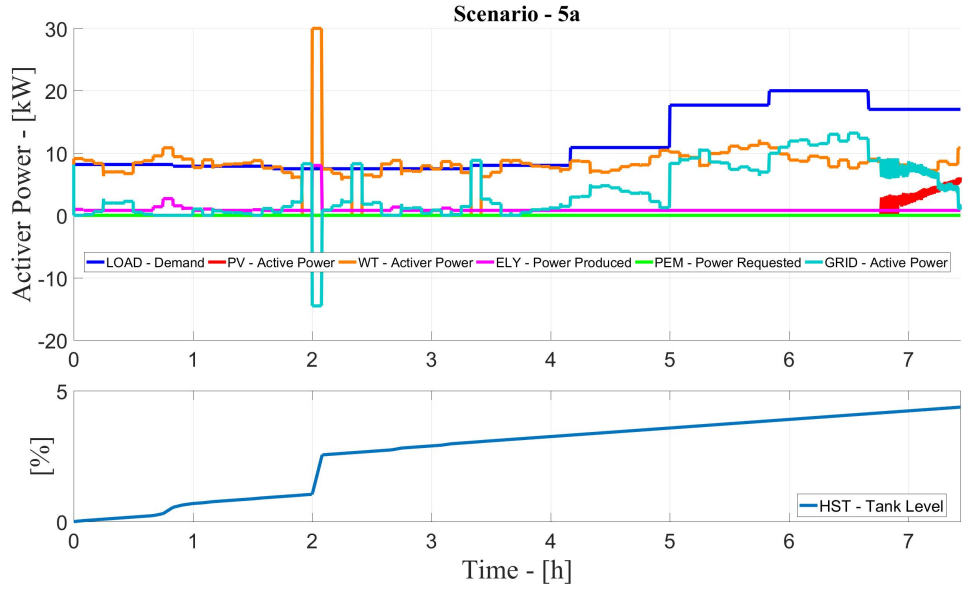

Figure 5.24: Global model of $H\mu G$. Validation load profile. Scenario 5a. Scarce solar irradiation condition at early hours.

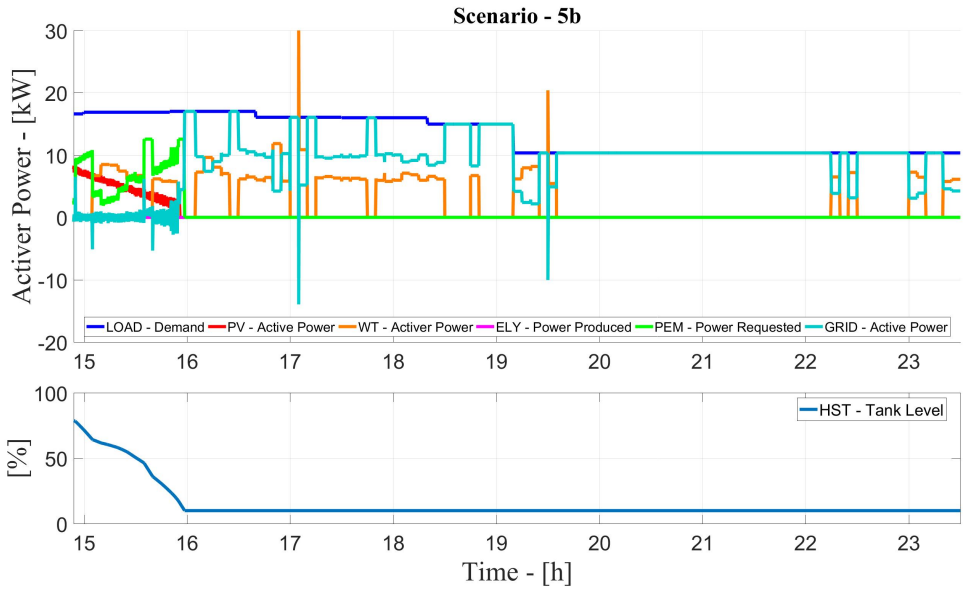

Figure 5.25: Global model of $H\mu G$. Validation load profile. Scenario 5b. Scarce solar irradiation condition at later hours.

5.4.5 Scenario 6

For the most critical situation which is show Figure 5.26, there are poor wind speed and solar irradiation conditions. In this case the electrolyzer has not to be operated, while the fuel cell is available to supply the load when there is a backup of hydrogen in the tank. The scenario does not expect a power injection into the grid. The power generated from wind turbine and photovoltaic systems in null. Electrolyzer is turned off and the *PEM* fuel cell does not produce power. However, in the worst case, the *PEM* and fuel cell may produce active power according to the presence of hydrogen in the tank.

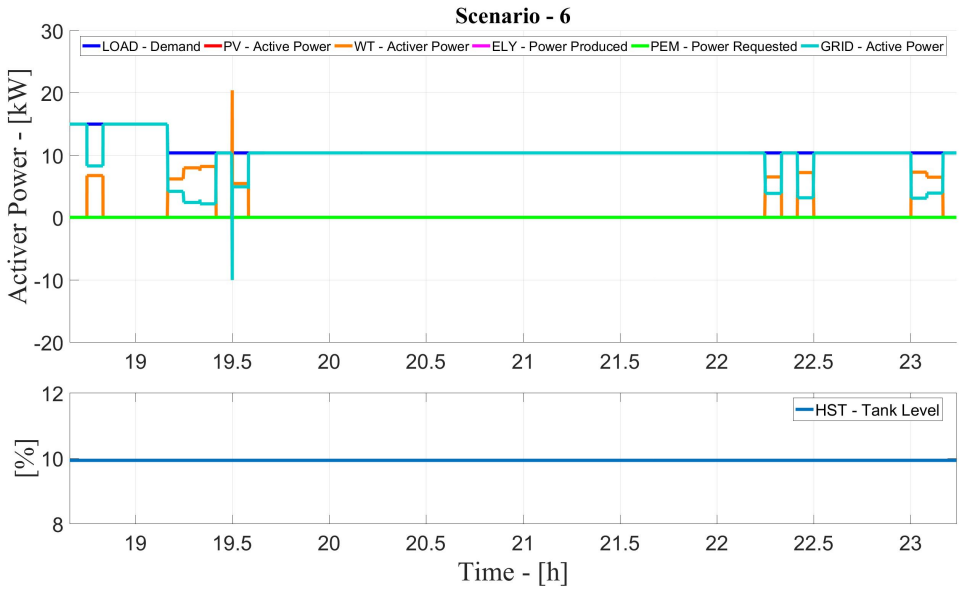

Figure 5.26: Global model of $H\mu G$. Validation load profile. Scenario 6. Both wind and solar irradiation scarce conditions.

5.5 Case of studies

In the Section 5.6 and Section 5.7 are presented the two case studies based on load profiles measured in two days in an electrical substation of the *Politecnico di Torino*. The profiles correspond to: (i) variable load and (ii) static load. The power produced by the primary sources, i.e, PV and WT systems is the same as the ones previously presented in Chapter 3 for validation purposes. Then, in the follow are presented the responses of the electrolyzer, hydrogen tank and the PEM fuel cell for each case. Moreover, it is presented the power power flow of the μG (model without integration of hydrogen system) and $H\mu G$ (model with integration of hydrogen system) at the PCC. The results obtained for both cases are reported in the figures shown below. The outline of the section is in both cases the following one:

1. Load profile
2. Alkaline electrolyzer.
3. PEM fuel cell.
4. Hydrogen storage tank.
5. Grid.
6. Performance of the $H\mu G$.

5.6 Case of Study 1 - Variable Load

5.6.1 Load

The variable load profile is presented in Figure 5.27. The profile varies quickly from 0 to 22 kW over all the period. The energy demand during the day is 11.41 kWh.

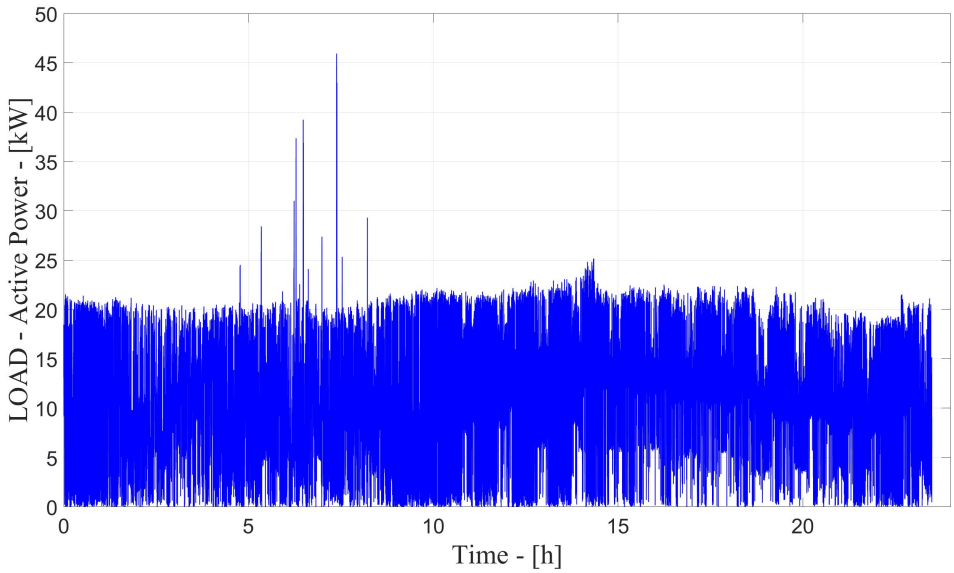

Figure 5.27: Case of study 1: Input of the system (variable load profile). Active power in kW.

5.6.2 Alkaline electrolyzer

Figure 5.28 shows the power requested by the electrolyzer under a variable load profile. The response of the system is reported as follows: Figure 5.29 shows (a) the stack voltage, (b) the stack current and (c) the operational temperature, whereas Figure 5.30 presents (a) the flow rate and (b) the hydrogen production.

The power supply of the electrolyzer depends of the power balance at the *PCC*. If the power produced from the *RES* is higher than the demand curve, the electrolyzer could be supplied. In Figure 5.28 (a), during the first 15 h the electrolyzer is powered with a variable supply due to the nature of the demand curve. Until 15 h, it works in all its operation range (between 0.8kW and 8kW), then, the hydrogen storage tank reaches its maximum level (95 % out of 12 m^3 of its capacity) and the electrolyzer trends to be turned off, or in

the best case, to operate at its minimum power, see figure 5.30 (b). The energy requested by the electrolyzer during the day is 2.77 kWh.

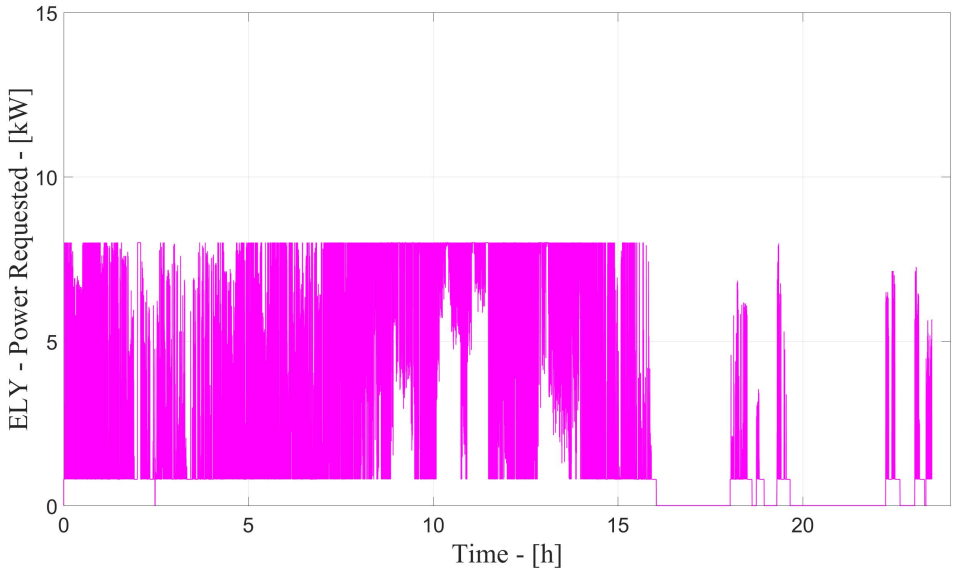

Figure 5.28: Case of study 1: Input of the alkaline electrolyzer system with a variable load profile. Active power requested in kW.

The operating voltage and current of the electrolyzer are reported in Figure 5.29 (a) and Figure 5.30 (b), respectively. During the first 16 h the power supply of the electrolyzer is variable; then, it operates between 10-55 V and 10.5-150 A in order to meet the power demand. After 16 h, the role of the electrolyzer is not predominant and it has an intermittent operation and it is turned off twice. Then, it works at open voltage (16.5 V) with $I_{ELY}^{(st)} = 0$. In Figure 5.29 (c) we can note a constant operating temperature of 30°C.

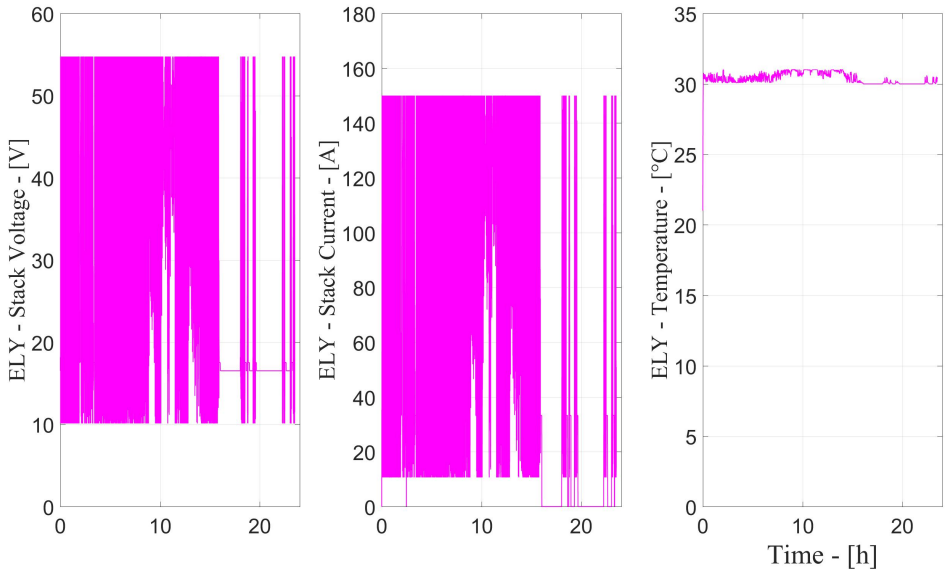

Figure 5.29: Case of study 1: Response of the alkaline electrolyzer system under a variable load profile. (a) stack voltage in V, (b) stack current in A and (c) operational temperature in °C.

The H_2 production follows the power requested and it depends of the availability of power from the *RES* and the demand curve. In other words, the flow rate varies according to the variance of the power requested, producing maximum 24.7 lpm as shown in Figure 5.30 (a). In the early hours (before 8 h) there is only a contribution of the wind turbine system, whereas the contribution of the photovoltaic system is null: then, hydrogen tank level increases with a low slope. After 9 hours (until 15 h), when the photovoltaic power appears, the slope of H_2 production increases drastically until the capacity of the hydrogen tank is full. Finally, in the night hours, the electrolyzer production is almost null due to the poor availability of solar energy or the hydrogen tank full field, see Figure 5.30 (b).

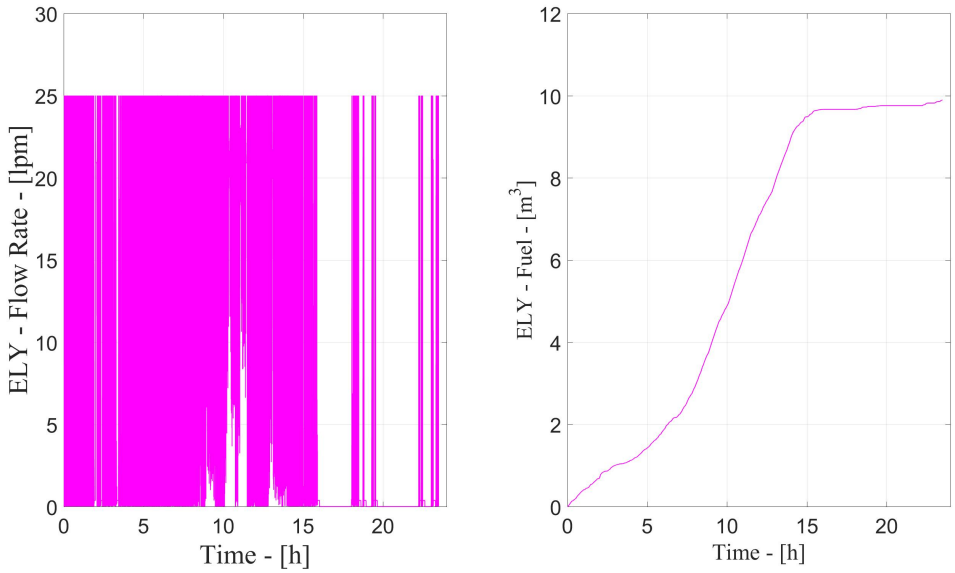

Figure 5.30: Case of study 1: Response of the alkaline electrolyzer system under a variable load profile. (a) flow rate in lpm and (b) hydrogen production in m^3.

5.6.3 PEM fuel cell

The response of the *PEM* fuel cell with a static load profile is reported as follows: Figure 5.31 shown the inputs of the system, i.e., (a) flow rate and (b) hydrogen consumption, whereas the outputs of the system are presented in Figure 5.32 and summarized as: (a) power produced, (b) stack voltage and (c) stack current.

In Figure 5.31 (a) we can observe the *PEM* fuel cell working about 4 hours (between 16 h out of 20 h), until it reaches the minimum capacity of the hydrogen tank (10 % out of 12 m^3), see Figure 5.31 (b). The energy consumed by the *PEM* fuel cell during the day is 0.57 kWh, as shown in Figure 5.32 (a). The voltage of the *PEM* fuel cell is almost constant and about 80 V except for the period when it is operating, (voltage level oscillating from 40-130V), see Figure 5.32 (b), whereas the current, when the PEM fuel cell produces energy, it changes between 0-145A, as shown in 5.32 (c).

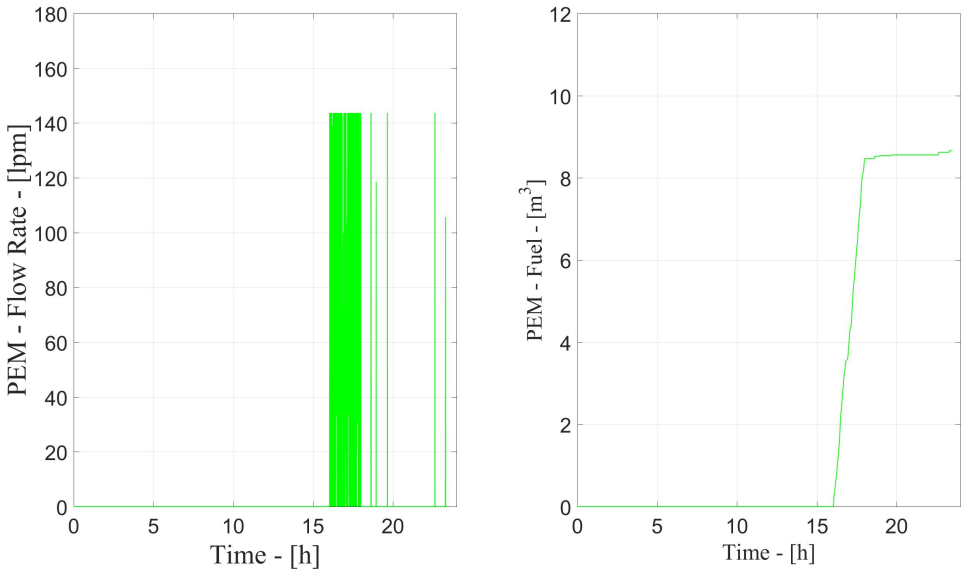

Figure 5.31: Case of study 1: Input of the *PEM* fuel cell system with a variable load profile. (a) flow rate in lpm and (b) hydrogen production in m^3.

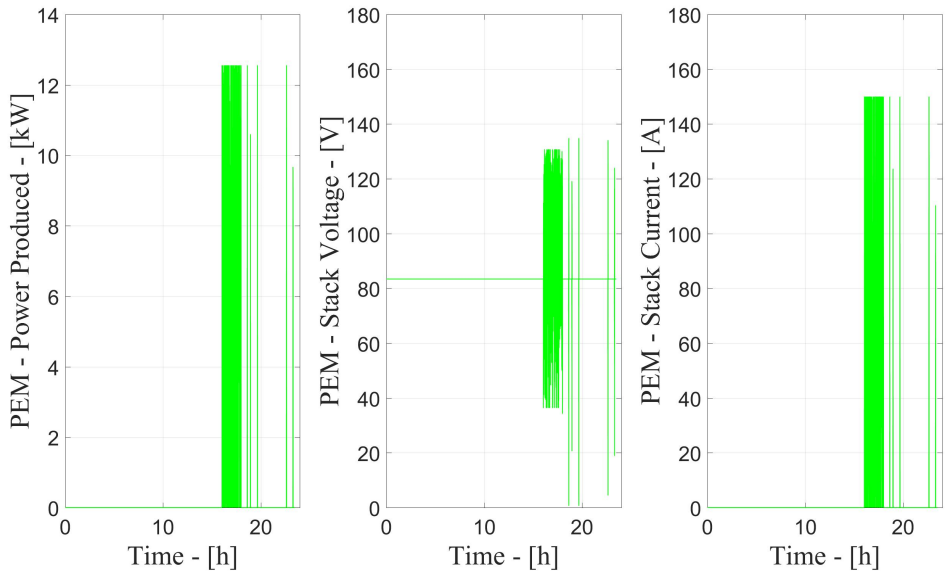

Figure 5.32: Case of study 1: Response of the *PEM* fuel cell system under a variable load profile. (a) stack voltage in V, (b) stack current in A and (c) power produced in kW.

5.6.4 Hydrogen tank

In Figure 5.33 (a) and (b) are reported the hydrogen tank level in % and m^3, respectively. It is noted in the first part of the day the tank level increases until it reaches the 80 % of its capacity (9.9 m^3) due to the operation of the electrolyzer, whereas in the last part (at 15 h), it decreases drastically until reaching the minimum level (10 % out of 12 m^3) due to the contribution of the *PEM* fuel cell to meet the demand (when the power from *RES* is not available in higher quantities).

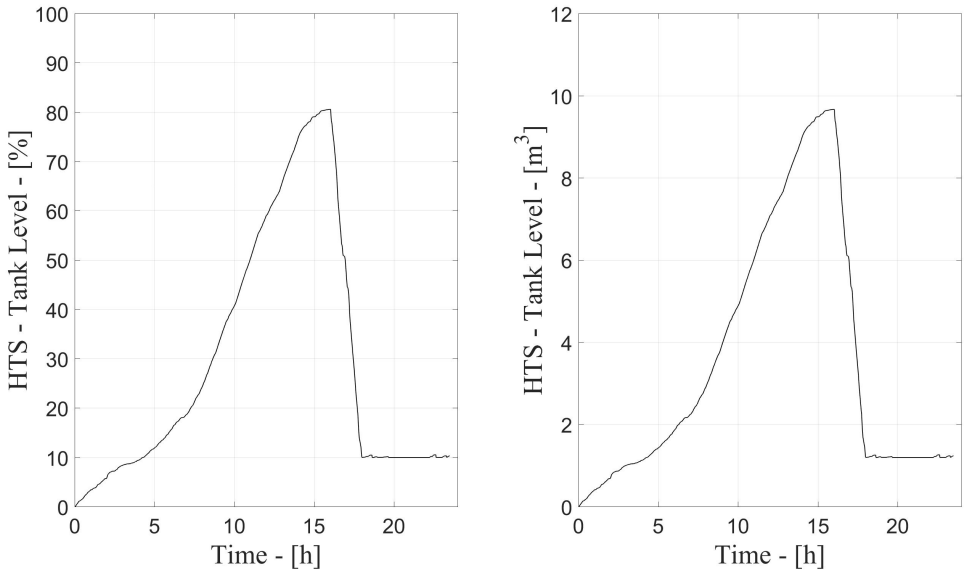

Figure 5.33: Case of study 1: Response of the *HST* system under a variable load profile. (a) tank level in % and (b) tank level in m^3.

5.6.5 Grid

For the case with a variable load profile, the power balance at the *PCC* is presented in Figure 5.34. In the figure is noted during the first 7 hours a few contribution of the grid due to the presence of the *RES*. About midday hours there is an exchange of power with the grid due to the presence of the peak of the photovoltaic system. We can see between 16 h and 18 h a short period exchanging power with the grid, it is due to the contribution of the *PEM* fuel cell to meet a power demand with a high dynamic (variable load). Finally, after 18 h, there is not solar irradiation and only the grid has to meet the power demand.

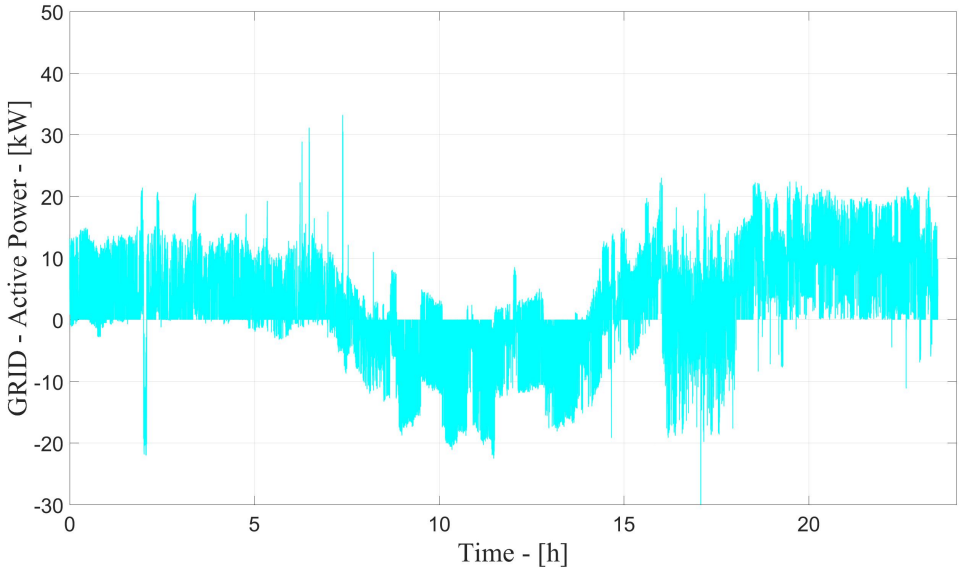

Figure 5.34: Case of study 1: Power exchange of the $H\mu G$ with the grid under a variable load profile. Power flow at PCC in kW.

In Figure 5.35 the response of all components composing the $H\mu G$ is summarized: (a) demand curve and grid contribution, (b) power generated from RES (wind turbine and photovoltaic systems), (c) hydrogen system (alkaline electrolyzer and PEM fuel cell) and (d) level of hydrogen storage tank. The energy demands per day are reported as follow: (i) load: 11.41 kWh, (ii) grid contribution 2.85 kWh, (iii) wind turbine system: 5.38 kWh, (iv) photovoltaic system: 5.37 kWh, (v) alkaline electrolyzer: 2.77 kWh and (vi) PEM fuel cell 0.57 kWh.

In the first case (variable load profile), it is consumed the 25.76 % (2.77 kWh) of the total energy obtained from the RES (10.75 kWh) to operate the electrolyzer, in order to produce H_2 which could be a fuel to the PEM fuel cell in a second moment. Moreover, 0.57 kW are returned from the PEM fuel cell to meet the power demand. Then, delivering 25.76 % of the power generated from the RES to supply the hydrogen system, 5.30 % can be recovered when there are not good enough environmental conditions to produce energy with the RES.

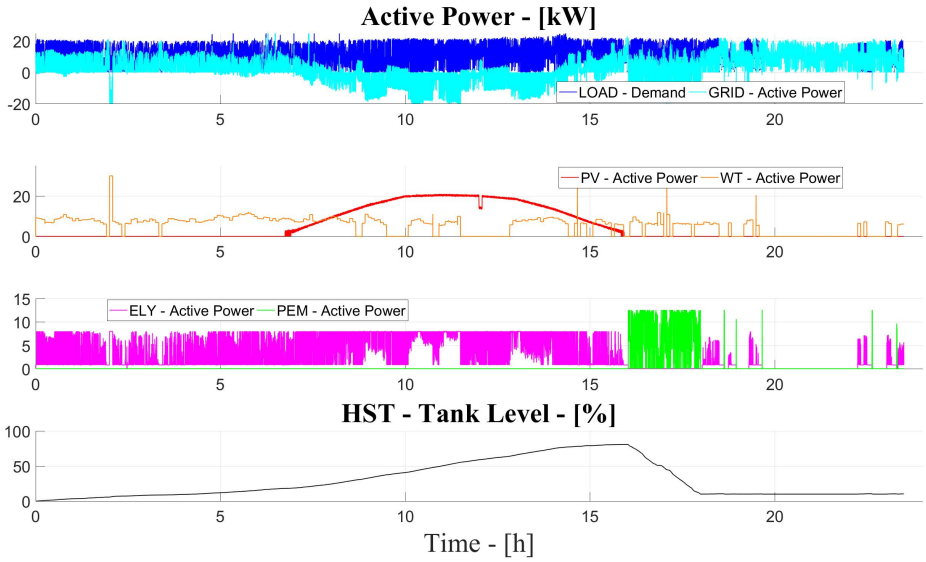

Figure 5.35: Case of study 1: Response of the $H\mu G$ under a variable load profile. Power flow at PCC in kW.

5.6.6 Performance of HuG

The performance of the $H\mu G$ under a variable load profile is reported in Figure 5.36. In Figure 5.36 (a), the first 6 h, we cannot not observe a higher difference between the response of μG (without hydrogen system) and the $H\mu G$ (with hydrogen system) and both profiles are almost the same. In Figure 5.36 (b), between 6 h and 8 h, it is noted a reduction of the power exchanged with the grid when the hydrogen system is installed, due to the power consumed in the operation of the electrolyzer (in this period the peak of the photovoiltaic system occurs and the electrolyzer can be powered). The operation of the PEM fuell cell occurs between 16 h and 18 h: in this period, it is noted a smaller contribution from the grid to meet the power demand, as a consequence of the presence of the PEM fuel cell. Finally, in Figure 5.36 (c), after 19 h, the contribution of the RES is few and the hydrogen tank is discharged, then, the behavior of the μG and the $H\mu G$ is the same.

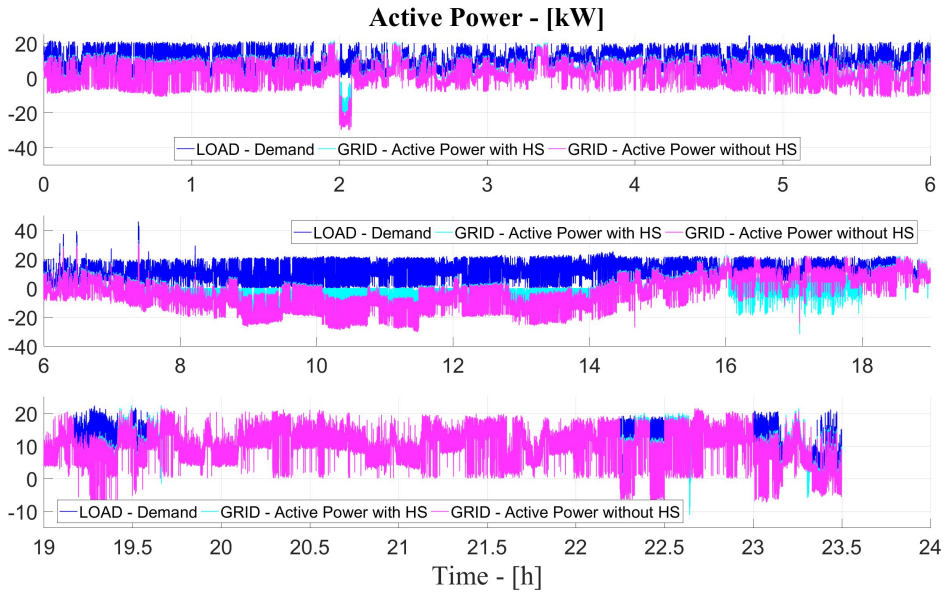

Figure 5.36: Case of study 2. Confronting performance of the system with/without hydrogen system under a variable load profile. Active power exchange with the grid in kW.

5.7 Case of Study 2 - Static Load

5.7.1 Load

The second case is the static load profile, as shown in Figure 5.37. The profile is characterized by a constant demand curve about 10.5 kW with some transitory peaks of 20 kW. The energy demand during the day is 10.22 kWh.

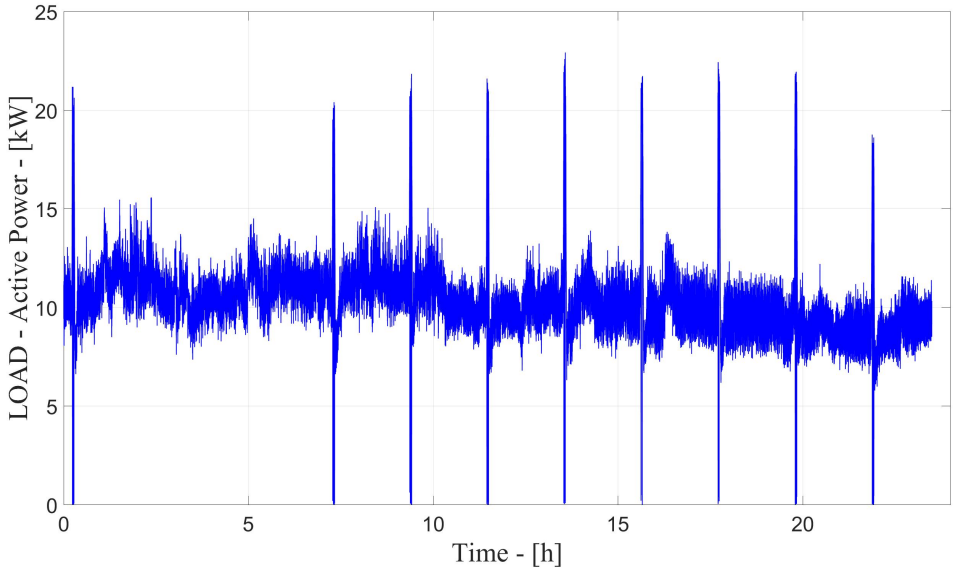

Figure 5.37: Case of study 2: Input of the system (static load profile). Active power in kW.

5.7.2 Alkaline electrolyzer

With a static load profile we can note easily three behaviors, see Figure 5.38 (*a*): (*i*) during the first part of the day (until 8 hours) the electrolyzer operates constantly at its minimum power (0.8 kW), (*ii*) after that (when photovoltaic power comes), between 8 h until 15 h, it works at its maximum power (8 kW) and (*iii*) in the last part of the day (after 15 h) the electrolyzer is turned off. In this case (static load) the electrolyzer works as expected and there are not abnormal behaviors for discussing. The energy requested by the electrolyzer during the day is 2.59 kWh.

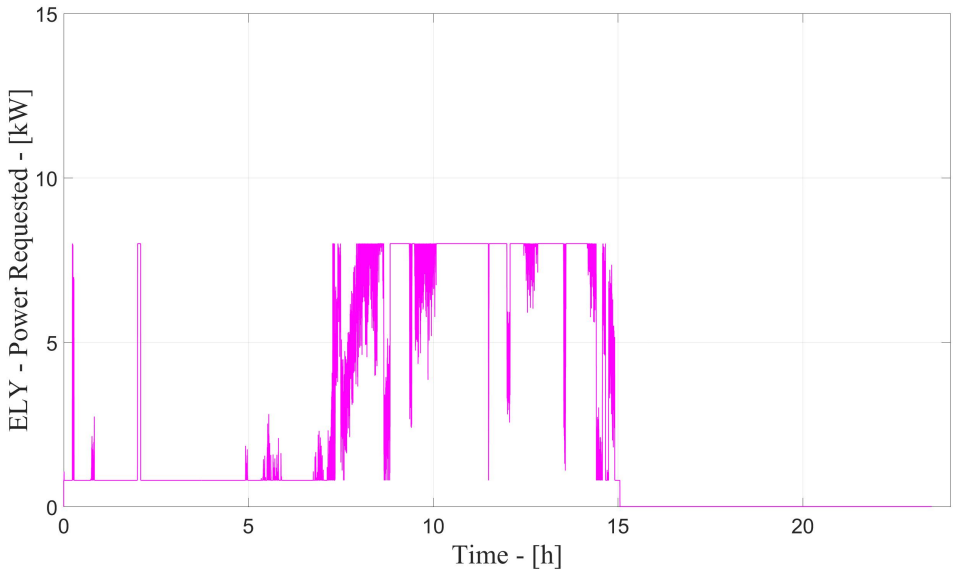

Figure 5.38: Case of study 2: Input of the alkaline electrolyzer system with a static load profile. Active power requested in kW.

The response of the electrolyzer is reported in Figure 5.39 and 5.40. We can note: (i) when the electrolyzer works at its minimum power (until 8 h) we have operating voltage 17.53 V, operating current 33.31 A and H_2 production 0.37 lpm. When the electrolyzer works at its maximum power (between 7 h and 75 h) we have operating voltage 45 V, operating current 130 A and H_2 production 20.9 lpm. In both cases the operating temperature is 30°C.

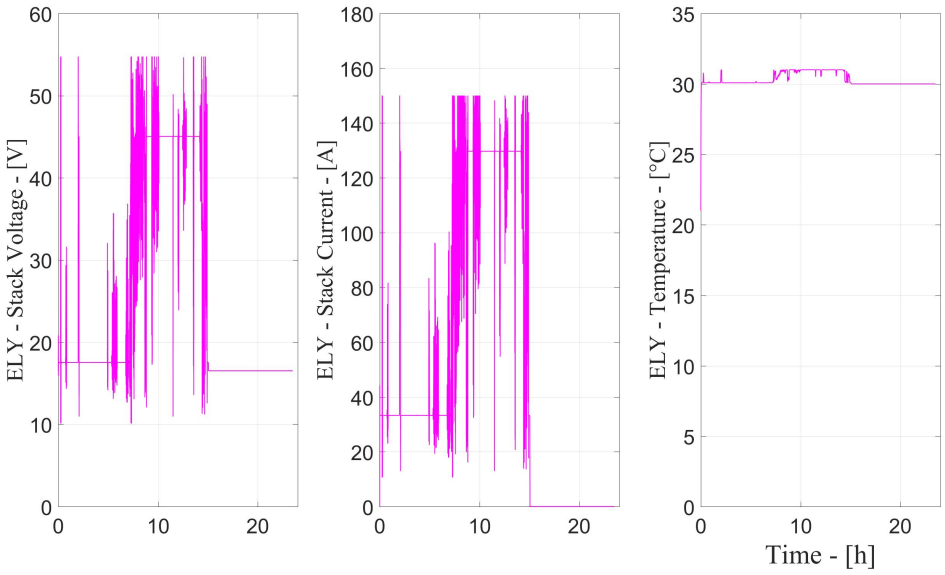

Figure 5.39: Case of study 2: Response of the alkaline electrolyzer system under a static load profile. (a) stack voltage in V, (b) stack current in A and (c) operational temperature in °C.

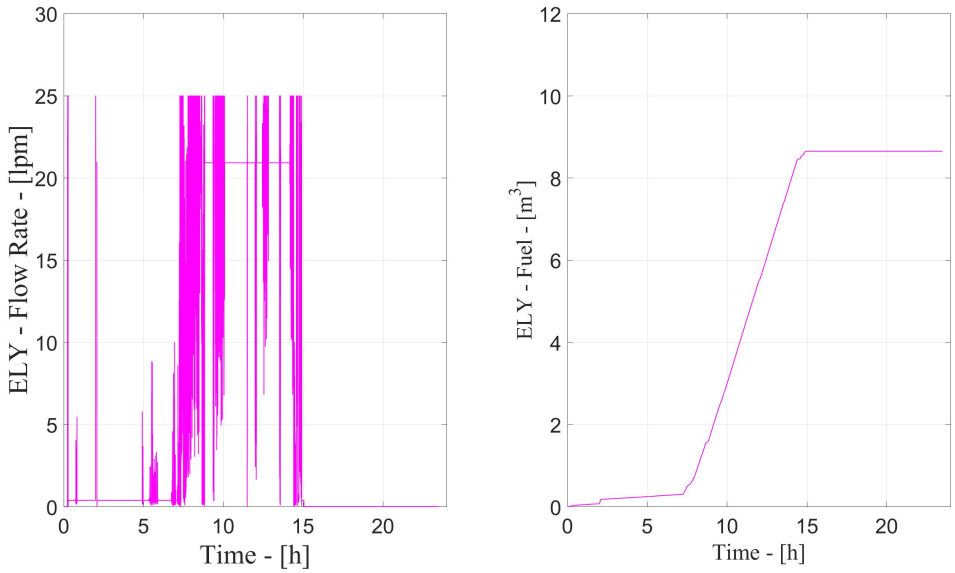

Figure 5.40: Case of study 2: Response of the alkaline electrolyzer system under a static load profile. (a) flow rate in lpm and (b) hydrogen production in m^3.

5.7.3 PEM fuel cell

The response of the *PEM* fuel cell with a static load profile is reported as follows: Figure 5.41 shown the inputs of the system: (a) flow rate and (b) hydrogen consumption, whereas the outputs of the system are presented in Figure 5.42 and summarized as: (a) power produced, (b) stack voltage and (c) stack current.

In Figure 5.41 (a) and (b) we can observe the *PEM* fuel cell working about 3 hours (between 15 h out of 18 h), until it reaches the minimum capacity of the hydrogen tank (10 % out of 12 m^3). The energy consumed by the *PEM* fuel cell during the day is 0.52 kWh, as shown in Figure 5.42 (a). The voltage of the *PEM* fuel cell is almost constant and about 80 V except for the period when it is operating, (voltage level oscillating from 40-120V), see Figure 5.42 (b), and for the current, when the PEM fuel cell produces energy, it changes between 0-145A, as shown in 5.42 (c).

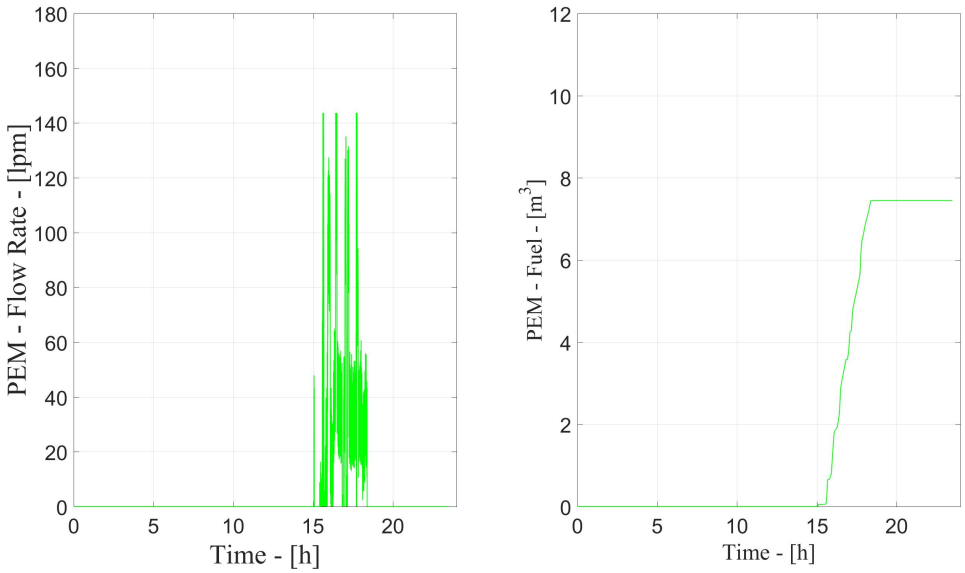

Figure 5.41: Case of study 2: Input of the *PEM* fuel cell system with a static load profile. (a) flow rate in lpm and (b) hydrogen production in m^3.

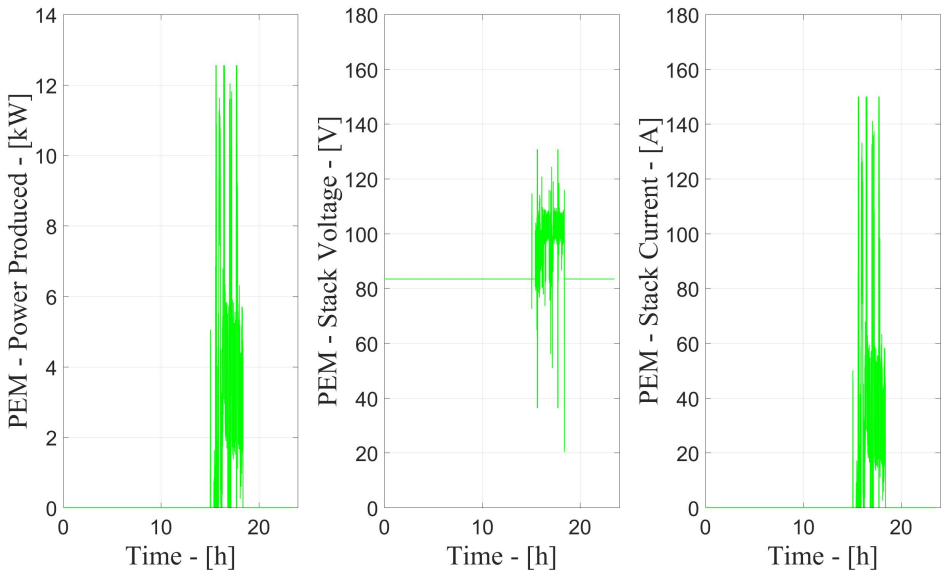

Figure 5.42: Case of study 2: Response of the *PEM* fuel cell system under a static load profile. (a) stack voltage in V, (b) stack current in A and (c) power produced in kW.

5.7.4 Hydrogen tank

In Figure 5.43 (a) and (b) are reported the hydrogen tank level in % and m^3, respectively. It is noted in the first part of the day the tank level increases until it reaches the 80 % of its capacity (9.9 m^3) due to the operation of the electrolyzer, whereas in the last part (at 15 h), it decreases drastically until reaching the minimum level (10 % out of 12 m^3) due to the contribution of the *PEM* fuel cell to meet the demand, when power from *RES* is not available in higher quantities.

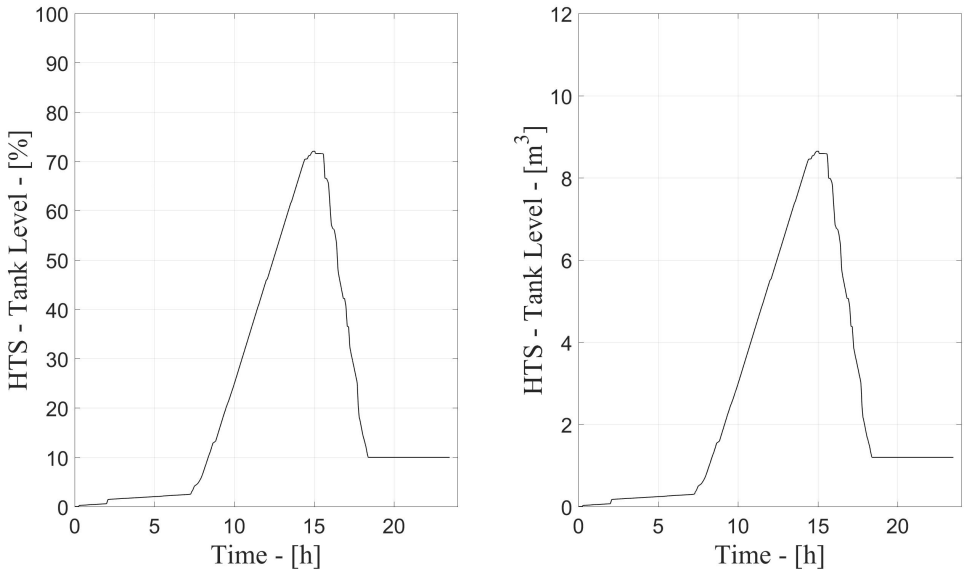

Figure 5.43: Case of study 2: Response of the *HST* system under a static load profile. (a) tank level in % and (b) tank level in m^3.

5.7.5 Grid

With a static load profile, the power flow balance at the *PCC* is shown in Figure 5.44. We can see for the first 7 hours a constant contribution of the grid, whereas about midday hours it is presented a reverse power flow towards the grid. In this case (static load profile), when the *PEM* fuel cell works to meet the demand (between 16 h and 18 h) a reverse power flow is smaller than in the previous case (variable load profile). Finally, after 19 h, the contribution of the grid to meet the power demand is predominant.

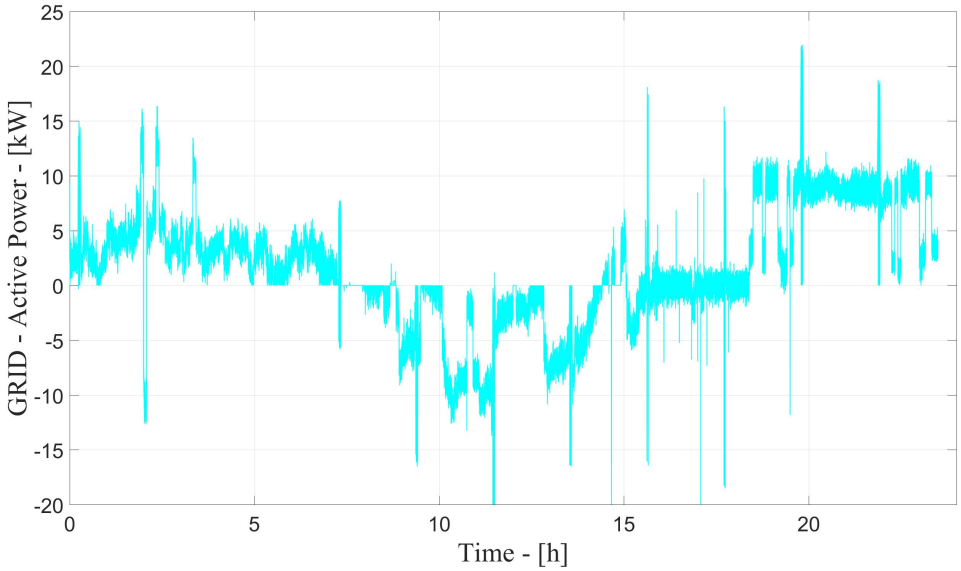

Figure 5.44: Case of study 2: Power exchange of the $H\mu G$ with the grid under a static load profile. Power flow at *PCC* in kW.

In Figure 5.45 is summarized the response of all components composing the $H\mu G$: (a) demand curve and grid contribution, (b) power generated from *RES* (wind turbine and photovoltaic systems), (c) hydrogen system (alkaline electrolyzer and *PEM* fuel cell) and (d) level of hydrogen storage tank. The energy demands per day are reported as follow: (i) load: 10.22 kWh, (ii) grid contribution 1.53 kWh, (iii) wind turbine system: 5.38 kWh, (iv) photovoltaic system: 5.37 kWh, (v) alkaline electrolyzer: 2.59 kWh and (vi) *PEM* fuel cell 0.52 kWh.

In the second case (static load profile), it is consumed the 24.09 % (2.59 kWh) of the total energy obtained from the *RES* (10.75 kWh) to operate the electrolyzer. Moreover, 0.52 kW are returned from the *PEM* fuel cell to meet the power demand, then, delivering 24.09 % of the power generated from the*RES* to supply the hydrogen system, 4.83 % can be recovered.

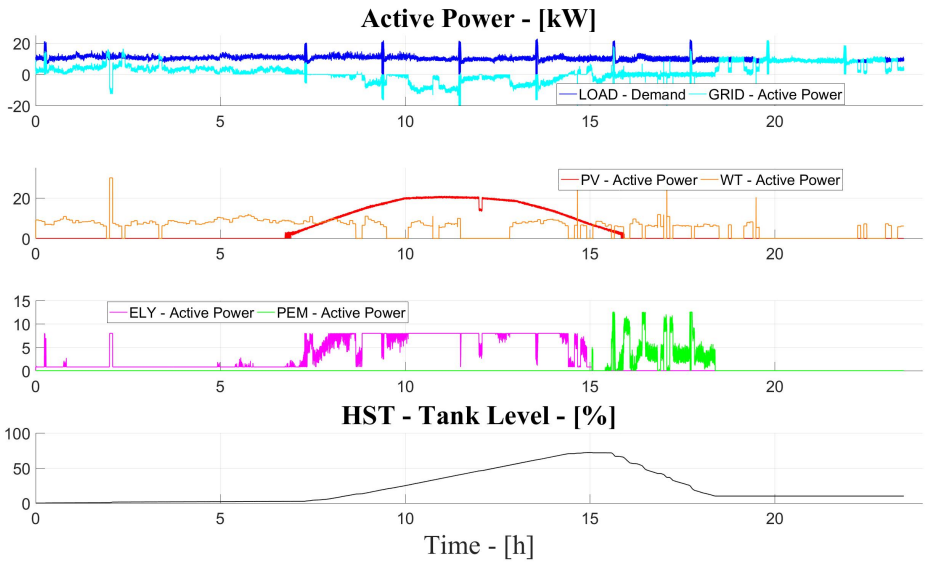

Figure 5.45: Case of study 2: Response of the $H\mu G$ under a static load profile. Power flow at PCC in kW.

5.7.6 Performance of HuG

The performance of the $H\mu G$ under a static load profile is reported in Figure 5.46. In the first 6 h, it is observed a small difference in the response of the μG (without hydrogen system) with respect to the $H\mu G$ (with hydrogen system), due to the operation of the electrolyzer at its minimum power (0.8 kW) when power from the RES is not quite high. In the midday hours (between 6 h and 16 h), the system feels the presence of the hydrogen system and it is note a high discrepancy between both responses. The operation of the PEM fuel cell occurs between 16 h and 18 h. In this period, we can see a almost null contribution from the grid to meet power demand. Finally, after 19 h, the hydrogen tank is empty and the RES energy produced is not higher a lot to supply the electrolyzer, then, the behavior of the μG and the $H\mu G$ is almost the same.

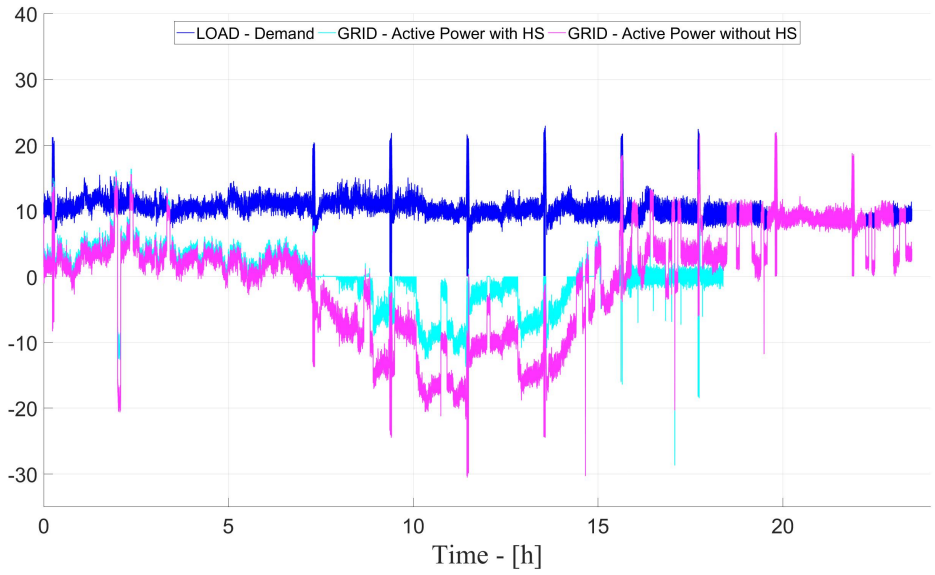

Figure 5.46: Case of study 2. Confronting performance of the system with/without hydrogen system under a static load profile. Active power exchange with the grid in kW.

5.8 HuG Performance

The performance of the $H\mu G$ is assessed through a sensitivity analysis presented in Table 5.1 for the variable load profile and Table 5.2 for the static load profile. As follow are reported the cases selected for studying the model response:

1. One photovoltaic system, one wind turbine system and one electrolyzer.
2. Two photovoltaic systems, two wind turbine systems and one electrolyzer.
3. Two photovoltaic systems, two wind turbine systems and two electrolyzers.

In these three cases, the capability of the hydrogen tank is increased gradually, studying the response of the *PEM* fuel cell and the power flow balance at the *PCC*. The wind speed, solar irradiation and operating temperature of the photovoltaic system are common for both cases.

In Table 5.1 is presented the sensitivity analysis for the response of the system under a variable load profile. In the first case (one photovoltaic system, one wind turbine system and one electrolyzer), the total energy average produced by the *RES* is 10.75 kWh which is less than the energy average demanded (11.41 kWh). When the system operates without the hydrogen system, the grid contribution of the system is 0.65 kWh, then, adding the

hydrogen system and and having constant the energy produced from the *RES*, if the capability of the hydrogen tank increases (from 12 m^3 to 54 m^3), the power returned from the *PEM* fuel cell to the grid decreases (from 0.56 kWh to 0.34 kWh) and the grid contribution to meet the demand increases (from 0.65 kWh to 3.09 kWh).

In the second case, duplicating the contribution from the *RES* (21.5 kWh) we have a condition $Power_{RES} > Power_{Demand}$. Operating the system with one electrolyzer, when the capability of the hydrogen tank increases (from 7 m^3 to 54 m^3), the power returned from the *PEM* fuel cell to the grid increases (from 0.45 kWh to 0.90 kWh) and the grid contribution increases (from -10.10 kWh to -6.54 kWh).

Table 5.1: Case 1. Sensitivity analysis of hydrogen system performance under a variable load profile.

PV Systems	*WT* Systems	*ELY* Systems	*HST* m^2	*PV* - kWh	*WT* - kWh	*ELY* - kWh	*PEM* - kWh	Grid Contribution - kWh
1	1	-	-	5.37	5.38	-	-	0.65
1	1	1	12	5.37	5.38	2.77	0.56	2.85
1	1	1	15	5.37	5.38	2.77	0.54	2.87
1	1	1	27	5.37	5.38	2.72	0.48	2.90
1	1	1	54	5.37	5.38	2.78	0.34	3.09
2	2	-	-	10.74	10.76	-	-	-10.10
2	2	1	7	10.74	10.76	1.99	0.45	-8.55
2	2	1	9	10.74	10.76	2.47	0.52	-8.14
2	2	1	12	10.74	10.76	3.21	0.74	-7.63
2	2	1	15	10.74	10.76	3.94	0.84	-6.99
2	2	1	27	10.74	10.76	4.45	0.90	-6.54
2	2	1	54	10.74	10.76	4.45	0.90	-6.54
2	2	2	7	10.74	10.76	2.10	0.49	-8.48
2	2	2	9	10.74	10.76	2.63	0.54	-8.01
2	2	2	12	10.74	10.76	3.33	0.75	-7.52
2	2	2	15	10.74	10.76	4.05	0.85	-6.89
2	2	2	27	10.74	10.76	7.12	1.50	-4.48
2	2	2	54	10.74	10.76	8.90	1.78	-2.98

(*i*) Wind speed average: 6.5837 m/s. (*ii*) Solar irradiation average: 249.108 W/m^2. (*iii*) Temperature average: 30.381 °C. (*iv*) demand energy average: 11.41 kWh.

Finally, in the last case, duplicating again the contribution from the *RES* but adding

a second electrolyzer, increasing the capability of the hydrogen tank (from 7 m^3 to 54 m^3) the power returned from the *PEM* fuel cell to the grid increases (from 0.49 kWh to 1.78 kWh) and grid contribution decreases (from -10.10 kWh to -2.98 kWh).

In Table 5.2 is presented the same analysis performed by considering the static load. In the first case (one photovoltaic system, one wind turbine system and one electrolyzer), the total energy average produced by the *RES* is 10.75 kWh which is almost equal to the energy average demanded (10.22 kWh). When the system operates without the hydrogen system, the grid contribution of the system is -0.53 kWh, then, adding the hydrogen system and and having constant the energy produced from the *RES*, if the capability of the hydrogen tank increases (from 12 m^3 to 54 m^3), the power returned from the *PEM* fuel cell decreases (from 0.52 kWh to 0.22 kWh) and the grid contribution increases (from -0.53 kWh to 1.86 kWh).

In the second case (two photovoltaic systems, two wind turbine systems and one electrolyzer), duplicating the contribution from the *RES* (21.5 kWh) and operating the system with one electrolyzer, when the capability of the hydrogen tank increases (from 7 m^3 to 54 m^3), the power returned from the *PEM* fuel cell to the grid increases (from 0.43 kWh to 0.76 kWh) and the grid contribution increases (from -11.29 kWh to -7.33 kWh).

Finally, in the last case (two photovoltaic systems, two wind turbine systems and two electrolyzers), duplicating again the contribution from the *RES* and adding a second electrolyzer, increasing the capability of the hydrogen tank (from 7 m^3 to 54 m^3) the power returned from the *PEM* fuel cell to the grid increases (from 0.46 kWh to 1.72 kWh) and grid contribution decreases (from -11.29 to -3.78 kWh).

Table 5.2: Case 2. Sensitivity analysis of hydrogen system performance under a static load profile.

PV Systems	*WT* Systems	*ELY* Systems	*HST* m^2	*PV* - kWh	*WT* - kWh	*ELY* - kWh	*PEM* - kWh	Grid Contribution - kWh
1	1	-	-	5.37	5.38	-	-	-0.53
1	1	1	12	5.37	5.38	2.59	0.52	1.53
1	1	1	15	5.37	5.38	2.59	0.50	1.55
1	1	1	27	5.37	5.38	2.59	0.45	1.60
1	1	1	54	5.37	5.38	2.62	0.22	1.86
2	2	-	-	10.74	10.76	-	-	-11.29
2	2	1	7	10.74	10.76	2.21	0.43	-9.50
2	2	1	9	10.74	10.76	2.65	0.57	-9.20
2	2	1	12	10.74	10.76	3.42	0.71	-8.57
2	2	1	15	10.74	10.76	4.19	0.89	-7.98
2	2	1	27	10.74	10.76	4.71	0.95	-7.53
2	2	1	54	10.74	10.76	4.71	0.76	-7.33
2	2	2	7	10.74	10.76	2.53	0.46	-9.21
2	2	2	9	10.74	10.76	2.95	0.57	-8.89
2	2	2	12	10.74	10.76	3.74	0.72	-8.26
2	2	2	15	10.74	10.76	4.51	0.90	-7.67
2	2	2	27	10.74	10.76	7.49	1.60	-5.40
2	2	2	54	10.74	10.76	9.23	1.72	-3.78

(*i*) Wind speed average: 6.58 m/s. (*ii*) Solar irradiation average: 249.10 W/m^2. (*iii*) Temperature average: 30.38 °C. (*iv*) demand energy average: 10.22 kWh.

The results obtained with the sensitivity analysis of both cases (variable load and static load) show the importance of the hydrogen tank capability for the contribution of the *PEM* fuel cell. The operation of the electolyzer is directly proportional to the capability of the tank and the energy produced from the *RES*, whereas the *PEM* fuel cell depends on the dimension of the hydrogen tank. With a small tank, it is not possible to have a high value of power injected to the grid, independently of the *RES* production energy levels. Finally, confronting the operation of a hydrogen system (electrolyzer, *PEM* fuel cell and hydrogen tank) connected with two different loads (variable and static load), when the capacity of the hydrogen tank is constant, it is observed a high operation for both the electrolyzer and the *PEM* fuel cell when the nature of the load is variable.

Chapter 6

Conclusions

In this thesis is presented a methodology to simulate the behavior of a Wind-Solar-Hydrogen Energy System. The system can produce hydrogen from the generation surpluses in a wind and solar plant. The hydrogen generated can be used later on as an energy carrier for electricity generation in fuel cells. Mathematical models to simulate the dynamic of each component of the system have been developed: *Photolvaic system*, *wind turbine generator*, *alkaline electrolyzer*, *PEM fuel cell* and *hydrogen tank*. The models encompass both dynamics and low computational requirements. The validation of electrolyzer and *PEM* fuel cell models are presented. The outputs confirmed that both models successfully depict the validation data. Results in validation process indicated an average error of less than 2 % and 6 % in dynamic behavior for hydrogen production by electolyzer and power produced by *PEM* fuel cell, respectively. Furthermore, in this work is presented a supervisory control strategy to the Wind-Solar-Hydrogen system.

The dynamic behavior of the Solar-Wind-Hydrogen system model has been by performing the simulations in different wind and solar irradiation conditions, using two cases of study: *i*: *Variable load profile* and *ii*: *Static load profile*. Therefore, it is confirmed that the developed model is a reliable tool to analyze the performance of the Wind-Solar-Hydrogen system. The simulation results have shown a satisfactory operation between the wind turbine, the photovoltaic system and the hydrogen system. As previously described, the integration of all models performed similar under variable and static power grid demand, achieving an adequate electrical response. Furthermore, a sensitivity analysis of the performance of the hydrogen system has been reported. This sensitivity analysis highlighted how the decoupling between the energy and power is positive to exploit the potential of the hydrogen system. In this way, the importance of the capability of the storage tank has been demonstrated for hydrogen systems integrated with *RES*.

In summary, the model developed in this thesis has proven to be a reliable tool for the

performance evaluation and optimization of Wind-Solar-Hydrogen plants. This demonstration project can prepare the way for a future hydrogen marketplace and it will help researches to run scenario analysis, verify theoretical findings and optimize system operations. It is therefore expected that this work will help improving cost competitiveness of renewable energy and reduce market barriers for new energy and technology solutions in general and hydrogen technology in particular. We trust that it is possible to supply remote areas with wind and solar power using hydrogen as storage medium, even if there are several things to improve in order to make the system competitive with respect to alternative systems (like wind-diesel).

Bibliography

[1] Tao Zhou, Bruno Francois *Modeling and control design of hydrogen production process for an active hydrogen/wind hybrid power system.* Ecole Centrale de Lille, Cite Scientifique, Villeneuve d'Ascq, France, 2008.

[2] L. Valverde-Isorna, D.Ali, D.Hogg, M.Abdel-Wahab. *Modelling the performance of wind-hydrogen energy systems:Case study the Hydrogen Office in Scotland/UK.* Departamento de Ingeniería Energética, Escuela Técnica Superior de Ingeniería, Universidad de Sevilla, Seville,Spain Electrical and Computer Engineering, Texas A& M University in Qatar, Doha, Qatar Bright Green Hydrogen, The Hydrogen Office, Ajax Way, Scotland, UK School of the Built Environment, Heriot-Watt University, Edinburgh, Scotland, UK

[3] Oystein Ulleberg *Modeling of advanced alkaline electrolyzers: a system simulation approach.* Institute for Energy Technology, Kjeller, Norway, 2003.

[4] Fatima Zohra Naama, Abdallah Zegaoui, Yessad Benyessad, Fatma Zohra Kessaissia, Abdelkader Djahbar, adn Michel Aillerie. *Model and Simulation of a Wind Turbine and its Associated Permanent Magnet Synchronous Generator.* School of Sustainability, Interdisciplinary Center, Herzliya, Israel. Department of Energy, Aalborg, University, Denamark. Renewable and Sustainable Energy Reviews, Vol, 90. 2018.

[5] F. Gonzatti, F.A. Farret. *Mathematical and experimental basis to model energy storage systems composed of electrolyzer, metal hydrides and fuel cells.* Federal University of Santa Maria, Santa Maria, RS, Brazil, 2016.

[6] Adam Hirscha, Yael Parag, Josep Guerrero. *Microgrids: A review of technologies, key drivers, and outstanding issues.* School of Sustainability, Interdisciplinary Center (IDC) Herzliya, Herzliya, Israel, 2018. Department of Energy Technology, Aalborg University, Aalborg East, Denmark, 2018.

[7] Francois-Xavier Saury, Craig Tomlison. *Hybrid microgrids: The time is now.* Caterpilar. February 2016.

[8] Sheetal Chandak, Pritam Bhowmik, Manohar Mishra. *Autonomous Microgrid Operation Subsequent to an Anti-Islanding Scheme*. Electrical Engineering Department, Siksha O. Anusandhan University, Bhubaneswar, India. Electrical and Electronics Engineering Department, Siksha O. Anusandhan University, Bhubaneswar, India. Sustainable Cities and Society, 2018.

[9] Dong-Jing Lee, Li Wang, Senior Member, IEEE, *Small-Signal Stability Analysis of an Autonomous Hybrid Renewable Energy Power Generation/Energy Storage System Part I: Time-Domain Simulations*. IEEE Transactions on energy conversion, Vol, 23. No. 1, March 2008.

[10] Tomonobu Senjyu, Member, IEEE, Toshiaki Nakaji, Katsumi Uezato, and Toshihisa Funabashi, Senior Member, IEEE. *A Hybrid Power System Using Alternative Energy Facilities in Isolated Island*. IEEE Transactions on energy conversion, Vol, 20, No. 2, June 2005.

[11] Sachidananda Sen, Vishal Kumar. *Microgrid modelling: A comprehensive survey*. Department of Electrical Engineering, Indian Institute of Technology Roorkee, Uttarakhand, India, 2018.

[12] *Detailed model of a 100 kW Grid-Connected PV Array*. Matworks documentation. February 2019.

[13] D. Suchitra, R. Jegatheesan, T.J. Deepika *Optimal design of hybrid power generation system and its integration in the distribution network*. Department of Electrical and Electronics Engineering, SRM University, Kattankulathur, Kancheepuram District, Chennai, Tamil Nadu, India, 2016.

[14] Yongheng Yang, Katherine A. Kim, Ariya Sangwongwanich. *Advances in Grid-Connected Photovoltaic Power Conversion System*. Elsevier Ltd. 2019.

[15] Fahad Rasool, Michael Direberg, Nasreen Badruddin, Balbir Singh Mahinder Singh. *PV panel modeling with improved parameter extraction technique*. Department of Electrical and Electronics Engineering, University Teknologi PETRONAS, Malasya. Department of Fundamental and Applied Sciences, Universiti Teknologi PETRONAS, Malasya.

[16] Vilas S. Bugade, Dr. P. K. Katti. *Dynamic Modeling of Microgrid with Distributed Generation for Grid Integration* International Conference on Energy Systems and Applications, ICESA, 2015.

[17] I. de la Parra, M. Muñoz, M. García, J. Marcos, F. Martínez Moreno. *PV performance modeling. A review in the light of quality assurance for large PV plants*. Renewable and Sustainable Energy Reviews. Institute of Smart Cities, Department of Electrical

and Electronic Engineering, Public University of Navarre. Institute of Solar Energy, PV Systems Research Group, Polythecnic University of Madrid. Renewable and Sustainable Energy Reviews, Vol, 78. 2017.

[18] Hongxing Yang, Lin Lu, Wei Zhou *A novel optimization sizing model for hybrid solar-wind power generation system.* Renewable Energy Research Group (RERG), Department of Building Services Engineering, The Hong Kong Polytechnic University, Hung Hom, Kowloon, Hong Kong, 2006.

[19] A. Goetzberger, G. Bopp, W. GrieBhaber, W. Stahl *The PV/Hydrogen/Oxygen-System of the Self- Sufficient Solar House Freiburg.* Fraunhofer-Institut fir Solare Energiesysteme Oltmannsstr, Freibur, Germany

[20] W. Hug, J. Divisek, J. Mergel, W. Seeger, H. Steeb *Highly efficient advanced alkaline electrolyzer for solar operation.* German Aerospace Research Establishment, Institute for Technical Thermodynamics, Pfaffenwaldring, Stuttgart 80, Germany, 1992. Research Centre Jiilich, Institute of Energy Process Engineering, Pfaffenwaldring, Stuttgart 80, Germany, 1992.

[21] Francesco Calise, Rafal Damian Figaj, Nicola Massarotti, Alessandro Mauro, Laura Vanoli. *Polygeneration system based on PEMFC, CPVT and electrolyzer: Dynamic simulation and energetic and economic analysis.* Dipartimento di Ingegneria Industriale, Università degli Studi di Napoli Federico II, P.le Tecchio 80, Napoli, Italy, 2016. Dipartimento di Ingegneria, Università degli Studi di Napoli "Parthenope", Centro Direzionale, IS. C4, Napoli, Italy , 2016. Università Telematica Pegaso, Piazza Trieste e Trento n. 48, 80132 Napoli, Italy, 2016.

[22] Arash Khalilnejad, Aditya Sundararajan, Alireza Abbaspour and Arif Sarwat. *Optimal Operation of Combined Photovoltaic Electrolyzer Systems.* Electrical and Computer Engineering Department, Florida International University, Miami, USA, 2016.

[23] Fco. Javier Pino, Luis Valverde, Felipe Rosa *Influence of wind turbine power curve and electrolyzer operating temperature on hydrogen production in wind-hydrogen systems.* Thermal Engineering Group, Energy Engineering Department, School of Engineering. Camino de los Descubrimientos s/n, Sevilla, Spain, 2010.

[24] Idoia San Martin, Aldredo Ursua, and Pablo Sanchis. *Modeling of PEM Fuel Cell Performance: Steady-State and Dynamic Experimental Validation* Department of Electrical and Electronic Engineering, Public University of Navarre, Campus de Arrosadia, Pamplona, Spain, Energies, Vol, 7. 2014.

[25] Tevfik Yigit, Omer Faruk Selamet. *Mathematical modeling and dynamic Simulink simulation of high-pressure PEM electrolyzer system.* Mechatronics Engineering Depart-

ment, Nidge University, Nigde, Turkey. International Journal of Hydrogen Energy, (2016).

[26] Samson Gebre Tesfahunegn. *Fuel Cell Assisted Photovoltaic Power Systems*. Thesis for the degree of Philosophiae Doctor, Norwegian University of Science and Technology, Faculty of Information Technology, Mathematics and Electrical Engineering. Trondheim, 2012.

[27] Tevfik Yigit, Omer Faruk Selamet. *Mathematical modeling and dynamic Simulink simulation of high-pressure PEM electrolyzer system*. Mechatronics Engineering Department, Nigde University, Nigde 51245, Turkeyr, 2016. Dr. T. Nejat Veziroglu Clean Energy Research Center, Nigde University, Nigde 51245, Turkey, 2016.